

An Atom Interferometer for Measuring Horizontal Accelerations

Jimmy Stammers

Department of Physics
Centre for Cold Matter

A thesis submitted to Imperial College London for partial fulfillment of the
requirements for the degree of Doctor of Philosophy

Abstract

Matter-wave interferometry has enabled high precision measurements of inertial forces such as gravity and the Coriolis force. This is facilitated by the long-term stability of the physical properties of atoms and lasers. Recent experiments have demonstrated the operation of portable, robust sensors using atom interferometry. This has potential uses in the context of inertial navigation, where conventional devices suffer from long-term drifts due to bias instability. Furthermore, determining position via dead reckoning requires minimisation of dead time between measurements. This thesis presents the development of an atom interferometer for measuring horizontal accelerations. In this configuration, gravity induces motion across the laser wavefront, which constrains the tolerable level of wavefront distortions. Effective control of the experiment allows the interferometer to be operated at a rate of 4 Hz. A cold ensemble of 10^6 atoms in the same internal state is prepared in 150 ms. The interferometer operates using a sequence of three laser pulses separated by $T = 25$ ms to achieve sensitivity to horizontal accelerations. Combining this with a classical accelerometer provides a method of correcting for vibration-induced noise, as well as determining the interferometer fringe order. After an integration time of 40 s, the sensitivity to horizontal accelerations is better than $3 \times 10^{-6} \text{ m s}^{-2}$. Effects which limit this sensitivity are discussed.

Declaration

I declare that this thesis is the result of my own work. All sources used for this work have been clearly referenced in accordance with the departmental requirements.

Jimmy Stammers

The copyright of this thesis rests with the author and is made available under a Creative Commons Attribution Non-Commercial No Derivatives licence. Researchers are free to copy, distribute or transmit the thesis on the condition that they attribute it, that they do not use it for commercial purposes and that they do not alter, transform or build upon it. For any reuse or redistribution, researchers must make clear to others the licence terms of this work.

Acknowledgements

There are many people whose support I wish to acknowledge. Firstly, I would like to thank Ed Hinds for his supervision and guidance throughout the project. His attention to detail and desire to understand the experiment from first principles have taught me a lot about how to approach scientific research. I also owe a great deal of thanks to the various post-docs I have worked with. Yu-Hung Lien and Giovanni Barontini were both immensely helpful when I was a new student and unfamiliar with the techniques required to trap and cool Rubidium. After they moved on, we were soon joined by Indranil Dutta. As someone who had just come from a well-established atom interferometry experiment, he was a welcome addition to our project. I owe him a great deal for everything he taught me about how to build an interferometer and to diagnose the inevitable problems along the way. Later on, we were joined by Joe Cotter and Teodor Krastev, who were both very helpful in developing the interferometer into a more robust device. Joe was. Theo's expert Then there are the other students on the Navigator project. It was a great pleasure working with Xiaxi Cheng as he was always willing to work on understanding the problem at hand. The next stage of the project is being undertaken by Shane de Souza and Nicola Bilton. I have enjoyed working with the both of them and being able to pass on some of the knowledge that I have learned to them. I wish them all the best for the continuation of their PhDs.

I have thoroughly enjoyed working as part of CCM. The friendly, collaborative environment, as well as the social cohesion of the group is something often hard to come by. I would like to particularly acknowledge Kyle Jarvis and Dylan Sabulsky. The three of us started our PhDs together, and I feel that we have a lot of shared experiences of life as PhD students, both positive and negative. I also owe a great deal of thanks to Sanja Maricic and Jon Dyne. Without Sanja's ability to deal with the complex and intricate details of Imperial College's administration and Jon's expertise at turning any Inventor design into a precision-engineered component, I am certain my PhD would have gone much differently.

Finally, I would like to acknowledge people within my personal life who have helped me get to where I am today. My family and in particular my parents, Siân and Carl, have been very supportive of my choices in life. I am grateful for everything they have given me. Last, but by no means least, I would like to thank Vickie for our time together. She has encouraged me to pursue the things I enjoy and to focus on the positive aspects of work, as well as life. Even when we were thousands of miles apart, she continued to offer her kind words of encouragement and I will forever be grateful for her unique support.

Contents

| | |
|---|-----------|
| List of figures | xi |
| List of tables | xv |
| 1 Introduction | 1 |
| 1.1 Light-Pulse Atom Interferometry | 1 |
| 1.2 Application to Inertial Navigation | 2 |
| 1.3 Aims | 3 |
| 1.4 Note on Units | 4 |
| 1.5 Structure of this Thesis | 4 |
| 2 Theory | 6 |
| 2.1 Chapter Overview | 6 |
| 2.2 Light-Pulse Matter-Wave Interference | 7 |
| 2.2.1 The Mach-Zehnder Scheme | 7 |
| 2.2.2 Phase Shift Contributions | 9 |
| 2.3 Raman Transitions in Rubidium-87 | 13 |
| 2.3.1 State Propagation | 15 |
| 2.3.2 Application to a Sequence of Raman Pulses | 17 |
| 2.3.3 Extending to a Real Atomic System | 18 |
| 2.4 Applications to Rubidium-87 | 19 |
| 2.4.1 Atomic Structure | 20 |
| 2.4.2 Driving Raman Transitions | 20 |
| 2.4.3 The Double Interferometer | 23 |
| 2.5 Conclusion | 25 |
| 3 MOTMaster | 26 |
| 3.1 Chapter Overview | 26 |
| 3.2 Motivation | 27 |

| | | |
|----------|--|-----------|
| 3.3 | Interfacing with Hardware | 28 |
| 3.3.1 | Hardware Abstraction | 29 |
| 3.3.2 | Voltage Pattern Generation | 30 |
| 3.3.3 | Timed Serial Communication | 31 |
| 3.3.4 | Voltage Acquisition | 32 |
| 3.4 | MOTMaster Sequences | 33 |
| 3.4.1 | Sequence Structure | 33 |
| 3.4.2 | Running a Sequence | 35 |
| 3.5 | Experiment Control Hardware | 36 |
| 3.6 | Experimental Sequence Overview | 38 |
| 4 | Cooling and Trapping in a MOT | 40 |
| 4.1 | Chapter Overview | 40 |
| 4.2 | The Navigator Vacuum Chamber | 40 |
| 4.2.1 | The 2D MOT system | 43 |
| 4.2.2 | The 3D MOT system | 46 |
| 4.2.3 | CCD Imaging | 50 |
| 4.3 | Generating MOT light | 53 |
| 4.3.1 | Absolute Frequency Reference | 54 |
| 4.3.2 | Cooling and Repump Light | 54 |
| 4.3.3 | Real-Time Control | 59 |
| 4.4 | Controlling the MOTs | 59 |
| 4.4.1 | Optical Fibre Network | 60 |
| 4.4.2 | Magnetic Field Control | 60 |
| 4.5 | Characterising the MOTs | 63 |
| 4.5.1 | 3D MOT Loading Rate | 65 |
| 4.6 | Conclusion | 66 |
| 5 | Preparing Atoms for Interferometry | 69 |
| 5.1 | Chapter Overview | 69 |
| 5.2 | Cooling in Optical Molasses | 70 |
| 5.2.1 | Motivation for Launching | 70 |
| 5.2.2 | Frequency and Power Control | 71 |
| 5.2.3 | Launching in a Moving Molasses | 71 |
| 5.2.4 | Imaging the Atom Cloud over Time | 74 |
| 5.3 | State Preparation | 79 |
| 5.3.1 | Schemes for Preparation | 79 |

| | | |
|----------|--|------------|
| 5.3.2 | Optically Pumping the Atoms | 80 |
| 5.3.3 | The Microwave Transitions | 86 |
| 5.3.4 | Blow-Away | 88 |
| 5.4 | Conclusion | 89 |
| 6 | Raman Optical System | 91 |
| 6.1 | Chapter Outline | 91 |
| 6.2 | Requirements | 91 |
| 6.2.1 | Gradients of Intensity | 92 |
| 6.2.2 | Wavefront Distortions | 95 |
| 6.3 | Raman Optics | 100 |
| 6.3.1 | Component Overview | 102 |
| 6.3.2 | Measuring the Beam Width | 103 |
| 6.4 | Retro-Reflection Assembly | 104 |
| 6.4.1 | In-Situ Alignment and Optimisation | 106 |
| 6.4.2 | The Mechanical Accelerometer | 109 |
| 6.5 | Conclusion | 110 |
| 7 | Acceleration-Sensitive Interference | 111 |
| 7.1 | Chapter Outline | 111 |
| 7.2 | The M-Squared Laser System | 112 |
| 7.2.1 | Laser System Overview | 112 |
| 7.2.2 | Frequency and Phase Control | 114 |
| 7.2.3 | The DCS Module | 115 |
| 7.3 | Atom Detection | 116 |
| 7.3.1 | Optical Setup | 116 |
| 7.3.2 | Detection using σ^+ transitions | 119 |
| 7.3.3 | Measuring the Occupation Probability | 124 |
| 7.4 | Individual Pulse Characterisation | 126 |
| 7.4.1 | Raman Transition Spectrum | 127 |
| 7.4.2 | Cancelling the Differential ac Stark Shift | 130 |
| 7.4.3 | Velocity-Selective Pulse | 132 |
| 7.4.4 | Interferometer Pulses | 137 |
| 7.5 | Noise | 137 |
| 7.5.1 | Detection Noise | 139 |
| 7.5.2 | Acceleration Uncertainty | 144 |
| 7.5.3 | The Allan Variance | 145 |

| | | |
|---------------------|--|------------|
| 7.5.4 | The Sensitivity Function $g(t)$ | 146 |
| 7.5.5 | The Interferometer Transfer Function $H(\omega)$ | 147 |
| 7.5.6 | Vibrations | 151 |
| 7.5.7 | Summary of Identified Noise Sources | 157 |
| 7.6 | Measuring Accelerations | 158 |
| 7.6.1 | Fringe Calibration | 158 |
| 7.6.2 | Comparing the atom accelerometer with the MEMS accelerometer | 159 |
| 7.6.3 | Expected vs observed Allan deviation | 162 |
| 7.7 | Conclusion | 163 |
| 8 | Outlook | 165 |
| 8.1 | Conclusions | 165 |
| 8.2 | Avenues of Further Research | 167 |
| 8.3 | Concluding Remarks | 169 |
| Bibliography | | 171 |
| Acronyms | | 181 |

List of figures

| | | |
|-----|--|----|
| 2.1 | Mach-Zehnder atom interferometer configuration. | 8 |
| 2.2 | Interferemeter paths under constant acceleration | 11 |
| 2.3 | Schematic diagram of a raman transition. | 15 |
| 2.4 | Rubidium-87 D2 transition hyperfine structure. | 21 |
| 2.5 | Raman beam configuration. | 24 |
| 2.6 | Interferometer paths with two oppositely directed Raman transitions.. | 24 |
| 3.1 | Schematic diagram of MOTMaster and hardware interface. | 28 |
| 3.2 | Scripted pattern generation for an NI-HSDIO card | 31 |
| 3.3 | Timing diagram for serial communication | 32 |
| 3.4 | MOTMaster user interface | 34 |
| 3.5 | Control hardware schematic diagram | 38 |
| 4.1 | Magneto-optical Trap (MOT) system component diagram | 42 |
| 4.2 | Schematic for the 2D MOT | 44 |
| 4.3 | Optical components for the 2D MOT | 45 |
| 4.4 | Calculated field and field gradients for the 2D MOT quadrupole coils . | 47 |
| 4.5 | MOT coil temperature rise | 49 |
| 4.6 | Measured magnetic field for the 3D MOT coils | 49 |
| 4.7 | Optical setup for CCD imaging | 51 |

| | | |
|------|--|----|
| 4.8 | Integrated pixel counts as a function of CCD exposure time. | 53 |
| 4.9 | μ Quans Laser System Diagram | 55 |
| 4.10 | Saturated absorption spectroscopy of the Muquans master laser. | 56 |
| 4.11 | Error Signal for the μ Quans master servo. | 56 |
| 4.12 | Error Signal for the μ Quans Cooling laser. | 57 |
| 4.13 | Cooling power vs. Acousto-optic Modulator (AOM) control voltage. . | 58 |
| 4.14 | Network of optical fibre splitters and AOMs for MOTlight distribution | 61 |
| 4.15 | Circuit diagram for 3D MOT quadrupole coils and bias field coils. . . | 62 |
| 4.16 | IGBT circuit for the 2D MOT quadrupole coils | 63 |
| 4.17 | MOT loading timing diagram. | 64 |
| 4.18 | 3D MOT atom number vs dispenser current with and without a push beam. | 67 |
| 5.1 | Molasses stage timing diagram | 72 |
| 5.2 | Beam configuration for a moving molasses | 73 |
| 5.3 | Atom cloud position after launching in a moving molasses | 74 |
| 5.4 | Integrated pixel counts during ballistic expansion. | 76 |
| 5.5 | Temperature measurement using ballistic expansion | 76 |
| 5.6 | Atom cloud centre-of-mass over time | 78 |
| 5.7 | State preparation pulse sequence | 81 |
| 5.8 | State selection timing schematic | 81 |
| 5.9 | Ground state distribution during $ F = 2\rangle \rightarrow F' = 2\rangle$ pumping | 82 |
| 5.10 | m_F populations before and after $ F = 1\rangle \rightarrow F' = 0\rangle$ pumping | 84 |
| 5.11 | $ 1, m_F\rangle$ populations for increasing $ F = 1\rangle \rightarrow F' = 0\rangle$ pumping time. . | 85 |
| 5.12 | Setup for Microwaves | 86 |
| 5.13 | Microwave transition spectrum | 88 |

| | | |
|------|--|-----|
| 5.14 | Microwave Rabi oscillation between $ 1, 0\rangle$ and $ 2, 0\rangle$ | 89 |
| 6.1 | Simulated fringe contrast vs beam waist size | 94 |
| 6.2 | Simulated fringe contrast vs beam waist size including a thermal velocity distribution. | 95 |
| 6.3 | Wavefront distortion and interferometer phase error for diverging Raman beams. | 97 |
| 6.4 | Tilted Raman beams with perfect retro-reflection. | 98 |
| 6.5 | Imperfect retro-reflection with a tilted incoming beam. | 98 |
| 6.6 | Expected fringe contrast as a function of random phase contributions. | 100 |
| 6.7 | Drawings of the components used in the Raman optics assemblies | 101 |
| 6.8 | Raman beam intensity profile and beam waist. | 104 |
| 6.9 | Quarter-wave plate thickness variation. | 105 |
| 6.10 | Automatic mirror alignment using the Nelder-Mead simplex algorithm. | 108 |
| 6.11 | Innalabs accelerometer cross-section | 110 |
| 7.1 | M-Squared Laser System Schematic | 113 |
| 7.2 | DCS Module User interface | 117 |
| 7.3 | Optical setup for Photodiode Detection | 118 |
| 7.4 | Scheme to invert beam polarisation. | 119 |
| 7.5 | State detection sequence timing | 121 |
| 7.6 | Photodiode output voltage for increasing detection beam intensity. | 123 |
| 7.7 | Photodiode voltages during atom detection for varying detection times. | 123 |
| 7.8 | Raman transition spectrum | 128 |
| 7.9 | $\Delta m = 0$ transition spectrum. | 129 |
| 7.10 | Differential ac Stark shift as a function of two-photon detuning and Raman beam intensities. | 133 |

| | | |
|------|---|-----|
| 7.11 | Raman transition spectrum after cancelling the differential ac Stark shift. | 134 |
| 7.12 | Simulated velocity distribution after a Raman π pulse. | 135 |
| 7.13 | $ F = 2\rangle$ population after a velocity-selective Raman π pulse. | 136 |
| 7.14 | Rabi oscillations between the $ 1, 0\rangle$ and $ 2, 0\rangle$ states. | 138 |
| 7.15 | Power spectral density of the amplified photodiode voltage. | 143 |
| 7.16 | Detector noise vs. integration time. | 143 |
| 7.17 | Transfer function for Raman phase noise. | 148 |
| 7.18 | Interferometer phase noise due to the Raman phase | 150 |
| 7.19 | Allan deviation of the interferometer phase due to the Raman laser phase. | 151 |
| 7.20 | Acceleration noise transfer function. | 153 |
| 7.21 | Interferometer power spectral density due to vibration noise. | 155 |
| 7.22 | Calculated Allan deviation of the interferometer phase from vibration noise. | 156 |
| 7.23 | Interference fringe for $T = 25$ ms. | 159 |
| 7.24 | MEMS/Interferometer correlation in a low vibration environment. . . | 161 |
| 7.25 | MEMS accelerometer and transition probability in high vibration noise | 162 |
| 7.26 | Comparison of Allan deviation in a high and low vibration environment. | 164 |
| 8.1 | Demonstration of the atom interferometer as a mobile sensor of a range of horizontal accelerations at the UK National Quantum Technologies Showcase in November 2018. | 168 |

List of tables

| | | |
|-----|--|-----|
| 4.1 | Table of parameters for each 3D MOT bias coil. | 50 |
| 4.2 | Typical optical and magnetic parameters for the Magneto-optical Traps (MOTs). | 64 |
| 7.1 | Allowed polarisation configurations for a Raman transition coupling $ F = 1, m_F\rangle \rightarrow F = 2, m_F + \Delta m\rangle$ | 128 |
| 7.2 | Allan variance characteristic timescales. | 145 |
| 7.3 | Comparison of known noise sources. | 157 |

“I may not have gone where I intended to go, but I think I have ended up where I needed to be”

— Douglas Adams

Chapter 1

Introduction

1.1 Light-Pulse Atom Interferometry

The development of quantum theory to explain the wave-like behaviour of matter has enabled significant advances in science and technology. An early example of this is the atomic clock [1], which makes use of the interference between two atomic internal states to precisely measure their transition frequency. This technology has led to a re-definition of the second in terms of physical constants, as well as a globally-adopted standard for timekeeping [2] that supports many aspects of modern society. Early interferometers relied on driving microwave frequency transitions because the contemporary laser technology did not have the frequency stability or linewidths necessary to maintain coherence between the atomic states. It was later suggested that interference of matter-waves could be used to make sensitive measurements of accelerations and rotations [3]. This sensitivity is increased using the large momentum recoil of optical frequency transitions to make an interferometer using successive pulses of light [4].

Kasevich and Chu demonstrated inertial force sensing using atom interferometry with a measurement of gravitational acceleration [5, 6]. Subsequent work showed that atom interferometers were also able to measure rotations [7, 8]. As inertial sensors, these experiments showed comparable short-term sensitivities to their classical counterparts. By contrast, their long-term stability was noteworthy. This is due to the frequency-stability of the atomic transition and in the lasers used to stimulate it. Again, this is analogous to atomic clock systems which are able to reach very low fractional uncertainties by integrating over long timescales [9].

1.2 Application to Inertial Navigation

Mobile applications of atom interferometry as inertial sensors have demonstrated both high sensitivity and long-term stability outside of laboratory environments [10]. Experiments during the parabolic flight of an aircraft have also demonstrated measurements of acceleration around 0 g and 1 g [11, 12]. The ability to precisely measure a range of accelerations over long durations is of great practical interest for inertial navigation systems. These measure the position of a moving body using successive measurements of its acceleration and rotation, known as dead reckoning. The accuracy of this method depends on the intrinsic noise of each sensor, as well as their bias. If the noise is known *a priori*, then a statistical method such as a Kalman filter [13] can be used to produce a more accurate estimate of the position. However, the error from a bias tends to dominate over long timescales. For instance, the position error from a constant acceleration bias grows quadratically with time. This problem is compounded by the fact that the bias in an inertial sensor drifts over time due to physical effects such as temperature variation and mechanical strain. This bias instability means that inertial navigation systems require regular re-calibration and an external method of correcting for the position error such as Global Navigation Satellite System (GNSS) [14].

One drawback of atom interferometers is the interrogation time needed between each laser pulse. This leads to a sensitivity bandwidth of the order of 10 Hz. It should be noted that acceleration bandwidths as high as 60 Hz [15] and even 10 kHz [16] using short, high-power pulses have been reported, but these are at the cost of a reduction in sensitivity. A further issue is the measurement dead time as a result of the time required to prepare a cold ensemble of atoms. During this preparation time, the system does not respond to any acceleration or rotation acting on the atoms. It has been suggested that this shortcoming can be counteracted by combining the interferometer with a mechanical accelerometer [17] or by interleaving multiple cold atom interferometers. The latter of these has been demonstrated in a gyroscope [18], but is technically more challenging.

Hybridising an atom interferometer with a classical sensor results in a composite system which aims for both long-term stability and high bandwidth. Indeed, a secondary measurement is needed to determine the interferometer fringe order and hence obtain an absolute value of acceleration. This is of particular importance for inertial navigation, where the range of acceleration is far greater than the fringe period [19]. This auxiliary sensor can also improve the sensitivity of the interferometer in high vibration environments [20], which is a significant source of phase noise. Measuring these vibrations provides a method of filtering their effect from the interferometer signal.

1.3 Aims

This aim of this project was to investigate the use of atom interferometry in the context of inertial navigation by measuring horizontal accelerations. Gravitational acceleration induces motion transverse to the laser wavefront. Together with the requirements

of high acceleration sensitivity and minimal dead-time, this influenced the technical aspects of this experiment.

1.4 Note on Units

In subsequent chapters of this thesis, various non-SI units are used for convenience.

The commonly used ones are defined here:

- $1 \text{ G} = 1 \times 10^{-4} \text{ T}$ (Gauss - cgs unit of magnetic flux density)
- $g = 9.806\,65 \text{ m s}^{-2}$ (international standard of gravitational acceleration, measured at 45° latitude and sea level [22])
- $I_{\text{sat}} = 1.38 \text{ mW cm}^{-2}$ (saturation intensity for the $|F = 2, 2\rangle \rightarrow |F' = 3, 3\rangle$ cycling transition in Rubidium-87)
- $\Gamma = 2\pi \times 6.065 \text{ MHz}$ (natural linewidth of the above transition)

1.5 Structure of this Thesis

This thesis is structured as follows:

- **Chapter 2** presents a theoretical introduction to matter-wave interferometry and the relevant atomic structure of Rubidium-87.
- **Chapter 3** describes the software used to control the experiment and acquire data.
- **Chapter 4** outlines the preliminary cooling and trapping of Rubidium-87 in a MOT.

- **Chapter 5** discusses the techniques used to further cool the atoms and prepare an ensemble in a suitable single internal state,
- **Chapter 6** gives a detailed description of the in-vacuum optical system for driving Raman transitions.
- **Chapter 7** characterises the interferometer's sensitivity to accelerations.
- **Chapter 8** summarises the conclusions of this thesis and outlines further work towards improving the accelerometer.

Chapter 2

Theory

2.1 Chapter Overview

This chapter presents a theoretical discussion of the interaction between light and matter that forms the basis of atom interferometry. It begins with a review of the theory of matter-wave interference and its application to measuring inertial forces such as accelerations in Section 2.2. This is followed by a derivation of the equations of motion for a Raman transition in a simplified three-level atom in Section 2.3. Finally, this chapter concludes with a discussion of the atomic structure of Rubidium-87 (^{87}Rb), focussing on the aspects relevant to the previously mentioned phenomena.

This chapter assumes some prior understanding of light-matter interactions on the part of the reader. A comprehensive description of the semi-classical approximation to atom-light interactions can be found in [23]. Theories of laser cooling and magneto-optical trapping are of interest for some experimental aspects of these thesis. Details of these can be found in [24]. For an exact derivation of the two-level approximation to the Raman transition, the reader is referred to [25].

2.2 Light-Pulse Matter-Wave Interference

A cornerstone of quantum mechanics is the wave-like evolution of quantum states as described by the Schrödinger equation. As a consequence of this, it is possible to create superpositions of states that evolve coherently. Furthermore, these states can interfere with each other if their wavefunctions overlap. The interference pattern depends on the difference in phase between the two paths.

In this section, the theory of matter-wave interference using pulses of laser light is presented. It begins in Section 2.2.1 with a description of the $\pi/2 - \pi - \pi/2$ pulse sequence that forms an analogue of the Mach-Zehnder interferometer. This is followed in Section 2.2.2 by a derivation of the interferometer phase. In particular, it is shown that this depends upon the acceleration of the atom during the interferometer.

2.2.1 The Mach-Zehnder Scheme

One method for realising matter-wave interference is the Ramsey-Bordé interferometer [26]. This requires an ensemble of atoms that can be driven between two states using an interaction with a laser field. The absorption and stimulated emission of photons exchanges momentum between the atom and the light such that the state of the atom is defined as a product of its internal states and momentum eigenstates, labelled as $|1, \mathbf{p}\rangle$ and $|2, \mathbf{p} + \hbar\mathbf{k}\rangle$. When compared with conventional optical interferometry, it is the light which alters the trajectory of the matter, rather than the other way around. Indeed, laser pulses with pulse areas of $\pi/2$ and π are analogous to beam-splitters and mirrors in optical systems.

A three pulse interferometer is the simplest configuration for which the two trajectories can overlap after separation. Schematically, this is shown in Figure 2.1. An atom in

$|1, \mathbf{p}\rangle$ is driven into a superposition of two states using a $\pi/2$ pulse. The wavepacket in $|2, \mathbf{p} + \hbar\mathbf{k}\rangle$ has a different momentum, so the two become spatially separated. After a time T , a π pulse inverts the state along each path, so that after another duration of T the two wavepackets overlap. These are recombined by a final $\pi/2$ pulse. The interference between the two states is manifested in their population, which depends on the phase difference between the two paths. This phase difference Φ is expressed as follows

$$\Phi = \Phi_{\text{prop}} + \Phi_{\text{int}} + \Phi_{\text{laser}} \quad (2.1)$$

where Φ_{prop} is the phase difference due to propagation along each path, Φ_{int} is the phase difference due to evolution of the internal state and Φ_{laser} is the phase difference caused by interactions with the laser field.

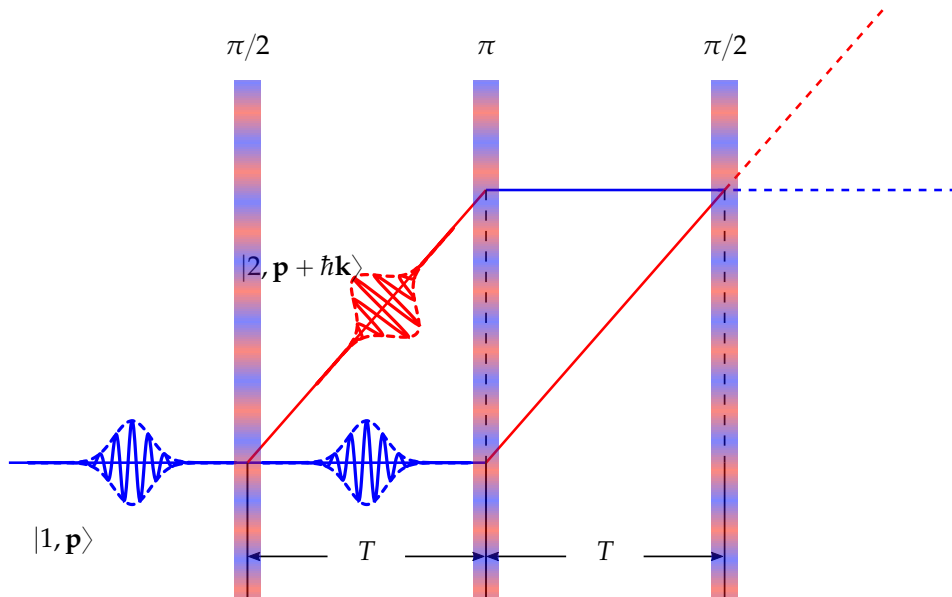


Figure 2.1: Mach-Zehnder atom interferometer configuration. A sequence of laser pulses are used to drive an atom into a superposition of two states. When the two paths overlap at the final $\pi/2$ pulse, they interfere with each other. The final occupation probability is proportional to the phase difference between the two paths.

2.2.2 Phase Shift Contributions

Propagation Phase

The propagation phase can be evaluated using the path integral approach to quantum mechanics. The trajectory of a quantum state is obtained by integrating over all possible paths. The total amplitude for arriving at position x_b at t_b , starting from x_a at t_a is given by the following propagator

$$K(t_b, x_b, t_a, x_a) = \int_{x_a}^{x_b} e^{iS/\hbar} dx(t) \quad (2.2)$$

where $x_b \equiv x(t_b)$ and similarly for x_a . The action S along a path is defined using the Lagrangian of the system

$$S = \int_{t_a}^{t_b} L(x, \dot{x}) dt \quad (2.3)$$

and the classical limit is recovered when the action $S_{\text{cl}} \gg \hbar$. In this case, most paths destructively interfere as their phases oscillate rapidly. Along the classical path, the action is minimised. Paths close to this lead to constructive interference, so the trajectory of the system is well-described using the Euler-Lagrange equations. Under this condition, it can be shown [27] that for a plane wave, the propagation phase is proportional to the action along the classical path

$$\Phi_{\text{prop}} = \frac{1}{\hbar} S_{\text{cl}}(t_b, x_b, t_a, x_a) \quad (2.4)$$

This is indeed the case for an atom interferometer. When considering a single atom under a constant acceleration, the Lagrangian is given by

$$L = \frac{1}{2}m\dot{x}^2 + max \quad (2.5)$$

so that its position and velocity are given by

$$x(t) = x_a + v_a(t - t_a) + \frac{1}{2}a(t - t_a)^2 \quad (2.6a)$$

$$v(t) = v_a + a(t - t_a) \quad (2.6b)$$

for initial values of position (x_a), velocity (v_a) and time (t_a). Using equation (2.3), the action is given by

$$S(t_b, x_b, t_a, x_a) = \frac{m(x_b - x_a)^2}{2(t_b - t_a)} + \frac{ma(x_b + x_a)(t_b - t_a)}{2} - \frac{ma^2(t_b - t_a)^3}{24} \quad (2.7)$$

The trajectories along each interferometer path under acceleration are shown in Figure 2.2. Denoting $S_{ac} \equiv S(T, x_c, 0, x_a)$ and likewise for the other co-ordinates, the difference in the action along the upper and lower paths is

$$\begin{aligned} S_{ac} + S_{cd} - (S_{ab} + S_{bd}) &= -\frac{m(x_b - x_c)(aT^2 - x_a + x_b + x_c - x_d)}{T} \\ &= -\frac{m(x'_b - x'_c)((x'_c - x'_a) - (x'_d - x'_b))}{T} \end{aligned} \quad (2.8)$$

The second expression is obtained using $x_b - x'_b = x_c - x'_c = \frac{1}{2}aT^2$ and $x_d - x'_d = 2aT^2$, where the primes indicate positions in the absence of acceleration. The last factor in the numerator of equation (2.8) is zero because the paths enclose a parallelogram for which $x'_c - x'_a = x'_d - x'_b$. It follows from equation (2.4) that there is no difference in the propagation phase along the two paths acd (ϕ_{prop}^u) and abd (ϕ_{prop}^l). In other words, $\Phi_{\text{prop}} \equiv \phi_{\text{prop}}^u - \phi_{\text{prop}}^l = 0$ when there is a constant acceleration of the atom.

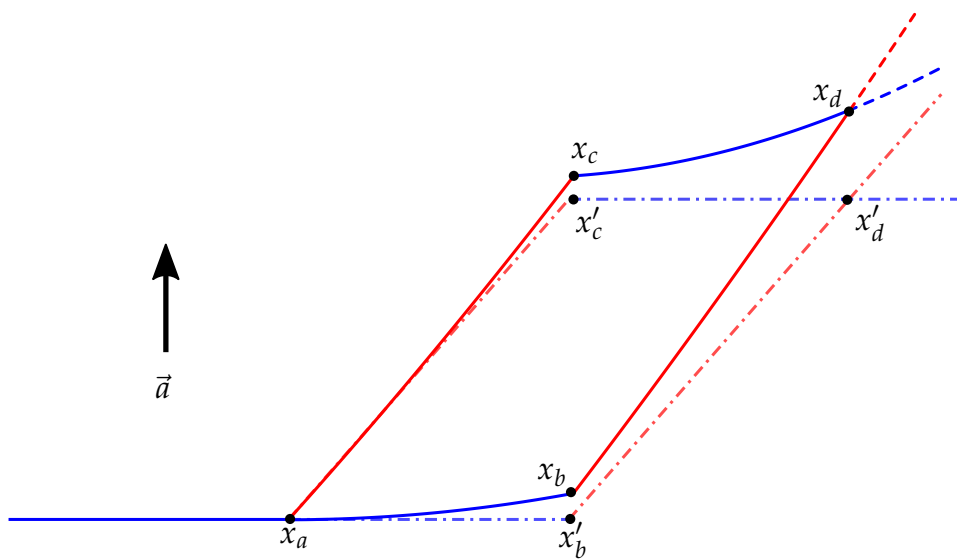


Figure 2.2: Interferometer paths under a constant acceleration. The dashed lines indicate the trajectories under zero acceleration.

Internal State Evolution

Between each laser pulse, the internal state of the atom evolves freely. Therefore, the phase due to this evolution is given by

$$\phi^{(j)}(t_a, t_b) = \int_{t_a}^{t_b} \omega_j t \, dt \quad (2.9)$$

where $\hbar\omega_j$ is the internal energy of the atom along that trajectory. The phase difference due to the internal state evolution is

$$\Phi_{\text{int}} = \phi^{(2)}(t_1, t_2) + \phi^{(1)}(t_2, t_3) - (\phi^{(1)}(t_1, t_2) + \phi^{(2)}(t_2, t_3)) \quad (2.10)$$

which is zero if the time between successive pulses is the same and the energy of each state does not vary. The possibility of energy variation is important when considering the effects of the ac Stark shift and is addressed subsequently in Section 7.4.2.

Laser Phase

Finally, there is the contribution from the laser phase. During each transition, the phase of the laser modifies the state of the atom. The propagator that describes this transition for arbitrary Rabi frequencies and detuning is derived below, in Section 2.3. For now, it is sufficient to focus on the ideal case of perfect pulse areas and zero detuning. The first and third pulses have pulse areas of $\pi/2$, which modifies the two states as follows

$$U_{\pi/2}(\phi) |1\rangle = \frac{1}{\sqrt{2}} |1\rangle + \frac{e^{-i\phi}}{\sqrt{2}} |2\rangle \quad (2.11a)$$

$$U_{\pi/2}(\phi) |2\rangle = \frac{e^{i\phi}}{\sqrt{2}} |1\rangle + \frac{1}{\sqrt{2}} |2\rangle \quad (2.11b)$$

where $\phi = \mathbf{k} \cdot \mathbf{x} - \omega_L t + \phi_0$ is the phase of the light driving the transition in the atom at position \mathbf{x} . The middle pulse has a π pulse area whose interaction is described by

$$U_\pi(\phi) |1\rangle = e^{-i\phi} |2\rangle \quad (2.12a)$$

$$U_\pi(\phi) |2\rangle = e^{i\phi} |1\rangle \quad (2.12b)$$

At the output corresponding to the state $|1\rangle$, the phases along the upper and lower path are then

$$\phi_l = \mathbf{k} \cdot (\mathbf{x}_d - \mathbf{x}_b) - \omega_L T + (\phi_0)_3 - (\phi_0)_2 \quad (2.13a)$$

$$\phi_u = \mathbf{k} \cdot (\mathbf{x}_c - \mathbf{x}_a) - \omega_L T + (\phi_0)_2 - (\phi_0)_1 \quad (2.13b)$$

$$(2.13c)$$

where $(\phi_0)_j$ refers to the phase of the laser at the j -th light pulse. Following the same argument used in equation (2.8), this can be simplified so that the phase difference

due to the laser interaction $(\phi_u - \phi_l)$, and hence the total phase difference, is

$$\Phi_{\text{laser}} = \mathbf{k} \cdot \mathbf{a} T^2 - (\phi_0)_1 + 2(\phi_0)_2 - (\phi_0)_3 \quad (2.14)$$

In summary, the phase difference along the two paths of the interferometer comes not from the atomic motion along the path, nor from the phase evolution of the internal states, but rather the position-dependent phase of the light field, which is impressed on the atom each time a transition is driven. In other words, $\Phi = \Phi_{\text{laser}}$. This makes a phase difference of $\mathbf{k} \cdot \mathbf{a} T^2$. In addition, if the phase of the light is adjusted between pulses, there is a further interferometer phase of $-(\phi_0)_1 + 2(\phi_0)_2 - (\phi_0)_3$. This second part vanishes if the phase of the light is undisturbed between pulses.

2.3 Raman Transitions in Rubidium-87

In this section, an analysis of the dynamics of the stimulated Raman transition is presented. This is modeled as an effective transition between two ground states $|1\rangle$ and $|2\rangle$. These two states are coupled via an intermediate state $|i\rangle$ which can be adiabatically eliminated when the two light fields are sufficiently detuned from resonance. An explicit derivation of this process can be found elsewhere [28, 29]. The key results, which aid the discussion of the performance of the interferometer in subsequent chapters, are summarised below. Following this, a propagator is derived which describes the evolution of the atomic state during a Raman transition. This is used to derive the final state after the interferometer pulse sequence. Modeling the atomic system in this way makes it possible to consider the effects of finite pulse duration, detuning and intensity on the final state.

The energy level scheme for a Raman transition is shown in Figure 2.3. Each ground state is coupled to the intermediate state $|i\rangle$ by an interaction with an electric field

$\mathbf{E}_j = \mathbf{E}_{0,j} \cos(\omega_j^l t - \mathbf{k}_j \cdot \mathbf{x} + \phi_j)$. The strength of this interaction is defined by the Rabi frequency

$$\Omega_j = \frac{1}{\hbar} \langle j | -\mathbf{d} \cdot \mathbf{E}_{0,j} | i \rangle e^{i\phi_j} \quad (2.15)$$

where \mathbf{d} is the dipole operator. Referring to Figure 2.3, it is assumed that $\omega_{\text{hfs}} \gg \Delta \gg \delta$, so that \mathbf{E}_1 couples only to state $|1\rangle$ and \mathbf{E}_2 couples only to state $|2\rangle$. When Δ is sufficiently large, the frequency of the two fields are far off-resonant from their corresponding transition frequencies that couple $|F = j\rangle \rightarrow |F' = i\rangle$. In this case, the population of the intermediate state remains small. This state can be adiabatically eliminated to result in an effective two-level system. The interference of the two fields means that the transition can be represented by an interaction with an effective field with the following parameters

$$\omega_{\text{eff}} = \omega_1^l - \omega_2^l \quad (2.16a)$$

$$\phi_{\text{eff}} = \phi_1 - \phi_2 \quad (2.16b)$$

$$\mathbf{k}_{\text{eff}} = \mathbf{k}_1 - \mathbf{k}_2 \quad (2.16c)$$

$\approx 2\mathbf{k}_1$ (because the beams will be counter-propagating)

The resonance condition for the Raman transition is given by

$$\delta = \omega_{\text{eff}} - \left[\omega_{\text{hfs}} + \mathbf{k}_{\text{eff}} \cdot \mathbf{v} + \frac{\hbar |\mathbf{k}_{\text{eff}}|^2}{2m} \right] \quad (2.17)$$

Here, the second term in the square brackets is the Doppler shift for an atom with velocity \mathbf{v} and the third is the recoil shift.

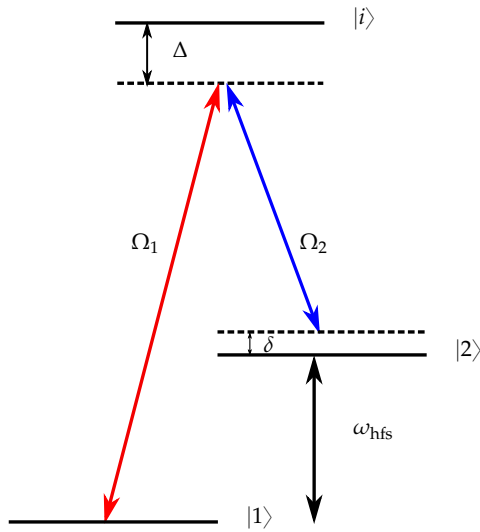


Figure 2.3: Schematic diagram of a Raman transition. Two states, $|1\rangle$ and $|2\rangle$, are coupled to each other via an intermediate state $|i\rangle$. When Δ is large enough (see text) $|i\rangle$ can be adiabatically eliminated, resulting in an effective two-level system.

2.3.1 State Propagation

To describe the dynamics of the Raman transition, it is convenient to express the system in the interaction picture. This allows the Hamiltonian to be represented in a time-independent form. An analytic solution to the equations of motion can then be obtained, which describes the evolution of the atomic state during a Raman transition. After adiabatically eliminating the intermediate state [28], the state of the atom in a rotating frame is given by

$$|\psi\rangle = c_1 e^{-i\omega_1 t} |1\rangle + c_2 e^{-i(\omega_2 + \delta)t} |2\rangle \quad (2.18)$$

The Hamiltonian can be simplified by making the rotating wave approximation, which neglects the rapidly oscillating terms. After this, the Schrödinger equation becomes

$$i \begin{pmatrix} \dot{c}_1 \\ \dot{c}_2 \end{pmatrix} = \frac{1}{2} \begin{pmatrix} -\Omega_1^{ac} & \Omega_{\text{eff}} \\ \Omega_{\text{eff}}^* & -2\delta - \Omega_2^{ac} \end{pmatrix} \begin{pmatrix} c_1 \\ c_2 \end{pmatrix} \quad (2.19)$$

Where in terms of the single-photon Rabi frequencies Ω_1 and Ω_2 , the ac Stark shifts Ω_j^{ac} and effective Rabi frequency Ω_{eff} are given by

$$\Omega_j^{\text{ac}} = -\frac{|\Omega_j|^2}{2\Delta} \quad (2.20\text{a})$$

$$\Omega_{\text{eff}} = \frac{e^{i\phi_{\text{eff}}} |\Omega_1| |\Omega_2|}{2\Delta} \quad (2.20\text{b})$$

where the contribution of δ to the one-photon detuning of the $|F = 2\rangle \rightarrow |F' = i\rangle$ transition has been neglected compared with Δ . The phase of the Rabi frequency is determined by ϕ_{eff} , which was previously defined in equation (2.16b). Under an appropriate choice of intensities and two-photon detuning, it is possible to cancel the differential ac Stark shift $\Omega_1^{\text{ac}} - \Omega_2^{\text{ac}}$ (see Section 7.4.2 for further details on this). Therefore, they can be omitted from equation (2.19) so that after solving the Schrödinger equation, the coefficients c_1, c_2 evolve according to

$$\begin{pmatrix} c_1(t) \\ c_2(t) \end{pmatrix} = U \begin{pmatrix} c_1(0) \\ c_2(0) \end{pmatrix} \quad (2.21)$$

where the propagator U is

$$U = e^{\frac{1}{2}i\delta t} \begin{pmatrix} \cos\left(\frac{\Omega't}{2}\right) - i\frac{\delta}{\Omega'} \sin\left(\frac{\Omega't}{2}\right) & -ie^{i\phi_{\text{eff}}} \frac{\Omega_{\text{eff}}}{\Omega'} \sin\left(\frac{\Omega't}{2}\right) \\ -ie^{-i\phi_{\text{eff}}} \frac{\Omega_{\text{eff}}}{\Omega'} \sin\left(\frac{\Omega't}{2}\right) & \cos\left(\frac{\Omega't}{2}\right) + i\frac{\delta}{\Omega'} \sin\left(\frac{\Omega't}{2}\right) \end{pmatrix} \quad (2.22)$$

and $\Omega' = \sqrt{\delta^2 + \Omega_{\text{eff}}^2}$ is the generalised Rabi frequency [30]. After transforming back into the stationary frame, equation (2.22) becomes

$$U = \begin{pmatrix} e^{\frac{i(\omega_{\text{eff}} - \delta_R)t}{2}} \left(\cos\left(\frac{\Omega't}{2}\right) - i\frac{\delta}{\Omega'} \sin\left(\frac{\Omega't}{2}\right) \right) & -ie^{\frac{i(\omega_{\text{eff}} - \delta_R)t}{2}} e^{i\phi_{\text{eff}}} \frac{\Omega_{\text{eff}}}{\Omega'} \sin\left(\frac{\Omega't}{2}\right) \\ -ie^{\frac{-i(\omega_{\text{eff}} - \delta_R)t}{2}} e^{-i\phi_{\text{eff}}} \frac{\Omega_{\text{eff}}}{\Omega'} \sin\left(\frac{\Omega't}{2}\right) & e^{-\frac{i(\omega_{\text{eff}} - \delta_R)t}{2}} \left(\cos\left(\frac{\Omega't}{2}\right) + i\frac{\delta}{\Omega'} \sin\left(\frac{\Omega't}{2}\right) \right) \end{pmatrix} \quad (2.23)$$

where $\delta_R = \mathbf{k}_{\text{eff}} \cdot \mathbf{v} + \hbar |\mathbf{k}_{\text{eff}}|^2 / 2m$ is the Raman detuning from equation (2.17). If we consider an atom starting in the state $|1\rangle$, then it is straightforward to show that after applying U , the probability of stimulating a transition to $|2\rangle$ is given by

$$P_{|2\rangle} = \frac{\Omega_{\text{eff}}^2}{\Omega'^2} \sin^2\left(\frac{\Omega't}{2}\right) \quad (2.24)$$

2.3.2 Application to a Sequence of Raman Pulses

Now, this propagator can be used to determine the state of the atom after a sequence of Raman pulses. The propagator was derived using an initial state at $t = 0$. This can be generalised to an arbitrary time by replacing $t \rightarrow t - t_0$ and $\phi_{\text{eff}} \rightarrow \phi_{\text{eff}} + \omega_{\text{eff}}t_0$. Between successive Raman pulses, there is a period of free evolution for a time T . During this, the state evolves according to

$$F(T) = \begin{pmatrix} e^{-i\frac{\omega_{\text{hfs}}T}{2}} & 0 \\ 0 & e^{i\frac{\omega_{\text{hfs}}T}{2}} \end{pmatrix} \quad (2.25)$$

Treating the Rabi frequency, phase, detuning and pulse duration as free parameters denoted by an index $j = 1, 2, 3$, the state after three arbitrary pulses separated in time

is given by

$$|\psi\rangle = U(\Omega_3, \phi_3, \delta_3, \tau_3)F(T_2)U(\Omega_2, \phi_2, \delta_2, \tau_2)F(T_1)U(\Omega_1, \phi_1, \delta_1, \tau_1)|\psi_0\rangle \quad (2.26)$$

for an initial state $|\psi_0\rangle$. This expression is valid for arbitrary pulses and is useful when considering a distribution of intensities and Doppler detunings across an atomic ensemble. For instance, the occupation probability for $|2\rangle$ is given by

$$P_{|2\rangle} = |\langle 2|\psi\rangle|^2 \quad (2.27)$$

It is also useful to define the fringe contrast – the difference between the maximum and minimum of $P_{|2\rangle}$

$$c = \max_{\Phi} P_{|2\rangle} - \min_{\Phi} P_{|2\rangle} \quad (2.28)$$

which ranges between 0 and 1. This fringe contrast implicitly depends on the pulse area and detuning of each pulse. In the case of perfect pulse areas and zero detuning with the initial state $|\psi_0\rangle = |1\rangle$, equation (2.27) yields the following

$$\begin{aligned} P'_{|2\rangle} &= \sin\left(\frac{1}{2}(\phi_1 - 2\phi_2 + \phi_3)\right)^2 \\ &= \sin\left(\frac{\Phi}{2}\right)^2, \end{aligned} \quad (2.29)$$

where Φ is related to the acceleration of the atom in equation (2.14).

2.3.3 Extending to a Real Atomic System

In a real atomic system, there are many intermediate states which couple to the two ground states. This theory can be extended to consider the additional intermediate

states using their individual Rabi frequencies. In this case, the effective Rabi frequency is given by the following sum

$$\Omega_{\text{eff}} = e^{i\phi_{\text{eff}}} \sum_k \frac{|\Omega_{1k}| |\Omega_{2k}|}{2\Delta_k} \quad (2.30)$$

where the index k labels the intermediate states which couple to both $|1\rangle$ and $|2\rangle$. A similar expression can be obtained for the ac Stark shift terms. Note that the previous assumption that \mathbf{E}_1 only couples to the state $|1\rangle$, and similarly for \mathbf{E}_2 , is no longer valid. A full treatment includes the coupling of each field to each state. The effective Rabi frequency in equation (2.30) implicitly depends on the polarisation of the light. The individual Rabi frequencies Ω_{jk} are calculated using the Clebsch-Gordan coefficients that describe the coupling of angular momentum states. Further detail on calculating transition matrix elements of tensor operators can be found in [31].

2.4 Applications to Rubidium-87

This final section places what has been discussed thus far into the context of Rubidium-87, the atomic species used in this experiment. It begins in Section 2.4.1 with a presentation of the hyperfine structure in the $5S_{1/2}$ and $5P_{3/2}$ levels, used throughout this experiment for cooling and trapping, as well as interferometry. This is followed by an overview of the techniques used to drive counter-propagating Raman transitions in Section 2.4.2. In particular, this motivates the choice of polarisation used for the two Raman beams. Finally, this section concludes in Section 2.4.3 with a discussion of the two interferometer paths.

2.4.1 Atomic Structure

The $5S_{1/2}$ electronic ground state of Rubidium-87 has two hyperfine levels $F = 1$ and $F = 2$, split by 6.8 GHz. It can be efficiently laser cooled using one laser (the cooler) to scatter light from atoms in $F = 2$, and another (the repumper) to pump atoms out of $F = 1$ and into $F = 2$.

In addition to these, two hyperfine levels in its ground state provide suitable choices of states for interferometry. Neither decays spontaneously, which helps to preserve their coherence during interferometry. Particular pairs of Zeeman sub-levels can be identified which are coupled via a Raman transition. When the two laser fields are counter-propagating, the photon recoil imparts 10^5 times more momentum than the one-photon 6.8 GHz microwave transition. This is desirable for acceleration sensing, since the sensitivity is directly proportional to the recoil momentum.

The D2 transition between the $5S_{1/2}$ ground state and $5P_{3/2}$ excited state is shown in Figure 2.4. The key transitions used in this experiment are also indicated. The Zeeman sub-levels (with magnetic quantum numbers m_F ranging from $-F$ to F) are not shown explicitly. Their energies are shifted in a magnetic field B by an amount $g_F m_F B$, where g_F is the Landé g -factor. The values listed are taken from [32]. Further quantities, such as relative transition strengths and physical properties of Rubidium-87 are contained therein.

2.4.2 Driving Raman Transitions

Within the Rubidium-87 ground state, there are multiple pairs of states that can be coherently coupled using a Raman transition. A natural choice is for interferometry is

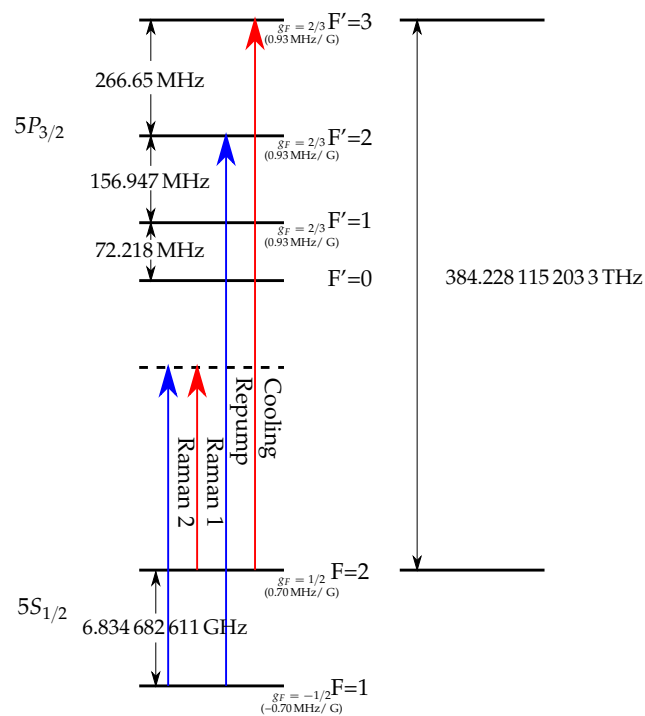


Figure 2.4: ^{87}Rb D2 transition hyperfine structure. The absolute energy difference of the $|F = 2\rangle$ and $|F' = 3\rangle$ levels is shown as an equivalent frequency. The energy of the other levels are shown relative to this. The approximate g -factors for each hyperfine level and Zeeman shifts are also indicated. The main transitions used in this experiment are indicated by red and blue arrows. The values are taken from [32].

to use the two $m_F = 0$ sub-levels¹. These are magnetically-insensitive; their transition frequency has at most a second-order Zeeman shift. Consequently, this transition is least affected by magnetic field variations from field gradients or environment noise.

The polarisation of the two light fields is crucial to ensuring that the $\Delta m_F = 0$ transition is driven. The $|1,0\rangle \rightarrow |2,0\rangle$ transition does not change the magnetic quantum number, i.e. the projection of angular momentum along the given quantisation axis. However, the total angular momentum quantum number increases by 1, which means that the Raman transition can be driven when the two electric fields are orthogonally linearly polarised ($\text{lin} \perp \text{lin}$) to each other and to the quantisation axis.

For circular polarisation, it can be shown that the two fields must have the same handedness. The electric field of a right-handed circularly polarised beam is $\mathbf{E} = E_0 (\mathcal{E}_- e^{-i\omega t} + \mathcal{E}_+ e^{i\omega t})$, where \mathcal{E}_- is the spherical tensor component that lowers the angular momentum of the light and \mathcal{E}_+ raises it. The product $r \equiv \mathbf{d} \cdot \mathbf{E}$ can be written as

$$r_j = E_0 (d_+^{(j)} \mathcal{E}_-^{(j)} e^{-i\omega_j t} + d_-^{(j)} \mathcal{E}_+^{(j)} e^{i\omega_j t}) \quad (2.31)$$

where $d_+^{(j)}$ and $d_-^{(j)}$ are the components of the dipole operator which increase and decrease m_F , respectively. The index j labels the $|j,0\rangle$ state. The product $r_1 r_2$ is expanded in the rotating wave approximation to give

$$r_1 r_2 = E_0^{(1)} E_0^{(2)} (d_+^{(1)} \mathcal{E}_-^{(1)} d_-^{(2)} \mathcal{E}_+^{(2)} e^{-i(\omega_1 - \omega_2)t} + d_-^{(1)} \mathcal{E}_+^{(1)} d_+^{(2)} \mathcal{E}_-^{(2)} e^{i(\omega_1 - \omega_2)t}) \quad (2.32)$$

where the first term corresponds to the component which drives $|1,0\rangle \rightarrow |2,0\rangle$ and the second to $|2,0\rangle \rightarrow |1,0\rangle$. The terms proportional to $(\omega_1 + \omega_2)$ have been neglected as they are off-resonant. A similar argument follows in the case of two left-handed circular polarised fields $\mathbf{E} = E_0 (\mathcal{E}_+ e^{-i\omega t} - \mathcal{E}_- e^{i\omega t})$. If one beam is left-handed and

¹In what follows, the states $|1\rangle$ and $|2\rangle$ will be used as alternative notation for $|F = 1, m_F = 0\rangle$ and $|F = 2, m_F = 0\rangle$ in instances where the explicit quantum numbers are not required

the other is right-handed, the near-resonant product of dipole operators results in components of the form $d_+^{(1)}d_+^{(2)}$. This changes the magnetic quantum number by ± 2 , which is suppressed for an $|F\rangle \rightarrow |F+1\rangle$ transition. This can be driven at resonance, but the transition amplitude rapidly decays as the detuning increases.

2.4.3 The Double Interferometer

The two frequencies for driving the Raman transition are sent into the experiment along the fast and slow axis of a Polarisation-Maintaining (PM) fibre. To produce the necessary counter-propagating beams, a Quarter-wave Plate (QWP) and mirror retro-reflect and invert the polarisation of each beam. This results in the beam configuration shown in Figure 2.5. With a magnetic field defining a z -axis parallel to the light's wavevector, the fields are all driving σ^\pm transitions. The co-propagating $\sigma^+ - \sigma^-$ combinations cannot drive the $\Delta m_F = 0$ $|F=1,0\rangle \rightarrow |F'=2,0\rangle$ transition, leaving the two counter-propagating $\sigma^+ - \sigma^+$ and $\sigma^- - \sigma^-$ combinations. These have effective wavevectors in opposite directions, which means that an atom resonant with both pairs is driven into a superposition of $|1, \mathbf{p}\rangle$, $|2, \mathbf{p} + \hbar\mathbf{k}\rangle$ and $|2, \mathbf{p} - \hbar\mathbf{k}\rangle$. The $\pi/2 - \pi - \pi/2$ pulse sequence results in a trajectory shown schematically in Figure 2.6. Some of the paths close to form two interferometers with oppositely signed phase shifts, making the interferometer insensitive to acceleration. Fortunately, these Raman transitions have Doppler shifts of opposite sign. Therefore, by appropriately detuning the light from resonance, an atom with a non-zero velocity will be shifted closer to resonance with one pair and further out from the other. Indeed, if the difference between their resonances $2|\mathbf{k}_{\text{eff}} \cdot \mathbf{v}|$ is larger than the transition linewidth, only one pair of beams drives the transition. The moving molasses method used to launch the atoms and lift this degeneracy is discussed later, in Section 5.2.3; a characterisation of the Raman transition spectrum in the experiment is presented in Section 7.4.1

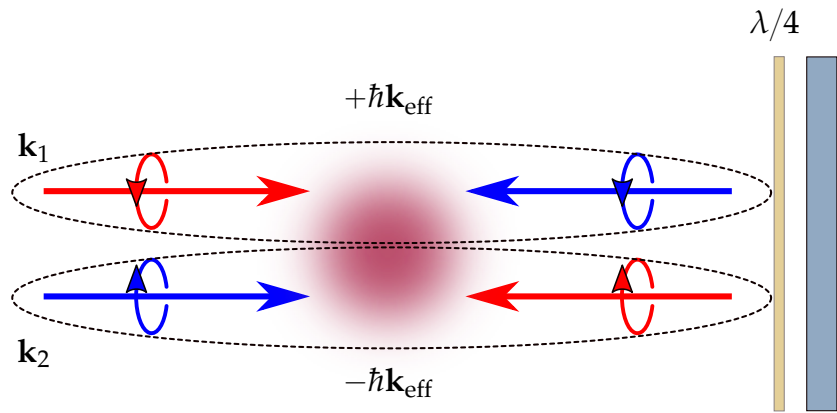


Figure 2.5: Raman beam configuration. The two incoming beams are orthogonally circularly polarised. The reflected beams pass through a QWP to invert their handedness. The selection rules of the Raman transition result in two pairs of beams that drive transitions with oppositely directed effective wavevectors.

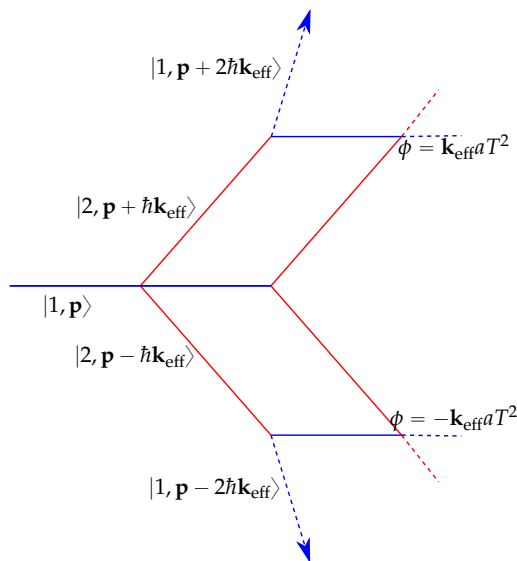


Figure 2.6: Interferometer paths with two oppositely directed Raman transitions. If the atom is resonant with both transitions, its momentum changes by $\pm\hbar\mathbf{k}_{\text{eff}}$. This results in two interferometers with oppositely signed phase differences. The dashed directed lines indicate trajectories which will not interfere, leading to a loss of coherence.

2.5 Conclusion

This chapter has presented a theoretical overview of matter-wave interferometry and motivated the use of a $\pi/2 - \pi - \pi/2$ sequence of laser pulses to measure the acceleration of an atom. Furthermore, it was shown how this can be implemented using a Raman transition between two ground states in ^{87}Rb . This induces a larger momentum recoil when compared to a microwave transition and thus, a greater sensitivity to accelerations. The effect of rotation on the interferometer phase has not been discussed. For further details on an atom interferometer gyroscope, the reader is referred to [33].

Chapter 3

MOTMaster

3.1 Chapter Overview

The aim of this chapter is to provide a description of the MOTMaster software, which was developed from a pre-existing version during my PhD. The design of MOTMaster assumes very little about the particular experiment it is being used for, so much of the discussion in this chapter will be kept general. This chapter begins with a motivating the need to extend MOTMaster by developing a graphical interface to simplify the creation of experimental sequences, as well as implementing new methods of controlling hardware. This is followed by a description of how input and output channels are controlled using MOTMaster in Section 3.3. The structure of a MOTMaster sequence, along with how it runs an experiment is then presented in Section 3.4. Finally, the specific hardware used in this experiment and an overview of each major step of the experiment is given in Section 3.5.

3.2 Motivation

In the initial stages of my PhD, I decided to use Cicero Word Generator [34] to control the hardware for the experiment. This is a graphical-based control system developed by Wolfgang Ketterle's group at MIT, which was designed for controlling atomic physics experiments using National Instruments hardware. Over time, as the experiment became more complex, it started to become apparent that Cicero was not suited to meet all of our requirements for control software. This was most evident in the control of the M-Squared Raman laser system. Cicero also takes an appreciable amount of time (around 300 ms) to re-calculate the experiment sequence between each shot. Since the design of Cicero was aimed at controlling experiments that take many seconds per cycle, this dead time between each cycle is not significant on those time scales. In contrast, each cycle of this experiment takes around 250 ms. This unnecessary dead time needed to be addressed if we hoped to improve the repetition rate.

After it became clear that a potentially large amount of work would be needed to improve Cicero, I decided that it was worth moving to a new control system. A collection of programs, named EDMSuite, has been developed by people in Centre for Cold Matter (CCM) to control a range of experiments within the group. One application, MOTMaster, was designed to control and acquire data from experiments investigating cold atoms trapped in a MOT. However, its method of structuring experimental sequences was inconvenient, as it lacked an intuitive graphical user interface. During the process of switching to using MOTMaster to control the experiment, I designed a graphical method of structuring sequences, which functioned identically on a device level to the original method of defining sequences. In addition to this, I included an interface to the M Squared laser system, so that it could be controlled using MOTMaster. A schematic of the structure of MOTMaster and how it interfaces with hardware

is shown in Figure 3.1. It is designed so that experiments can be controlled without requiring specific details about the hardware in use.

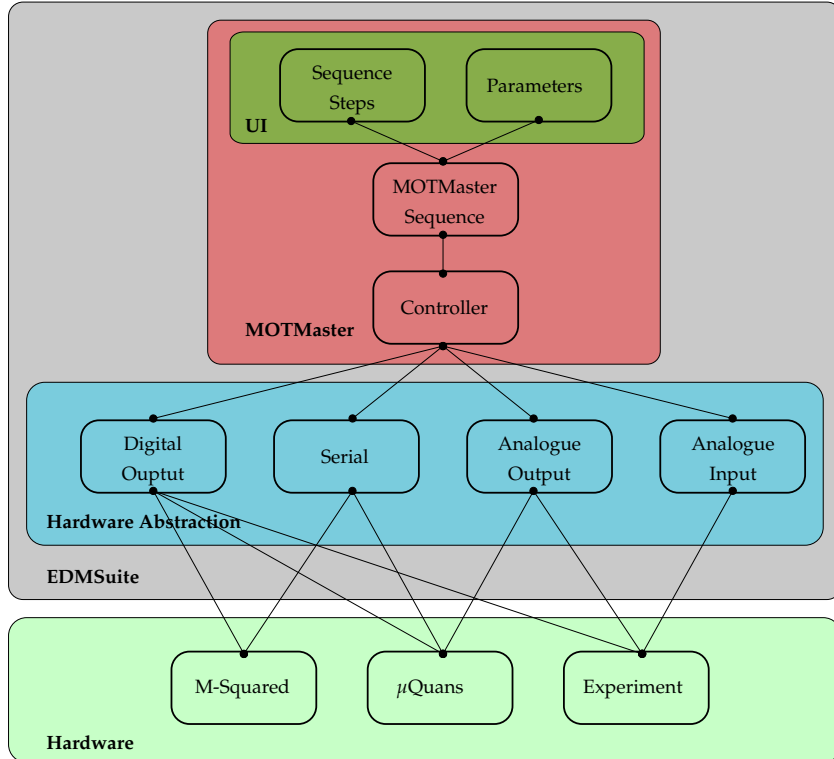


Figure 3.1: Schematic diagram of MOTMaster and the hardware it controls. A sequence is built using the user interface, which then uses separate modules to communicate to the hardware. In this way, an experiment can be controlled without requiring specific knowledge of the hardware.

3.3 Interfacing with Hardware

The majority of the experimental hardware is controlled using analogue and digital voltages that are generated by Data Acquisition (DAQ) cards manufactured by National Instruments. MOTMaster is compatible with cards that use either the NI-DAQmx or NI-HSDIO device drivers. These are used to configure the generation or acquisition of digital or analogue voltage waveforms. By design, they are capable of precisely timing and synchronising their I/O across multiple devices. Most compo-

nents in the experiment rely on this precise timing to function correctly. Other devices, where timing accuracy is less critical, are controlled by sending or receiving data using serial communication. Serial messages enable the execution of more complex commands than what is typical with analogue or digital voltages, but the communication speed of the serial channel limits the accuracy of the execution time.

The following section describes the low-level interface between MOTMaster and the experimental hardware. It begins by introducing the concept of hardware abstraction in Section 3.3.1. This is followed by a more detailed discussion of how each type of control is implemented. Section 3.3.2 describes how analogue and digital output waveforms are generated. Section 3.3.3 outlines serial communication, along with a method for triggering this communication during an experiment. Finally, this section concludes with a discussion on acquiring analogue input data, which is given in Section 3.3.4.

3.3.1 Hardware Abstraction

When designing software, it is often useful to structure a program in such a way that modules which make use of other components do not need to know about their specific implementation in order to use them. This approach means that a module can be modified without harming the compatibility with the rest of the programme. In the context of experimental hardware, this is equivalent to requiring that changing specific components, for example the Voltage-Controlled Oscillator (VCO) that generates the RF power for an AOM, will not stop the experiment from working. This is done using abstract representations of the hardware, in the form of input and output channels that are used to communicate to each device.

3.3.2 Voltage Pattern Generation

Analogue Outputs

All the analogue outputs controlled using MOTMaster are done using the NI-DAQmx software. Each output uses a Digital-to-Analogue Converter (DAC) to convert a floating-point number into an analogue voltage. To generate a sequence of voltages across multiple channels, the NI-DAQmx driver allocates a block of memory on the DAQ card for each output channel. This memory acts as a first-in first-out (FIFO) buffer for data streamed to it from a computer. The output of each channel is synchronised to a clock signal, so that every time a rising edge occurs on the clock, the voltage at each output transitions to the value corresponding to the next value in its corresponding buffer. Channels across multiple DAQ cards can be synchronised by sharing a clock signal, which can be done using the bus that connects cards in a PXI-e chassis. Additional cards can also be configured to trigger the start of their output at the moment they receive the first clock pulse, rather than waiting for a software trigger from the computer.

Digital Outputs

Digital outputs from NI-DAQmx cards are generated in much the same way as analogue voltages, except for the fact that they only take two values corresponding to either a low (0 V) or high (3.3/5 V) level. Additionally, DAQ cards which use the NI-HSDIO driver can be used. These cards can be sampled at much higher rates than NI-DAQmx ones. For instance, the NI-HSDIO PXI-6541 card can generate digital voltages at sample rates up to 50 MHz. Rather than writing the pattern as an array of values at each clock cycle, the sequence is segmented into smaller patterns during which the state of each channel is constant, as illustrated in Figure 3.2. NI-HSDIO

cards can be scripted to generate each of these patterns for the appropriate number of clock cycles.

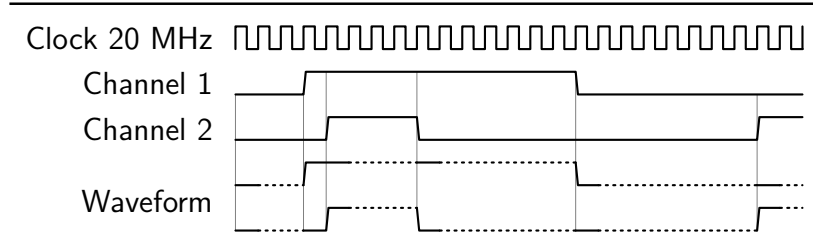


Figure 3.2: Scripted pattern generation for an NI-HSDIO digital output card. A pattern is split into segments which correspond to a duration for which all the channels output a constant value. The vertical lines indicate when at least one channel changes state, requiring a new segment. Each of these smaller waveforms are written to the on-board memory, along with a script that instructs the card to output each pattern for the required number of times to reconstruct the original sequence. The dotted lines illustrate the duration for which the segment is repeated. By reducing the amount of memory required to define the sequence, a faster clock frequency and hence timing resolution can be used to output digital control signals.

3.3.3 Timed Serial Communication

Serial communication is used to control devices which require more complex control than is possible using analogue or digital voltages. This increase in complexity comes at the cost of slower response times, because it takes longer to communicate an array of bytes than to change the voltage across an output terminal. For this reason, serial communication is mostly used to control devices where the execution time does not need to be precise. Using the NI-VISA driver, the output of serial data can only be timed using a software clock on a computer, which is more prone to jitter than a hardware clock. One way to improve the synchronisation between serial data and hardware timed outputs is to use extra hardware to trigger the transmission of serial data. If the trigger is timed using the same clock as other outputs and the transmission delay is accounted for, then serial data can be output more synchronously. In this experiment, the devices controlled using serial communication are triggered to execute

the commands using another hardware trigger. It is this trigger which enables the precise timing of the device, not the one which triggers the transmission of the serial data. The scheme for timing serial messages is shown in Figure 3.3. Serial messages are stored as strings on the computer and a counter channel is configured so that every time it detects a rising edge, the computer outputs the next message. This counter is connected to a digital output channel, so that it acts as a trigger for the serial data output. Using this method, multiple serial messages can be sent to one device during a sequence even for devices which have no means of storing commands.

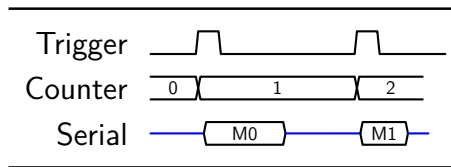


Figure 3.3: Timing diagram for serial communication. A counter channel is configured to count edges from a digital output channel. Every time it sees a rising edge, it triggers the output of the next message on each serial channel from the computer. Multiple messages can be communicated during a single sequence without the need for software timing.

3.3.4 Voltage Acquisition

Analogue input channels are configured in a similar way to analogue output channels. A block of memory is allocated on the DAQ card for each input channel. Once the card is triggered to start acquiring, an Analogue-to-Digital Converter (ADC) converts the voltage across the input into a digital value at every rising edge of the clock signal. Once the sequence has finished, or the buffer has been filled, the card streams this data to the computer.

3.4 MOTMaster Sequences

In addition to interfacing with control hardware, MOTMaster is used to define the structure of experimental sequences. In earlier versions of MOTMaster, sequences were defined using functions within a C# source file. To run an experiment, MOTMaster compiled this file to build the voltage patterns and wrote them to the hardware. Whilst this had little overhead in resources needed to build and run a sequence, modifying and debugging sequences was much more time consuming. Taking inspiration from Cicero, the user interface of MOTMaster was redesigned so that sequences could be expressed graphically. They are then built using the same functions as before, so that from the point of view of the hardware, the two methods of control are equivalent.

3.4.1 Sequence Structure

A MOTMaster sequence is composed of a list of sequence steps, which define the state of the control hardware over a discrete amount of time. Each step contains the following properties:

- Name: A descriptive name for the step.
- Duration: duration of the step, which must be an integer multiple of the timebase (e.g. 10 µs for a 100 kHz sample clock frequency).
- Serial Channel: A serial message encoded as a string of text.
- Digital Output Channel: High (3.3 V) or Low (0 V)
- Analogue Output Channel: Single value, step or ramp the output from a start to end value, or output an arithmetic function over time.
- Analogue Input Channel: An array of measured voltages stored.

where each channel is represented by its own property and associated with an identifying name.

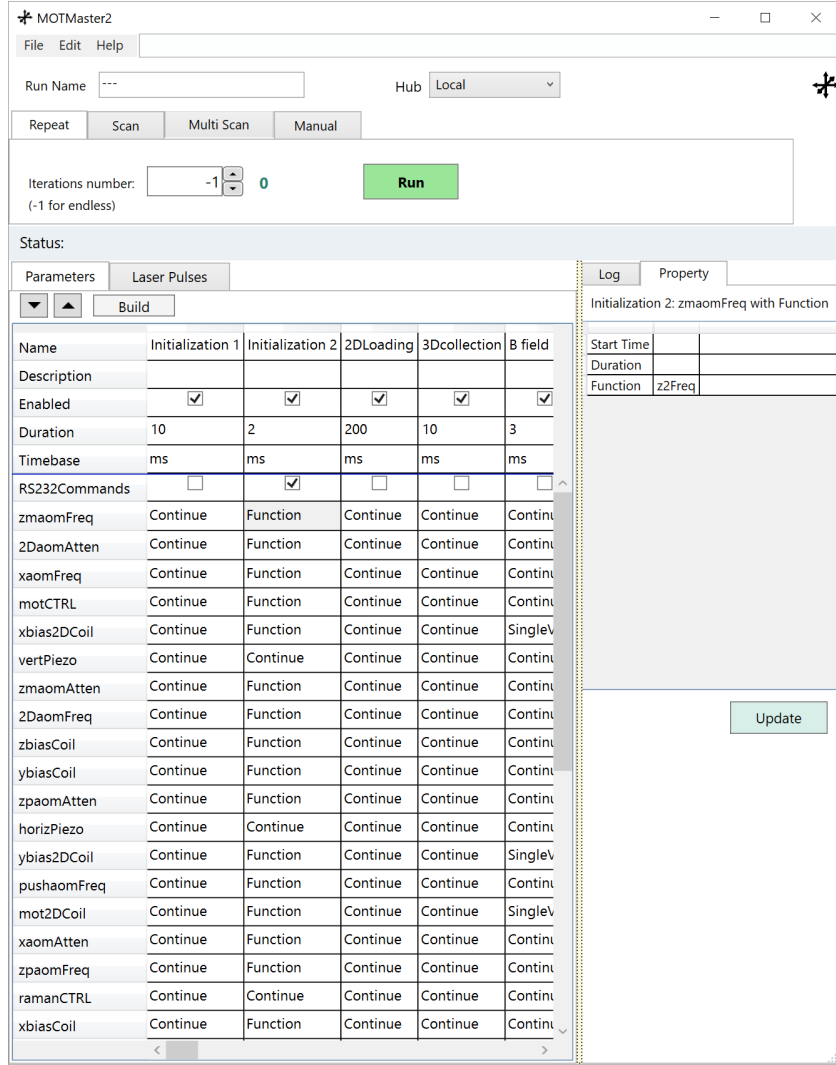


Figure 3.4: A sequence as represented in the MOTMaster user interface. Each step defines a duration and properties for each output channel. The sequence can either be run repeatedly, or configured to iterate through values of a chosen parameter.

A sequence step is useful to represent a single action, so that each stage of the experiment, for example the initial MOT loading phase, is composed of multiple steps. Numerical values, such as analogue voltages or times, can be represented by named parameters. The value of a parameter can be updated between each cycle of the experiment, so that MOTMaster can implement a scan by iterating a parameter through a

range of values. The sequence steps are also used to define when to acquire from the analogue inputs. A specific digital channel, named `acquisitionTrigger`, is reserved as a start trigger for the acquisition. This channel is also used to define the length of time over which to acquire data. Analogue data acquisition is triggered at the start of the step where this channel goes high and stops when it goes low.

3.4.2 Running a Sequence

MOTMaster is designed to run in two modes, referred to as repeat and scan. The distinction between these is that the repeat mode does not need to recreate a sequence between each cycle. Before MOTMaster starts controlling the experiment, the sequence is built once and the output hardware is configured to regenerate its patterns. This reduces the delay between each cycle, which is largely a result of the time needed to process acquired data and reconfigure the control hardware. In contrast, scan mode varies a parameter during each cycle, so additional time is required to rebuild the sequence and write to each DAQ card. Aside from this, these modes operate equivalently.

At the start of an experiment cycle, the hardware is initialised and timing properties, such as the trigger and sample clock for each DAQ card are set. An example of a sequence as represented in the user interface is shown in Figure 3.4. In this example, the output hardware is re-initialised to its default values before the sequence continues by switching on the 2D and 3D MOTs. Subsequent stages of the experiment are similarly defined, but are not shown in the figure. Each sequence step is represented as a column, where the rows correspond to the properties defined above. An exception to this are the analogue input channels, whose data are not shown in the user interface. Values for a selected output channel are set on the right-hand side. The default value `Continue` is used to indicate that the state of that channel does not change during that

step. The value Function is used to modify the state of that output channel. In this instance, during the step Initialization 2 the channel zmaomFreq is set to the value of a parameter named z2Freq. An optional start time and duration, relative to the start of that sequence step can be defined. In addition, the user interface is used to configure the two modes of operation and to define a descriptive name used in saving data from the experiment.

The sequence is converted into the analogue and digital voltage patterns for each DAQ card. The required buffer for the analogue input data is calculated based on the state of the acquisitionTrigger channel. If any serial commands are used, the timing properties of the counter channel are configured, similarly to the rest of the DAQ hardware. The sequence is started by sending a software trigger to one output card, which is configured to export its start trigger to the other cards. This ensures that start of the output of each card is synchronised.

After the sequence has finished, any acquired data from the analogue input channels is streamed to the computer. The data per channel are segmented into arrays that were acquired during each sequence step, before additional post-processing if required. Finally, the hardware is reset to its initial state, before starting the next experiment cycle.

3.5 Experiment Control Hardware

In the preceding sections, the discussion of MOTMaster has been presented without referring to specific hardware used in this experiment. Subsequent chapters will introduce components of the experiment that are controlled by a computer, but it is worth introducing the hardware used to implement this control. A diagram of the control hardware is shown in Figure 3.5. All of the DAQ cards are housed on a

PXIe-1073 chassis, so that timing signals such as start triggers and sample clocks can be shared on the PXI backplane. The analogue output signals are generated on a PXI-6723 card. This contains 32 analogue output channels and the output of each is generated using a 13 bit DAC. Over the maximum voltage range of $\pm 10\text{ V}$, this corresponds to an output quantisation of 2.44 mV , which did not limit the precision of any analogue control in the experiment. The analogue output pattern is sampled at a frequency of 100 kHz , which gives a minimum resolution of $10\text{ }\mu\text{s}$. Any jitter on this sample clock did not produce any noticeable effects during the experiment.

Two cards on the chassis are able to acquire data from analogue inputs. The first is a PXIe-6341, which has 16 input channels, each with a 16-bit ADC. In addition to this, a counter channel on this card was used to trigger the output of serial messages. During the preliminary stages of the experiment, this bit-depth was sufficiently large to prevent quantisation effects becoming significant. However the AI-Q-2010 MEMS accelerometer used in the experiment, discussed further in Section 6.4.2, has an equivalent voltage noise below this quantisation level. Therefore, a PXI-4462 card, which contains 4 24-bit analogue input channels, was added. This card is used to acquire data from devices where the higher voltage resolution is desirable — namely, the MEMS accelerometer and the photodiode used to detect the population of atoms in each state after interference.

Digital output signals are generated using a PXI-6541 card. Unlike the others, this card is controlled using the NI-HSDIO driver. With a maximum sampling frequency of 50 MHz , this card is capable of generating digital signals at a much higher rate than the PXIe-6341, which also contains digital output channels. However, the PXIe-6341 card only contains 8 digital channels that can be timed using a hardware clock, fewer than required to control the entire experiment.

Two components of the experiment are controlled during the experiment using serial communication. The first of these is an interface to the Direct Digital Synthesiser (DDS) on the μ Quans laser which control the frequency of the cooling and repump lasers and is controlled in real-time during the experiment. This communication protocol is described in further detail in Section 4.3.3. Finally, MOTMaster is configured to remotely connect to the M Squared laser, so that it can control all the parameters necessary to drive Raman transitions during the experiment. This is done by sending structured JSON messages that contain commands to implement this control. More detail on how this is used in the experiment is given in Section 7.2.2.

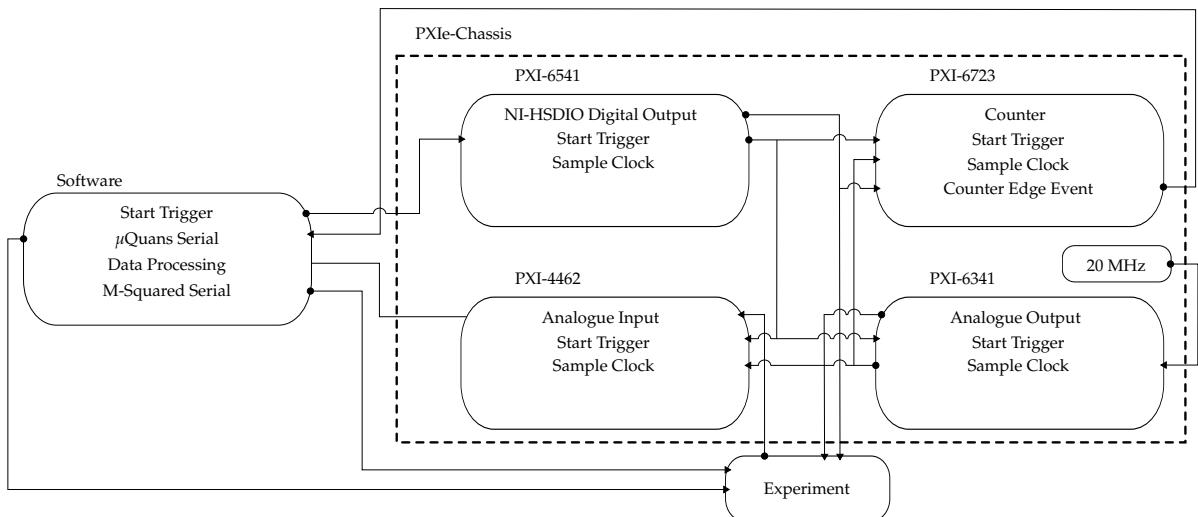


Figure 3.5: Schematic diagram of the control hardware. The PXIe chassis contains the DAQ cards which generate the analogue and digital waveforms used to control other devices. Signals are routed between the cards to synchronise their operation. Serial communication to the μ Quans laser (Section 4.3), the M-Squared laser (Section 7.2) and the CCD camera (Section 4.2.3) are used for their control.

3.6 Experimental Sequence Overview

The experiment can be broken down into the following stages:

- Loading: Atoms are loaded from the 2D MOT into the 3D MOT.

- Molasses: Atoms are released from the trap and cooled further in an optical molasses.
- State Preparation: A sequence of optical and microwave pulses are used to prepare atoms with a narrow velocity spread in the $|1, 0\rangle$ state.
- Interferometry: A $\pi/2 - \pi - \pi/2$ sequence of laser pulses drive Raman transitions between the atoms.
- Detection: Two laser pulses are used to measure the number of atoms in $|F = 2\rangle$ and the total number, respectively. From these measurements, the interferometer phase difference can be inferred.

Chapter 4

Cooling and Trapping in a MOT

4.1 Chapter Overview

This chapter describes the components of the experiment which are used to trap and cool atoms in a MOT. An outline of the hardware used to create both the 2D and 3D MOTs is presented in Section 4.2. Following this is a description of the μ Quans laser system, in Section 4.3, which generates the light used to cool and trap atoms. The hardware used to control the frequency and power of each MOT beam, as well as the required magnetic fields, is given in Section 4.4. Finally, this chapter concludes with a characterisation of the 3D MOT loading rate in Section 4.5

4.2 The Navigator Vacuum Chamber

The vacuum chamber, along with the components mounted to it, make up the majority of the hardware used in the preliminary trapping and cooling stages of the experiment. Figure 4.1 shows a diagram of the vacuum chamber and the main MOT components.

In this diagram, gravity is acting towards the bottom of the page. The chamber is made of 316L stainless steel, which has a low magnetic permeability to reduce stray magnetic fields on the atoms. It contains 16 DN40 ConFlat ports arranged on the edges of three octagons, one in each Cartesian coordinate plane. Six of these ports provide optical access for the 3D MOT. Another port connects the 2D MOT system to the main chamber. One port provides optical access for either a CCD camera or photodiode. Opposite this is a microwave horn for driving microwave transitions between the two ^{87}Rb hyperfine ground states. The remaining ports are not used for optical access since they do not have a direct line of sight to the atoms. Instead, these are used to mount a pressure gauge, gate valve, a Non-evaporative Getter (NEG) pump and electrical feedthroughs for the MOT coils.

Two oppositely-facing DN63 ports are used to mount the optics for driving Raman transitions¹. This is the axis along which the atom interferometer is sensitive to accelerations, subsequently referred to as the Raman axis.

The chamber is pumped down to a pressure of around 5×10^{-10} mbar using a NexTorr D100-5 pump. This is a composite system consisting of NEG and an ion pump. The NEG is a porous sintered zirconium (St 172) element, which reacts with chemicals such as hydrogen, water, nitrogen, oxygen and hydrocarbons. Most of these were removed during the initial baking and roughing pump stages. Under Ultra-high Vacuum (UHV) conditions, the largest contributor to the pressure is hydrogen which the NEG can pump at a speed of 100 l s^{-1} . Any species that are not absorbed by the NEG, in particular Rubidium, are pumped by the 5 l s^{-1} ion pump.

¹For more information about the Raman optical system, refer to Chapter 6

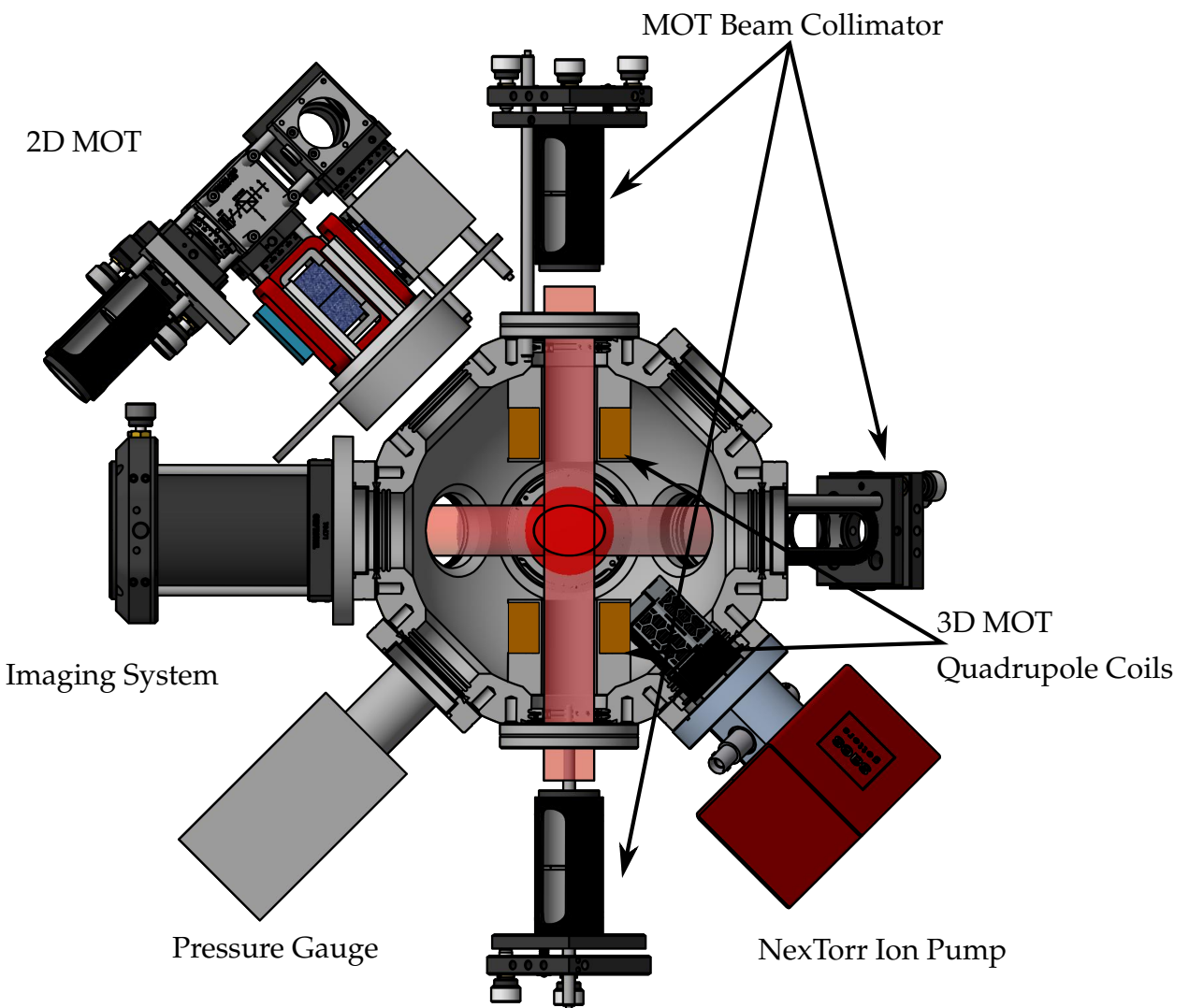


Figure 4.1: A diagram of the main components on the vacuum chamber used for the MOT systems. Rubidium atoms are dispensed and loaded into the 2D MOT before being pushed into the main chamber and collected in the 3D MOT. A set of 6 beam collimators provide the light to slow and cool atoms. A spherical quadrupole field traps atoms at the centre of the chamber. Not shown are additional bias coils along each MOT beam axis to null stray fields at the centre of the chamber. Gravity acts towards the bottom of the page, along the central axis of the 3D MOT quadrupole coils.

4.2.1 The 2D MOT system

At room temperature, a large fraction of atoms have velocities greater than typical MOT capture velocities, so a very high partial pressure of Rubidium is needed to achieve a fast loading rate from a background vapour. We do not want so high a pressure in the main chamber because collisions with background gas reduce the fringe visibility. Instead, we keep the high pressure region in a side chamber where a large number of atoms are loaded into a 2D MOT [35]. This allows us to collect many atoms, while also retaining a low pressure inside the main chamber.

A diagram of the light and magnetic fields required to produce a 2D MOT is presented in Figure 4.2. It is similar to the 3D MOT, with the main exception being that only 4 beams are used to cool the atoms along 2 orthogonal axes. It is designed to produce a large flux of cold atoms which can be subsequently loaded into a 3D MOT [36,37]. The cooling beams are collimated to a large waist size and the magnetic field coils produce a cylindrical quadrupole field with a line of zero magnetic field along the axis of symmetry. Along this axis, the atoms are free to move, resulting in an atomic beam. This beam is collimated using a larger radial field gradient than is typically found in 3D MOT systems. This increases the radial confinement of atoms.

A pinhole is placed at the exit of the cell to prevent atoms with a high radial velocity from exiting. This pinhole also greatly reduces the conductance between the 2D MOT cell and the main chamber, which means that a high rubidium partial pressure can be maintained in the 2D MOT cell, without greatly increasing the pressure in the main chamber. The pinhole is drilled into a silicon plate, which partially reflects the beam that propagates along the central axis. This creates an unbalanced molasses that cools atoms along the axial direction. The scattering rate from each beam is not equal, so the net force on the atoms pushes them through the pinhole. By slowing a larger

proportion of atoms to within the capture velocity of the 3D MOT, this configuration, referred to as a 2D+ MOT, loads a 3D MOT faster than the 4-beam counterpart.

Figure 4.3 shows a schematic of the optical components used to generate the light

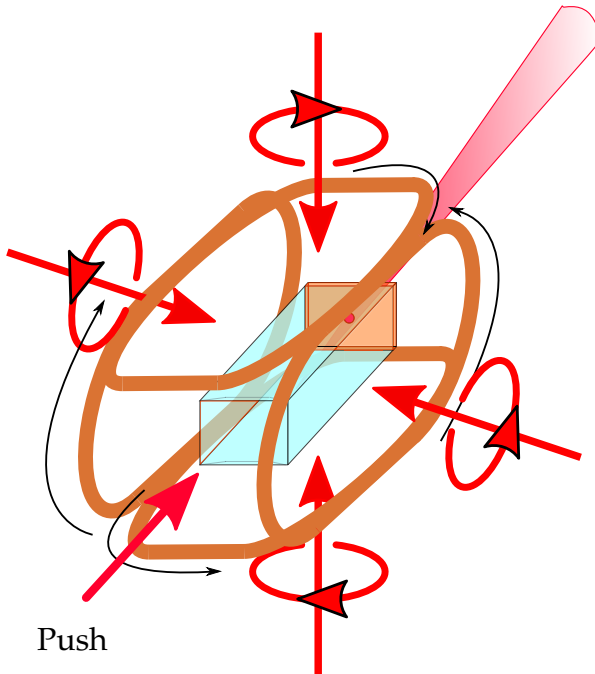


Figure 4.2: Schematic diagram for the 2D MOT. ^{87}Rb atoms are trapped and cooled along the 2 axes orthogonal to the long axis of the source cell. The black arrows indicate the direction of the current through each coil. The handedness of each circularly polarised beam is indicated and are such that each beam drives σ^- transitions for an atom moving in the opposite direction. A linearly polarised push beam propagates along the longitudinal axis and is partially reflected by the silicon wafer at the opposite end. This provides a small amount of axial cooling and the imbalance of radiation pressure pushes atoms out of the cell. The pinhole at the other end prevents atoms with a high transverse velocity from leaving the cell.

for the 2D MOT. The cooling light enters from a single fibre, which is collimated to a beam waist of 9.5 mm using two aspheric lenses. A Half-wave Plate (HWP) divides the linearly polarised light into two beams of equal power, one for each cooling axis. Each beam passes through a beam-splitter and a prism mirror, to increase the volume covered by the 2D MOT beams. A QWP circularly polarises the beam before it enters the ar-coated glass cell. On the opposite side of the cell, a 25 mm \times 35 mm mirror

retro-reflects the beam. A QWP is bonded onto the surface of the mirror and is aligned so that the reflected beam has the same helicity as the incoming.

The push beam enters from a second fibre input. A fixed focus collimator collimates the beam to a waist of 1.5 mm. This is mounted onto a 25 mm kinematic mount to align the push beam to the 0.7 mm pinhole at the other end of the cell. The push beam is linearly polarised by a Polarising beam-splitter (PBS) to reduce the effect of polarisation drift on the axial cooling of the 2D MOT.

The cell, manufactured by ColdQuanta, has dimensions of 30 mm × 30 mm × 44 mm and is specifically designed for creating a 2D+ MOT. It contains two rubidium dispensers composed of rubidium chromate (RbCrO_4) and a reducing agent. These were activated by passing a large current through them to remove a thin oxidation layer. To produce rubidium, a current of around 2.8 A is passed through the dispenser to trigger an electro-chemical reduction reaction, so that pure rubidium sublimates.

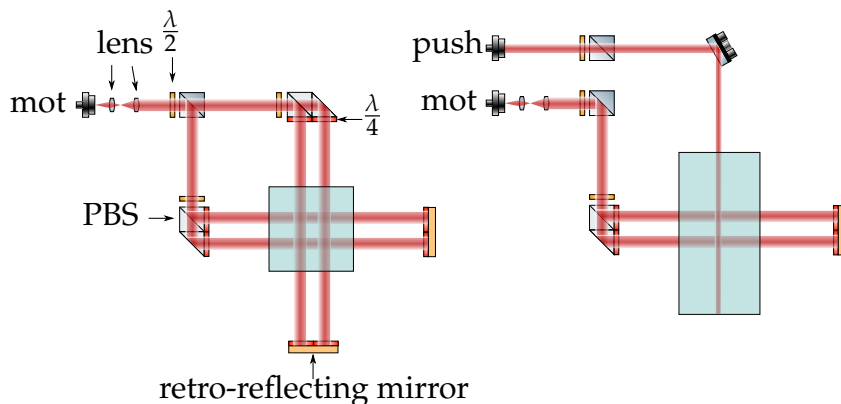


Figure 4.3: Optical components for the 2D MOT. The left-hand diagram indicates the components in the radial plane and the right-hand shows those in the axial plane. The light for the MOT is split into two equal portions using a HWP and PBS. Along each axis, the beam passes through a PBS and a prism mirror to increase its spatial extent. The beam is circularly polarised before entering the cell and retro-reflected by a QWP bonded on top of a mirror. The push beam is collimated from another fibre input and linearly polarised before entering the cell along the longitudinal axis.

The cylindrical quadrupole field is generated by a set of coils that are manufactured by ColdQuanta. They are mounted so that the axis of zero magnetic field coincides with the central longitudinal axis of the source cell. These produce a radial field gradient per unit current of $20 \text{ G cm}^{-1} \text{ A}^{-1}$. During the experiment, a current of 0.97 A produces a radial field gradient of 19.4 G cm^{-1} . Figure 4.4a shows the magnitude of the calculated magnetic field strength in the radial plane where the axial co-ordinate is $y = 0$. The equally-spaced contours of constant magnetic field are indicative of a quadrupole field. Figure 4.4b shows the field gradient $\partial B / \partial x$ where $y = 0$ and $z = 0$. This is uniform across the central 10 mm, where the MOT forms. Figure 4.4c shows the field strength in the axial plane where $z = 0$. Along the axial direction, the field is zero and increases in magnitude away from the central axis. At around 3 mm away, the field strength is around 10 G, which corresponds to a Zeeman shift of 14 MHz. The MOT light is red-detuned from resonance by 15 MHz, and will therefore be shifted to the blue side of the transition beyond this. Outside of this trapping volume, atoms will not be cooled, so it is not necessary to have MOT beams with a waist larger than this.

The equilibrium position where the MOT forms is adjusted using Helmholtz coil pairs along each MOT axis. These coils produce a field per unit current of 1 G A^{-1} .

4.2.2 The 3D MOT system

The main chamber contains the apparatus that is used to make a 3D MOT [38]. Each MOT beam originates from a PM fibre and is collimated using a lens with a nominal focal length of 75 mm to a waist size of 7.5 mm. At the output of each collimator is a QWP, with its slow axis oriented at a 45° angle to either the fast or slow axis of the fibre, to produce either left- or right-handed circularly polarised light. The MOT beams along the axial direction of the quadrupole field (i.e. the \vec{z} direction) are orthogonally polarised to the others along the \vec{x} and \vec{y} directions. The MOT beams are aligned so

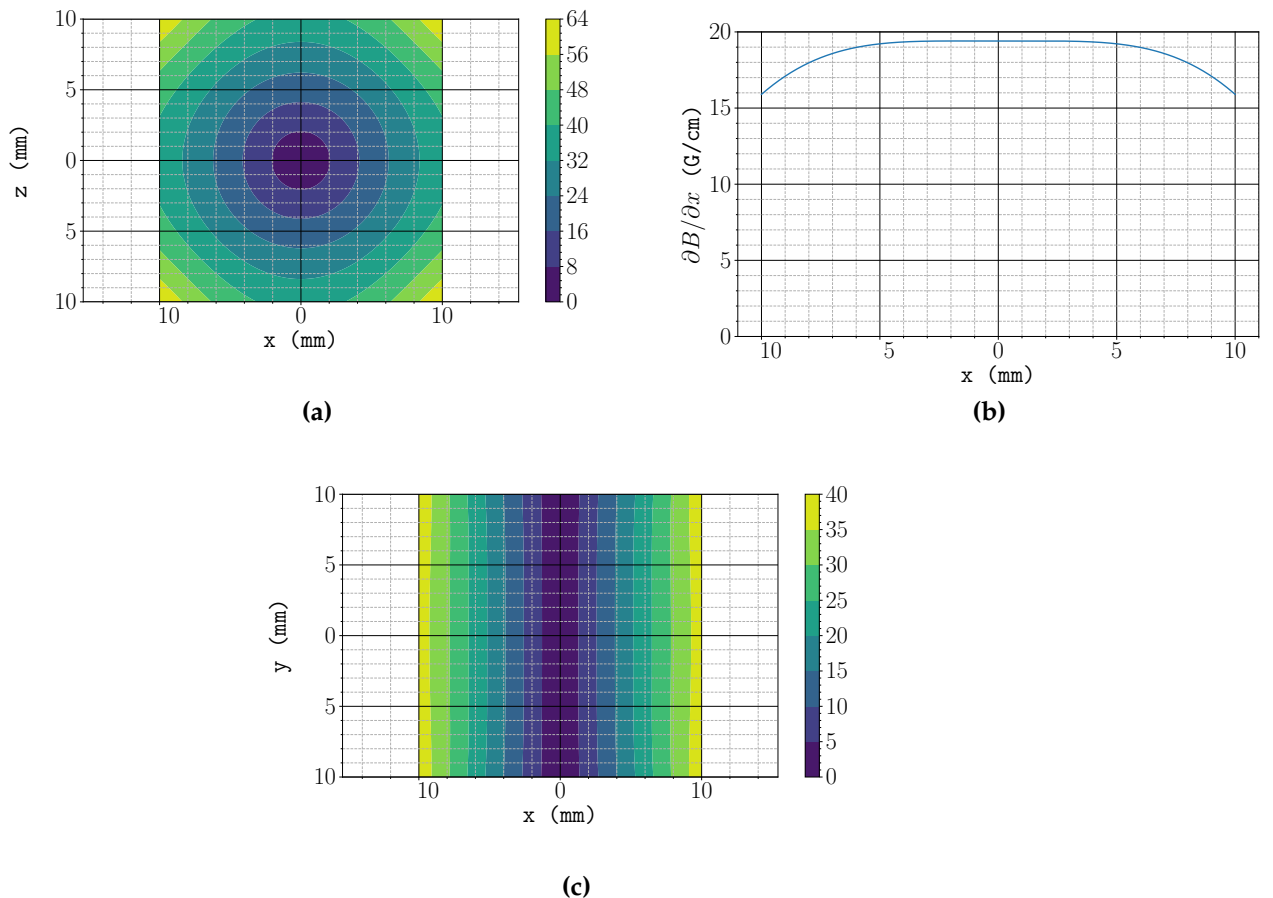


Figure 4.4: Calculated field and field gradients for the 2D MOT quadrupole coils. In this coordinate system, the 2D MOT cools and traps atoms in the \vec{x} and \vec{z} directions. The simulation was performed using a nominal current of 1 A, which corresponds to a current density in each coil of 7.78 A mm^{-2} . The magnitude of the magnetic field (in units of G) and its direction in the axial and radial planes of symmetry are shown in (a) and (c), respectively. (b) shows the field gradient components $\partial_x B_x$ along the x axis.

that their intensities at the centre of the chamber are equal, so that the MOT forms where the magnetic field is zero.

Spherical quadrupole magnetic field

The magnetic field for the 3D MOT is created by a pair of coils in an anti-Helmholtz configuration. Each coil is wound using rectangular wire coated in a 35 µm thick layer of Pyre-M.L, a UHV-compatible polyamide which provides a layer of insulation between each loop. The wire has a cross-section of dimensions 1.1 mm × 1.1 mm, including the insulation. The coils have 20 layers in the axial direction and 12 radially. The inner diameter of the coil is 25.4 mm, to allow for optical access of the \vec{z} -axis MOT beams, and the maximum diameter is 59.2 mm – small enough that the coil could be inserted into the chamber through the DN63 CF ports. The coils are mounted to the chamber using groove grabbers which clamp into grooves inside the wall of the DN40 ports. The coil formers increase the surface area in contact with the chamber, increasing the rate of heat dissipation from the coils.

Figure 4.5a shows the temperature rise of the coils after they are turned on, both at atmospheric pressure and after evacuating the chamber. At a low pressure (here around 1×10^{-2} mbar), the temperature of the coils inside the chamber does not exceed 40 °C. This warms the chamber up by a few degrees, as shown in Figure 4.5b. Once mounted, the distance between the innermost loops is 70 mm. The red and blue circles in Figure 4.6a show the magnetic field, measured using a Hall probe, along the axis of symmetry for each of the coils with a current of 2.53 A. Figure 4.6b shows the axial field measured when the coils are operating together. This shows good agreement with the field calculated from the Biot-Savart law.

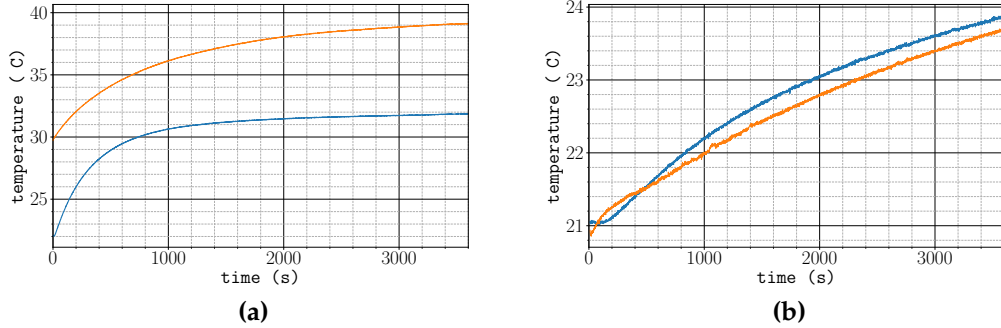


Figure 4.5: Temperature rise due to the MOT coils over 1 hour of operation. The blue curves were measured when the coils were at atmosphere and the orange were measured under a rough vacuum around 1×10^{-2} mbar. For the orange curve, the coils were switched on before $t = 0$. (a) shows the temperature of the coils and (b) is the temperature of the exterior of the chamber.

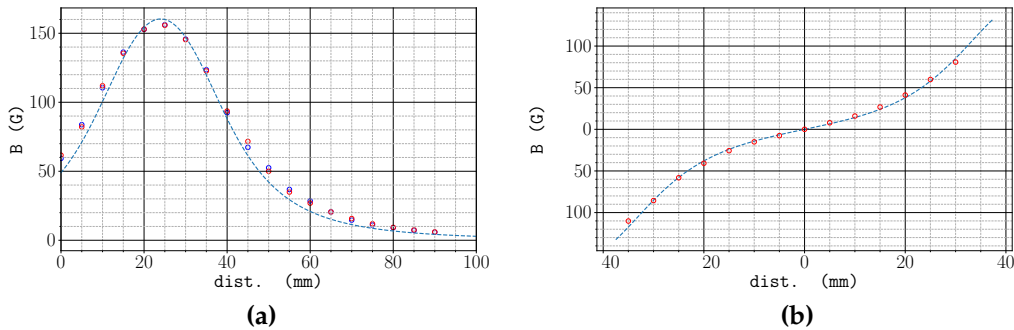


Figure 4.6: Measured magnetic field for the 3D MOT coils. (a) red and blue circles show the axial magnetic field component of both coils as measured using a Hall probe, where the origin corresponds to the outermost coil loop. (b) red circles show the field close to the centre when the coils are operating together. In this case, the origin corresponds to the mid-point between the two coils, which is the centre of the trap. The dashed lines indicate the axial field as calculated from the Biot-Savart law. Close to the centre of the coils, the magnetic field is approximately linear, indicating a constant magnetic field gradient.

| Axis | a (mm) | r_i (mm) | r_o (mm) |
|-----------|----------|------------|------------|
| \vec{x} | 88 | 105 | 115 |
| \vec{y} | 132 | 178 | 188 |
| \vec{z} | 116 | 123 | 133 |

Table 4.1: Table of parameters for each 3D MOT bias coil. a denotes the axial separation between each coil, measured from their centres. r_i and r_o are the inner and outer radii, respectively.

Bias Coils

Three orthogonally arranged pairs of coils are used during the experiment to provide a homogeneous magnetic field close to the centre of the chamber. In the initial loading and molasses stages, these are used to zero the magnetic field at the centre of the chamber. This is required for effective sub-Doppler cooling. In subsequent stages, these coils provide a bias field along the appropriate axes during state preparation, interferometry and state detection. Each coil was wound using 1 mm thick wire and consisted of 5 turns in the axial direction and 10 turns radially. For a pair of coils in Helmholtz configuration, the magnetic field gradient at the centre is minimised when the axial separation a is equal to the coil radius r , but the geometry of the vacuum chamber meant that it was not possible to satisfy this condition. The radii and axial separations of each coil pair are presented in Table 4.1.

4.2.3 CCD Imaging

During the experiment, atoms are imaged using a CCD camera to spatially resolve the cloud. This was done to measure the temperature using a ballistic expansion method and the trajectory of the cloud (see Section 5.2.4). Figure 4.7 shows a diagram of the apparatus used for imaging. A pair of 125 mm and 50 mm focal length lenses

are used to image the cloud onto a Pike F505-B CCD camera. The camera has a maximum resolution of 2452×2054 pixels. A ruler placed in the object plane gave a calibration factor of $7.062(48)$ pixel/mm. To reduce the level of background light on the CCD, a bandpass filter is placed in front of the sensor. This transmits the Rubidium fluorescence at 780 nm with an efficiency of 60%.

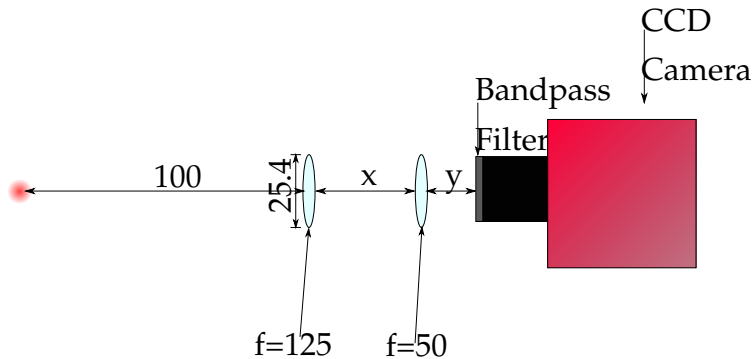


Figure 4.7: Optical setup for CCD imaging. Two lenses are used to magnify the image of the atom cloud on the CCD. A bandpass filter is placed in front of the sensor to block out background light at wavelengths other than 780 nm. All lengths are given in millimetres.

Incident Optical Power Calibration

Measuring the incident optical power emitted during resonance fluorescence is useful for estimating the number of atoms N_a . However, typical number densities in a MOT mean that the cloud is optically thick and we see mainly the atoms close to the surface. Consequently, the fluorescence can lead to an under-estimate of the atom number. More accurate techniques such as absorption imaging can be used, but for the purposes of this experiment, it was sufficient to use fluorescence imaging as a rough estimate of the number of atoms in the MOT. In subsequent stages of the experiment, a sensitive photodiode with a high bandwidth was used to detect the atoms in each hyperfine ground state. Details on this setup can be found in Section 7.3.2.

Neglecting absorption, the power incident on the CCD, let us call that P_{ccd} , can be related to the scattering rate per atom R_{sc} as follows

$$P_{\text{ccd}} = \frac{\Omega}{4\pi} t R_{\text{sc}} \hbar \omega N_a \quad (4.1)$$

where $\Omega/4\pi = 1.8 \times 10^{-3}$ is the fractional solid angle subtended by the imaging optics, t is the transmission of the bandpass filter and $\hbar \omega = 1.6 \text{ eV}$ is the fluorescence photon energy. For a two-level system, the scattering rate R_{sc} is

$$R_{\text{sc}} = \frac{\Gamma}{2} \frac{s}{1 + s + \left(\frac{2\delta}{\Gamma}\right)^2} \quad (4.2)$$

where Γ is the spontaneous decay rate of the upper level, δ is the angular frequency detuning and $s = I/I_{\text{sat}}$ is the saturation parameter. This incident power is then related to the integrated number of pixel counts C_{int} by

$$C_{\text{int}} = \alpha \tau_{\text{exp}} \eta P_{\text{ccd}} \quad (4.3)$$

where τ_{exp} is the exposure time, $\eta = 0.14$ is the quantum efficiency of the CCD and α is a scaling factor that relates the incident light energy to pixel counts. By varying the exposure time used to image a collimated beam with a total power of $0.17 \mu\text{W}$, the total number of counts recorded by the camera as a function of exposure time is plotted in Figure 4.8. Each data point is obtained by subtracting a background measurement for the same exposure time. Below $50 \mu\text{s}$, the signal-to-noise ratio is too low to detect the incident light as indicated by the fact that zero counts are observed for a non-zero duration. This gives a count scaling factor of $\alpha = 2.2 \times 10^5 \text{ counts } \mu\text{s}^{-1} \mu\text{W}^{-1}$. With this calibration, the number of atoms in the MOT can be estimated. This is described further in Section 4.5.1.

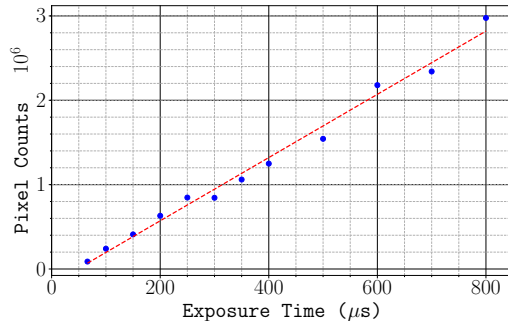


Figure 4.8: Integrated pixel counts as a function of CCD exposure time for an incident optical power of $0.17 \mu\text{W}$ after subtracting a background measurement. The dashed line indicates a linear regression which gives a scaling factor of $\alpha = 2.2 \times 10^5 \text{ counts } \mu\text{s}^{-1} \mu\text{W}^{-1}$. Zero counts are detected for a non-zero duration because the incident light level is equal to the background light level for exposure times below $50 \mu\text{s}$.

4.3 Generating MOT light

All the MOT light in this experiment was generated by the μ Quans laser [39]. μ Quans is a French laser company that is a spin-off from the Institut d'Optique and Observatoire de Paris. A schematic of this laser system is shown in Figure 4.9. The light is fibre-coupled to minimise the number of free-space optical components. This makes the system more stable in the presence of vibrations and temperature variations. The μ Quans laser is comprised of four 1560 nm External-Cavity Diode Lasers (ECDLs) which are frequency-doubled to produce light at 780 nm [40]. The first acts as a master laser which is locked to the $|F = 3\rangle \rightarrow |F' = 3, 4\rangle$ crossover point in Rubidium-85 (^{85}Rb) to serve as an absolute frequency reference. The other three slave lasers are used for output. The first one provides light for cooling ^{87}Rb using the $|F = 2\rangle \rightarrow |F' = 3\rangle$ transition. Light for the $|F = 1\rangle \rightarrow |F' = 2\rangle$ repump transition is created by phase modulating this laser using an Electro-optic Modulator (EOM). The other two make up a pair of lasers for driving Raman transitions. One laser is frequency-offset locked to the master and the other is phase-locked to the first. This Raman laser was not used in this experiment, so will not be discussed in further detail. The power in each of

these slave lasers is amplified using an Erbium-Doped Fibre Amplifier (EDFA). The frequency is doubled to around 780 nm using a Periodically-Poled Lithium Niobate (PPLN). The output power is controlled using an AOM.

4.3.1 Absolute Frequency Reference

The master laser provides an absolute frequency to which the slave lasers are offset-locked. The reference frequency is created using saturated absorption spectroscopy inside a Rubidium vapour cell. The sub-Doppler features in this spectrum are insensitive to temperature changes, and have linewidths close to the natural linewidth of Rubidium ($\Gamma \sim 2\pi \times 6$ MHz). Figure 4.10 shows the saturated absorption spectrum using the μ Quans master laser. The frequency is varied by finely adjusting the temperature of the master ECDL. The master laser is set to lock to the crossover resonance between the $F = 3 \rightarrow F' = 3$ and $F = 3 \rightarrow F' = 4$ transitions in ^{85}Rb (indicated as **(b)**), which is the strongest feature in the spectrum. This crossover is around 1.1 GHz above the cooling transition in ^{87}Rb (indicated as **(a)**). The frequency of the laser is dithered by modulating the current to the ECDL [42]. Phase-sensitive detection using a lock-in amplifier then produces the derivative signal shown in Figure 4.11. Close to the lock point that provides an error signal that is proportional to the frequency difference from the lock point. The servo that controls the master laser frequency also contains an integrator to compensate for long-term drifts arising from temperature variations.

4.3.2 Cooling and Repump Light

The first of the slave lasers provides light to address the cooling transition. This is frequency-offset locked to the master by comparing their beat frequency to a reference from a DDS (labelled as f_0 in Figure 4.9). The reference is multiplied by a factor of

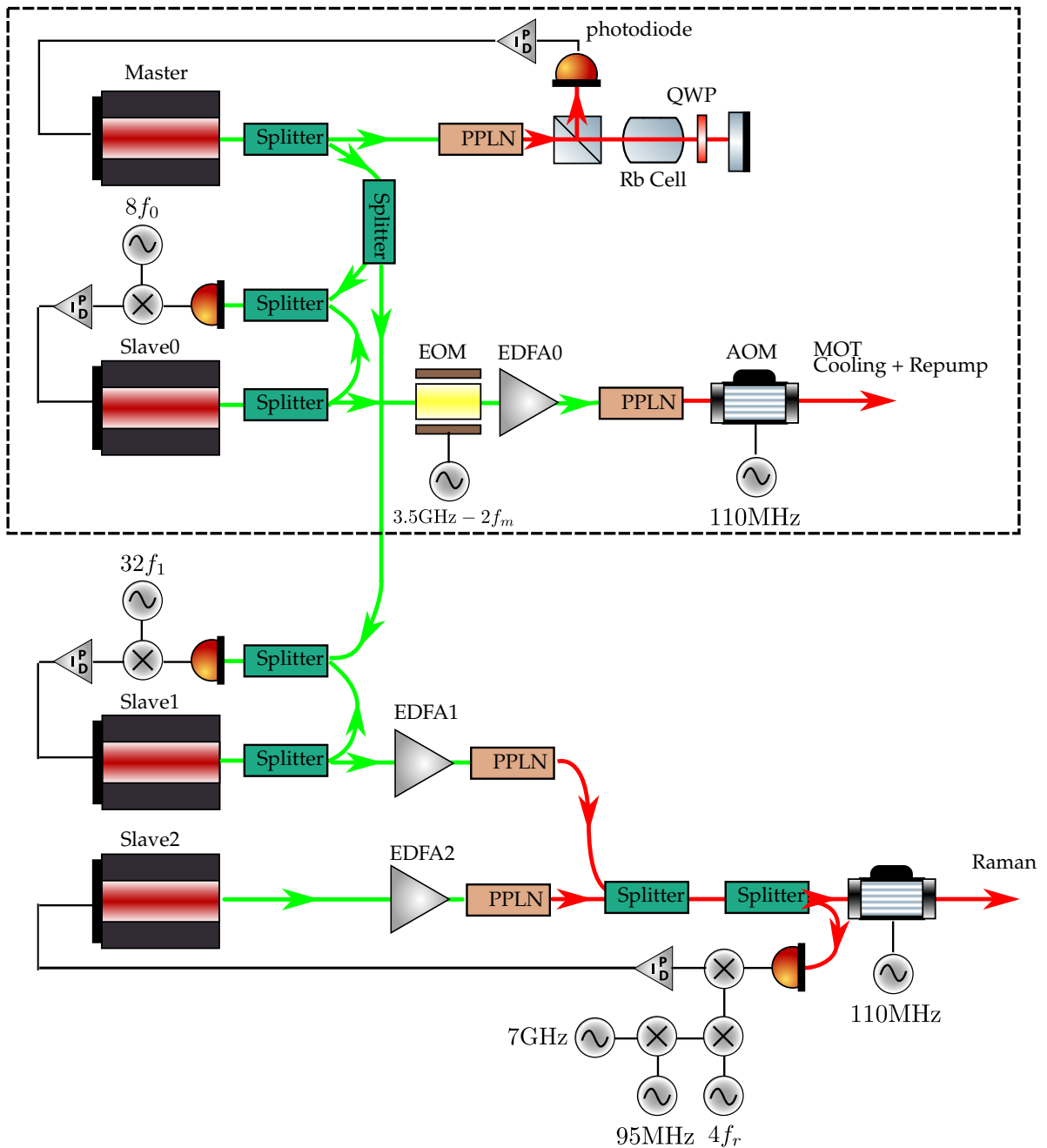


Figure 4.9: Schematic of the μ Quans laser system. Each output laser is derived from a 1560 nm ECDL (shown in green) which is amplified using an EDFA and then frequency-doubled to 780 nm using a PPLN crystal. A master laser is locked to the 3,4 crossover in ^{85}Rb and the output lasers are offset-locked to their corresponding frequencies. The dashed region indicates the components used for generating light for the MOTs, which was the part used for this experiment.

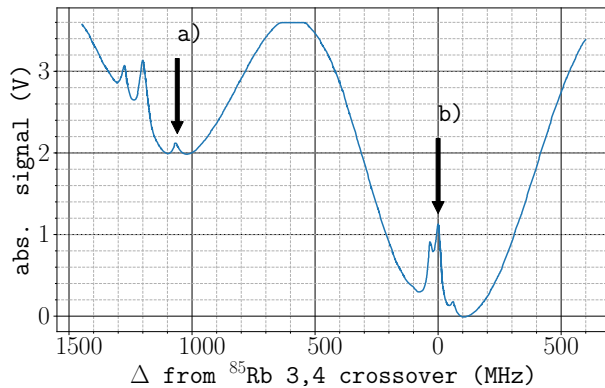


Figure 4.10: Saturated absorption spectroscopy using the Rubidium vapour cell in the μ Quans laser. The absorption features indicated are *a*: the $F = 2 \rightarrow F' = 3$ transition in ^{87}Rb and *b*: the crossover resonance between the $F = 3 \rightarrow F' = 3$ and $F = 3 \rightarrow F' = 4$ transitions in ^{85}Rb which is used to lock the frequency of the master laser.

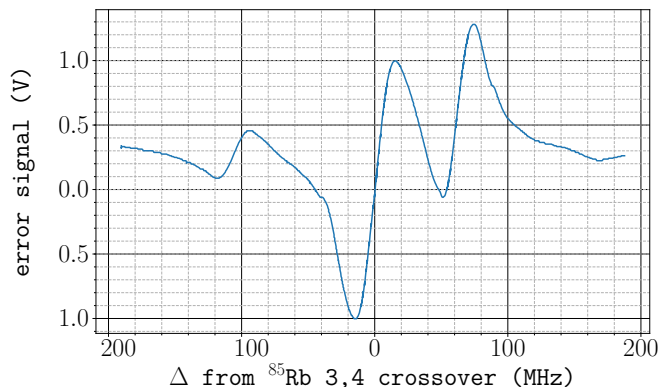


Figure 4.11: Error signal obtained by modulating the laser current. Close to the lock point, the signal is approximately linear. This signal is used in a feed-back loop to correct for frequency changes of the master laser.

8 before it is mixed with the beat frequency of the 1560 nm light. After frequency doubling and taking into account the frequency shift of the output AOM and those used to control each MOT beam (see Section 4.4), a DDS frequency of 88.82 MHz offsets the frequency of the slave laser from the master laser's frequency so that it is resonant with the $|F = 2\rangle \rightarrow |F' = 3\rangle$ cooling transition. Similarly, a DDS frequency of 87.89 MHz red-detunes the slave laser from this transition by 15 MHz. A plot of the error signal used to lock this offset frequency is shown in Figure 4.12. The zero-crossing occurs when the frequency difference of the two lasers is equal to $8f_0$.

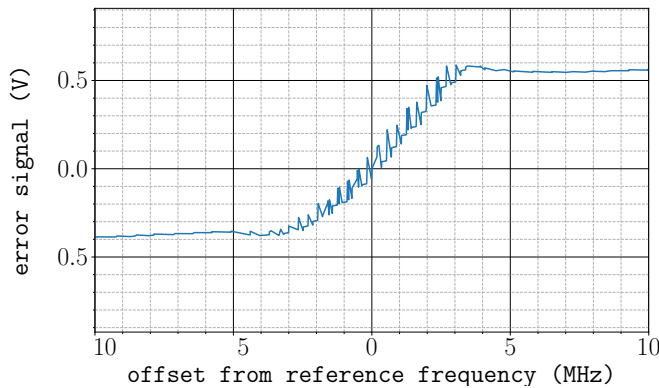


Figure 4.12: Error signal for the μ Quans cooling laser, plotted as a difference from the reference frequency. The beat frequency between the master and slave lasers is compared to a reference frequency generated by a DDS (see text). Between ± 3 MHz, the error signal is proportional to the frequency difference and is used by a servo-loop to keep the difference close to zero.

An EOM modulates the phase of the cooling laser to produce light for the $|F = 1\rangle \rightarrow |F' = 2\rangle$ repump transition. This modulation creates frequency sidebands separated by integer multiples of the modulation frequency. If the amplitude of the modulation is small, only the first positive and negative sidebands are present. When the carrier is set to drive the cooling transition, the modulation frequency is set so that the first positive sideband drives the repump transition, which is 6.6 GHz higher in frequency. A separate DDS provides the reference for the modulation frequency (labelled as f_m in Figure 4.9), so that the frequency of the cooling and repump light

can be independently ramped during the experiment (see Section 4.3.3). The DDS frequency is amplified, doubled and subtracted from a 3.5 GHz reference signal to give the modulation frequency for the EOM. A DDS frequency of $f_m = 104.25$ MHz produces a positive sideband to drive the $|F = 1\rangle \rightarrow |F' = 2\rangle$ transition when the carrier is -15 MHz below the $|F = 2\rangle \rightarrow |F' = 3\rangle$ transition. The modulation power is externally controlled using a Voltage-Controlled Attenuator (VCA) to control the ratio of repump power to cooling power. An RF switch turns the repump on and off by blocking the reference frequency.

The total output power is controlled using an AOM that has a fixed modulation frequency of 110 MHz. Figure 4.13 shows the combined power of the cooling light for the 3D MOT as a function of the control voltage to the AOM RF power. The hardware used to divide the light from the laser to the separate beams is described in Section 4.4.1.

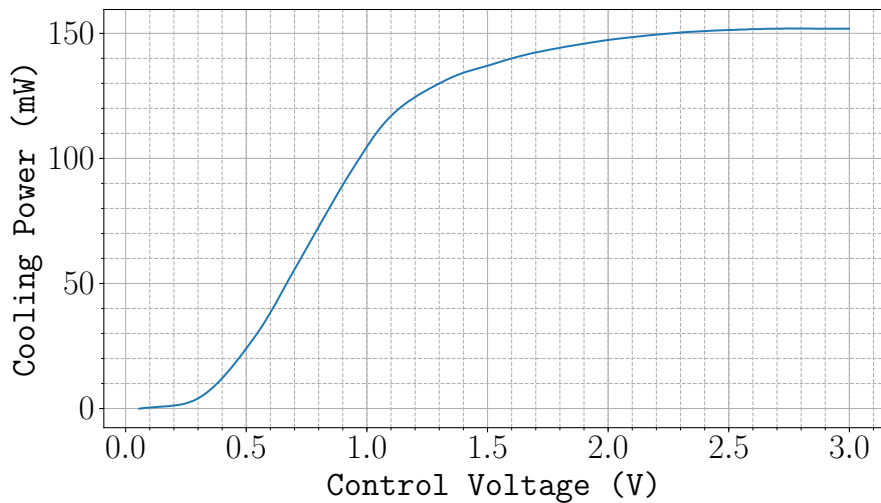


Figure 4.13: Combined 3D MOT cooling power as a function of control voltage for the RF power that drives the μ Quans output AOM.

4.3.3 Real-Time Control

During the experiment, it is necessary to vary the frequency and power of both the cooling and repump light. Analogue and digital signals control the RF sources for the output AOM and EOM. A DDS generates each RF frequency, so that they can be updated in real-time. These are also programmed to ramp the output frequency for a specified duration and ramp rate. This is done by sending serial messages to an application which interprets the message and synchronously communicates the command to the DDS using Serial Programming Interface (SPI). A glossary of the messages and their function is given in Appendix ???. The command is stored in memory on-board the DDS and is triggered to start using a digital pulse. This means that the time at which the frequency of the light changes is synchronised with the rest of the experiment.

4.4 Controlling the MOTs

Effective trapping and cooling of Rubidium requires careful control of the light and magnetic fields used to create the MOT. A well-balanced MOT requires circularly polarised beams with equal intensities so that there is no net force from scattering light. Otherwise, the MOT forms at a position where the magnetic field is not zero [43]. Equivalently, the MOT requires good control of the magnetic field inside the chamber. What follows is a description of the hardware used to implement this control. Section 4.4.1 describes the network of optical fibres used to control the frequency and power in each MOT beam. The electrical circuits used to control the strength of each bias field, as well as switching off the quadrupole coils, are described in Section 4.4.2

4.4.1 Optical Fibre Network

A network of fibre-based beam-splitters and AOMs distributes the light from the μ Quans fibre to each of the beams for the 2D and 3D MOTs. This provides independent control of the power and frequency of the light at each output of the fibre network. A diagram of this setup is shown in Figure 4.14. The μ Quans fibre output is polarised using a polarising beam-splitter before a HWP aligns it with the slow axis of a PM fibre. The light is first divided on a 1:2 beam-splitter, with 66% exiting one port, used for the 3D MOT. The 34% on the other port is split again using a 95:5 beam-splitter in the hope of making 32% of the input power available for the 2D MOT, leaving 1.7% for the push beam. The junctions between components are spliced together to minimise insertion loss, but still the output powers are significantly lower than that, as indicated in Figure 4.14. The slow axes of the spliced fibres are aligned so that the linear polarisation of the light is maintained. Independent control of each output is done using a *Gooch and Housego* fibre AOM with a central modulation frequency of 135 MHz.

The light for the 3D MOT is split using a 1:3 splitter into pairs of outputs for the light along the \vec{x} , \vec{y} and \vec{z} axes. Unlike the outputs for the \vec{x} and \vec{y} axes, the two used for light along the \vec{z} axis have separate AOMs. This is done so that during the experiment, a single beam along the \vec{z} axis can be used to blow away background atoms (see Section 5.3.4 for more details).

4.4.2 Magnetic Field Control

There are 5 pairs of bias coils used to control the zero of magnetic field - 3 for the 3D MOT and 2 for the 2D MOT. The current through each set of bias coils is controlled using a voltage-controlled current source. Figure 4.15 shows a diagram of the circuit

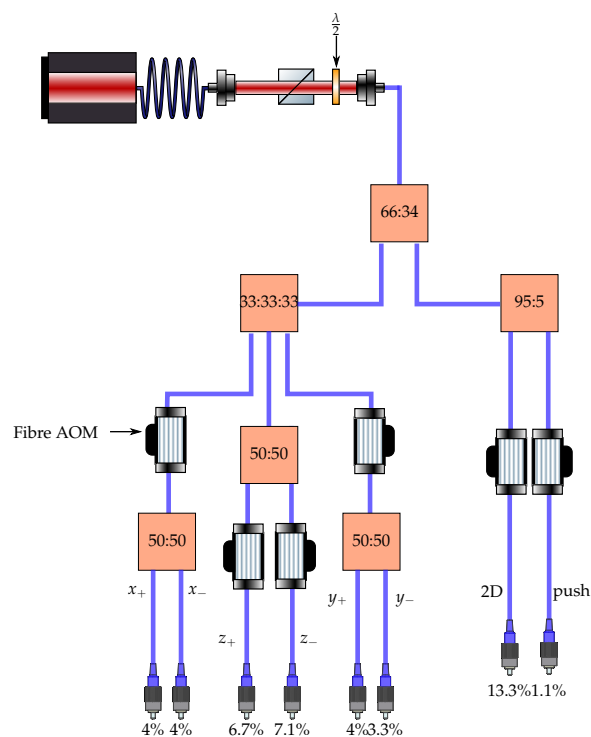


Figure 4.14: Fibre splitter and AOMs for MOT light distribution. The polarisation of the cooling and repump light from the μ Quans laser is aligned to the fibre network using a PBS and HWP. Apart from the outputs for the \vec{x} and \vec{y} 3D MOT beams, which have a single AOM per axis, the power and frequency at each output can be controlled independently. The percentages shown are the fractions of the input power at each output, when driving each AOM with the optimum RF power.

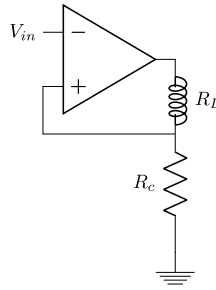


Figure 4.15: Circuit diagram for 3D MOT quadrupole coils and bias field coils. The current through the coils (shown as an inductor) is controlled using an input voltage V_{in} and a sense resistor R_c .

used to control the current through the bias coils and 3D MOT quadrupole coils. The control voltage is an input at the non-inverting terminal of an OPA549 op-amp. The coils are placed in series with a sense resistor of resistance R_s at the output. The circuit is configured so that the voltage at the inverting terminal is $V_- = iR_s$. This forms a negative feed-back loop to keep the output current constant if the load resistance changes. The bias coils can be supplied with up to 2 A using a control voltage of 10 V. This same circuit is used to control the 3D MOT coils.

During the experiment, the 3D MOT coils need to be switched off rapidly, to allow for effective sub-Doppler cooling of the atoms [44]. By actively controlling the current through the coils, their stored energy can be dissipated faster than the natural time constant $\tau = L/R$. This is done by applying a negative voltage across the coils. A flux-gate magnetometer was used to measure the time taken to switch off the coils. With an applied voltage of 0 V, the characteristic decay time is $\tau = 2.5$ ms. Under the maximum available backward bias of -24 V, the field can be completely switched off in $800\ \mu\text{s}$.

The quadrupole coils for the 2D MOT are switched off in much the same way. Figure 4.16 shows a diagram of the circuit used. An IGBT cuts the flow of current when the gate voltage drops below a threshold value. To prevent damage to the transistor, a diode and $10\ \Omega$ power resistor are placed in parallel with the coils. This allows the

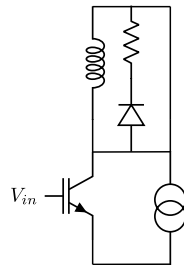


Figure 4.16: IGBT circuit for the 2D MOT quadrupole coils. The circuit is broken to switch the coils off, which generates a back-EMF. This flows through the diode and resistor in parallel with the coils, preventing damage to the IGBT.

current generated by the back-EMF to dissipate without damaging the IGBT. These field from these coils can be switched off in less than 1 ms.

4.5 Characterising the MOTs

This section discusses the performance of the 2D and 3D MOTs for trapping and cooling ^{87}Rb . The main goal of this stage of the experiment is to quickly produce an ensemble of trapped, cold atoms in the 3D MOT. For this reason, the loading rate of the 3D MOT is a useful figure-of-merit. As further cooling in an optical molasses is necessary to achieve a sufficiently cold ensemble for interferometry (see Section 5.2), the temperature of atoms in the MOT will not be discussed in detail.

At the start of the experiment, the light and magnetic fields to produce the 2D and 3D MOTs are switched on. Table 4.2 shows typical values for the total cooling and repump powers, as well as the field gradients and bias fields required to cancel the external stray field from the lab. The cooling light is detuned by -2Γ from the $|F = 2\rangle \rightarrow |F' = 3\rangle$ transition for the 2D MOT and by -2.5Γ for the 3D MOT. The push beam is at resonance. A timing diagram of the loading sequence is given in Figure 4.17. The light and quadrupole field for the 2D MOT are switched off after 100 ms and the 3D MOT is kept on for a further 50 ms to allow for the transit of the remaining atoms

from the 2D MOT to the 3D MOT. After a sufficient number of atoms are loaded, the experiment proceeds by switching off the 3D quadrupole field prior to cooling in an optical molasses.

| | 2D MOT | | 3D MOT | | | | |
|---------|-------------|------------------|-----------------------|----------------|--------|---------------|-----------------------|
| | Laser Power | Magnetic Field | Laser Power | Magnetic Field | | | |
| Cooling | 60 mW | $d\vec{B}/d\rho$ | 18 G cm ⁻¹ | Cooling | 130 mW | $d\vec{B}/dz$ | 15 G cm ⁻¹ |
| Repump | 6 mW | B_x | 0.48 G | Repump | 13 mW | B_x | 1 G |
| Push | 500 μ W | B_y | -0.46 G | | | B_y | -0.5 G |
| | | | | | | B_z | 0.22 G |

Table 4.2: Typical optical and magnetic parameters used for the 2D and 3D MOTs. The optical powers listed are the total used for each MOT, which is divided into separate beams. The bias field strengths are the values used during the preliminary trapping stage of the experiment to cancel the stray field from the lab. This depends on the location of the experiment, rather than the experiment itself. The specified field gradients are given along the radial direction and the symmetry axis of the quadrupole coils for the 2D and 3D MOTs, respectively.

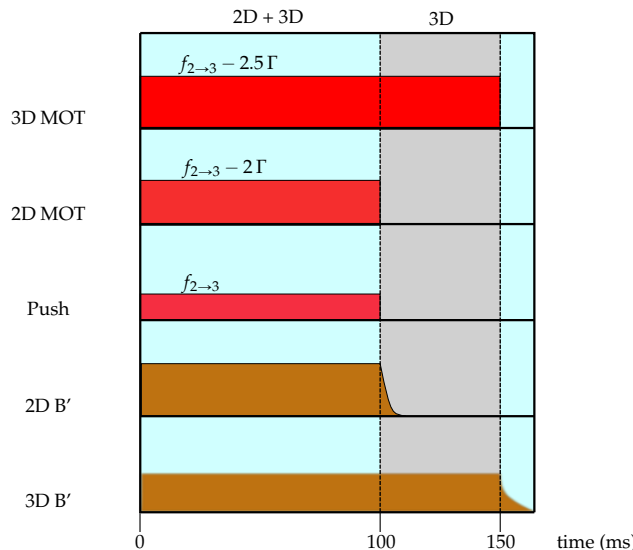


Figure 4.17: Timing diagram for the loading stage of the experiment. The 2D MOT is switched on for 100 ms and is switched off earlier than the 3D MOT.

4.5.1 3D MOT Loading Rate

The loading rate of the 3D MOT from a beam of atoms originating from the 2D MOT can be understood using the following rate equation

$$\frac{dN}{dt} = R\phi_{rb} - (\alpha\phi_{rb} + \beta n_{bg}) N - \gamma N^2 \quad (4.4)$$

where ϕ_{rb} is the flux of rubidium through 3D MOT capture volume and R describes the rate at which rubidium is cooled and trapped such that $R\phi_{rb}$ is the loading rate of the 3D MOT. The second term describes a loss rate due to collisions between trapped atoms and untrapped rubidium and background atoms. These loss rates are parameterised by α and β , respectively. The final term describes the loss of atoms from the trap due to intra-trap collisions [46] which depends on the density of atoms in the trap. At the number densities found in a MOT, the last term can be neglected, and then there is a simple solution for the number of atoms in the 3D MOT

$$N(t) = \frac{R\phi_{rb} \left(1 - e^{-t(\beta n_{bg} + \alpha\phi_{rb})}\right)}{\beta n_{bg} + \alpha\phi_{rb}} \quad (4.5)$$

which has a steady-state atom number given by

$$N_\infty = \frac{R\phi_{rb}}{\beta n_{bg} + \alpha\phi_{rb}} \quad (4.6)$$

Under a small atomic flux, both the loading rate and steady-state atom number increase as the flux of atoms from the 2D MOT increases. Once this flux is great enough, the loss due to untrapped rubidium collisions becomes non-negligible and the number of atoms in the MOT becomes independent of ϕ_{rb} . At very high pressures, this collision rate is great enough to cause a roll-off in the number of trapped atoms.

The flux of atoms from the 2D MOT depends on the 2D MOT loading rate, which in turn depends on the capture volume and the partial pressure of rubidium inside the source cell. The number of atoms in the 3D MOT was measured over time for a range of dispenser currents. At low partial pressures, the loading rate increases due to the increase in the flux from the 2D MOT. As the pressure increases, the increasing flux gives a larger steady-state number of atoms, up until the background pressure becomes negligible. Figure 4.18a and Figure 4.18b compare the loading curves observed with and without the push beam. Below a threshold pressure, the push beam greatly improves the loading rate since a greater fraction of the atoms can be captured in the 3D MOT.

Figure 4.18c shows the fitted loading rate for each scenario. There is a clear optimum pressure, where the loading rate is $2.4 \times 10^9 \text{ s}^{-1}$. The steady-state atom number is independent of the flux from the 2D MOT. Above this pressure, the loading rate is sharply reduced. The increased collision rate between cold atoms from the 2D MOT and hot untrapped ones reduces the atomic flux. This also increases the mean velocity of atoms in the beam, since faster ones are less likely to collide with a background atom before exiting the cell. At very high pressures, the mean velocity is so great that only a small fraction of atoms can be captured and the push beam has little effect on the loading rate.

4.6 Conclusion

This chapter has introduced the components of the experiment that were used to trap and cool atoms in a MOT. This is used to prepare an ensemble of cold atoms in a pure quantum state, suitable for interferometry. An optimisation of the loading rate of the

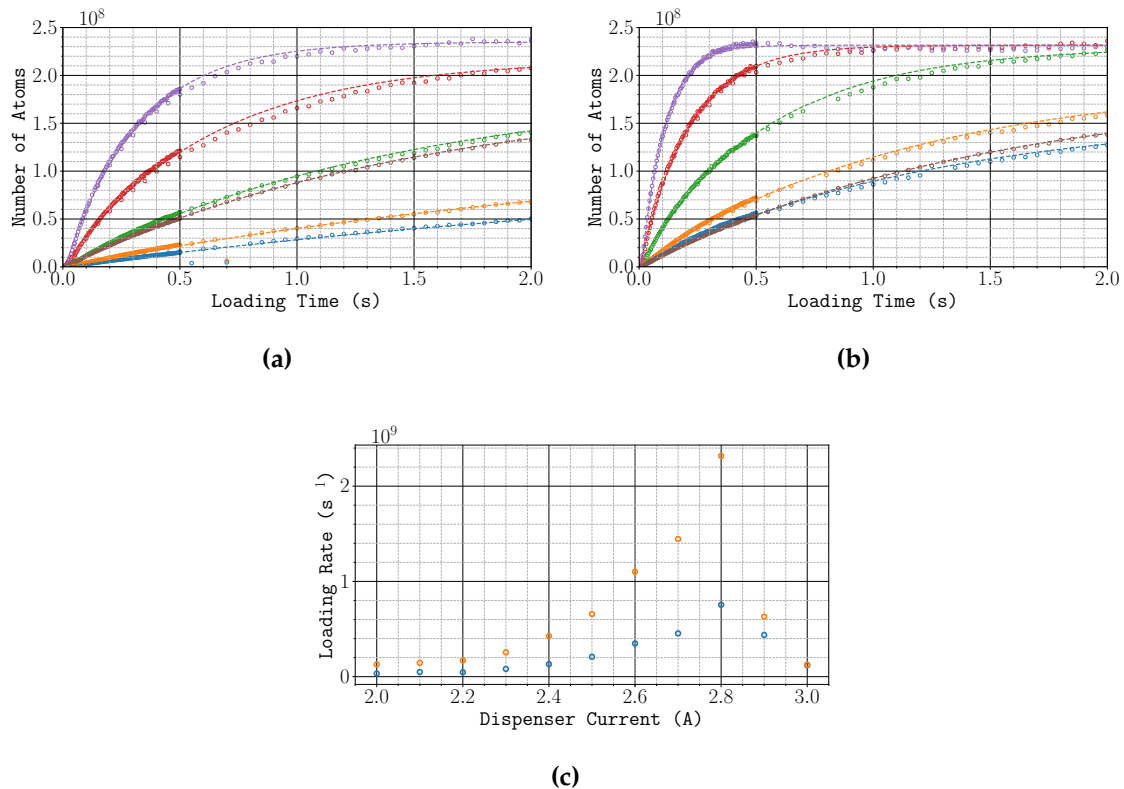


Figure 4.18: Number of atoms and loading rate for the 3D MOT (a) without push beam and (b) with push beam. For clarity, only the loading curves for dispenser currents of 2 A (blue), 2.2 A (orange), 2.4 A (green), 2.6 A (red), 2.8 A (purple) and 3 A (brown) (c) Loading rates ($R\phi_{rb}$ with (orange) and without (blue) push beam. As the partial pressure of rubidium increases, the flux of atoms from the source cell increases. By longitudinally cooling the atoms, the push beam enhances the loading rate of the 3D MOT. Above a dispenser current of 2.8 A, the collision rate with hot untrapped atoms greatly reduces the atom flux, reducing both the loading rate and steady-state atom number.

3D MOT was carried out to reduce the dead time between consecutive experiment cycles.

Chapter 5

Preparing Atoms for Interferometry

5.1 Chapter Overview

This chapter presents the stages of the experiment which prepare an ensemble of atoms for interferometry, after they are loaded into the 3D MOT. After being released from the trap, the atoms are cooled and launched using a moving molasses, as described in Section 5.2. Following this, a sequence of optical and microwaves pulses is used to increase the population in the $|1, 0\rangle$ ground state and end with an ensemble which has a narrow velocity spread along the Raman axis. A characterisation of this is given in Section 5.3.

Some sections of this chapter refer to parts of the experiment which have yet to be introduced. Details on the Raman laser and the velocity-selective Raman pulse can be found in Section 7.2 and Section 7.4.3, respectively. A description of the detection scheme, used to measure the population of atoms in $|F = 1\rangle$ and $|F = 2\rangle$ is presented in Section 7.3.

5.2 Cooling in Optical Molasses

A low thermal velocity means that the atoms can be interrogated for a longer time, $2T$, because the atom cloud spreads out more slowly. This in turn makes the accelerometer more sensitive because the interferometer phase is proportional to T^2 . Further cooling is therefore required before the most sensitive interferometer signal can be achieved. Temperatures well below that of the Doppler limit ($146 \mu\text{K}$ for ^{87}Rb) can be reached using polarisation gradient cooling [47]. In what follows, the principles of sub-Doppler cooling using polarisation gradients will not be discussed in detail, but can be found elsewhere [48, 49].

This section describes the work towards to cooling and launching the atoms in a moving optical molasses. It starts with a motivation for launching the atoms in Section 5.2.1. The following section discusses the control of the intensity and frequency of the light during the molasses stage of the experiment. A description of the techniques needed to cool the atoms in a moving molasses is then given in Section 5.2.3. Finally, this section concludes in Section 5.2.4 with measurements of both the temperature and trajectory of the atom cloud which were measured using a ballistic expansion method.

5.2.1 Motivation for Launching

As previously discussed in Section 2.4.3, there are two pairs of counter-propagating beams which can drive Raman transitions between the two hyperfine ground states. If an atom can be stimulated by both pairs, then the additional trajectories this introduces do not interfere, resulting in a reduction in the fringe visibility. This problem can be avoided by using the fact that the Raman transition is Doppler-sensitive to ensure that the atoms are only driven by one pair of beams. Each pair has an opposite Doppler shift $\pm\omega_D = \pm\mathbf{k}_{\text{eff}} \cdot \mathbf{v}$ and so their transition frequencies are separated by

$2\omega_D$. Therefore, the atoms are launched so that their centre-of-mass velocity along the Raman axis is large enough to lift the degeneracy of the two Raman transitions.

5.2.2 Frequency and Power Control

A timing diagram illustrating the power and frequency during the molasses phase is shown in Figure 5.1. After the atoms are loaded into the MOT, they are released by switching off the quadrupole field. Once this field has decayed away, the frequency and intensity of the cooling light are ramped adiabatically [50]. The frequency of the cooling light is ramped to -25Γ over 1.4 ms. Since the repump light is a sideband of the cooling light, the modulation frequency is simultaneously ramped up to keep this sideband resonant with the $|F = 1\rangle \rightarrow |F' = 2\rangle$ transition. Additionally, the relative detuning of counter-propagating MOT beams is varied so that the atoms are cooled into a moving molasses (see Section 5.2.3). After this, the intensity of the light is reduced over 5 ms. The response of the output AOM on the μ Quans laser was calibrated so that we could apply a voltage ramp that gives an approximately linear intensity ramp.

5.2.3 Launching in a Moving Molasses

The configuration for launching atoms along the Raman axis is shown in Figure 5.2. The forward-propagating beams are blue-detuned by $+\delta f_l$ and the backward-propagating ones are red-detuned by $-\delta f_l$, so that atoms with a velocity along the beam axis of $\vec{v} = \delta f_l \lambda$ are resonant with both beams. The frequency of each beam is ramped from the initial value by varying the modulation frequency of its AOM. This ramp occurs slowly to ensure strong cooling throughout the period of accelerating the atoms to their final velocity. As there is no pair of MOT beams along the axis of the Raman

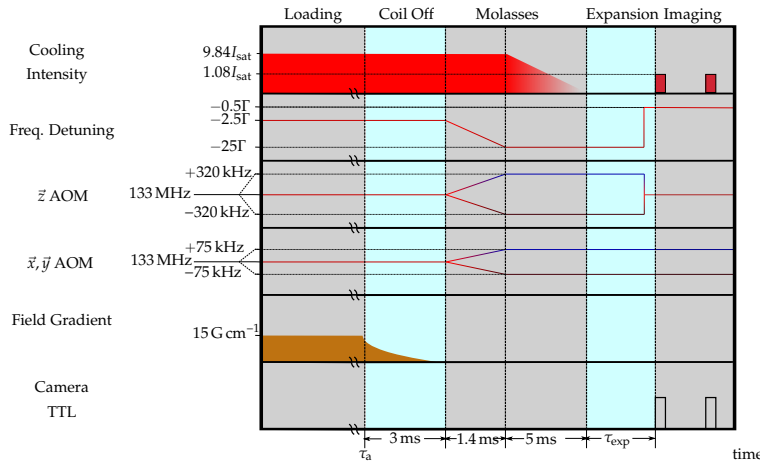


Figure 5.1: Timing diagram for the molasses stage of the experiment. After a time $\tau_a = 100$ ms, the atoms are released from the MOT. The molasses sequence begins 3 ms later, once the magnetic field from the MOT coils has decayed away. First, the frequency of the cooling light is ramped to -25Γ over 1.4 ms. The relative frequencies of counter-propagating MOT beams are detuned so that the atoms are cooled in a moving frame, launching them along a parabolic path (see Section 5.2.3). Next, the intensity of the MOT light is reduced linearly over 5 ms. To measure the temperature, the atoms are left to expand for a duration of τ_{exp} ms, after which they are imaged using the camera.

beams, the \vec{x} and \vec{y} MOT beams, whose axes are nominally at $\pm 45^\circ$ to the Raman axis, are used to launch the atoms. By controlling the power and alignment of each beam, the net velocity on the atoms will be along the Raman axis. If the detuning of both pairs of beams is the same, then the velocity along the Raman axis is given by $\vec{v}_r = \sqrt{2}\delta f_l \lambda$ [51].

As well as launching the atoms horizontally, the atoms are launched vertically so that they can remain closer to the centre of the chamber after the free fall time $2T$. This keeps them in a region of more uniform Raman beam intensity where the pulse area is more homogeneous across the cloud, giving better fringe visibility. This launch is carried out using the MOT beams that lie along the vertical \vec{z} axis.

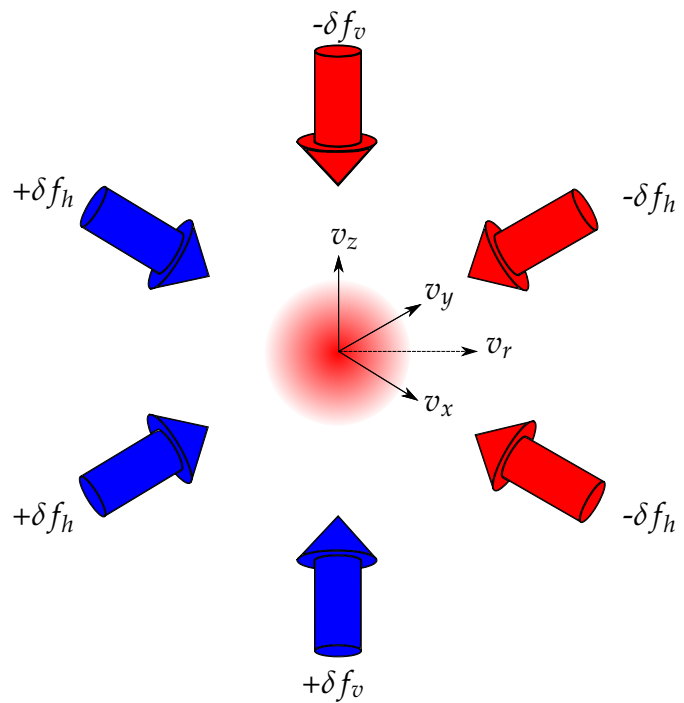


Figure 5.2: Beam configuration for a moving molasses. When counter-propagating beams are detuned from each other, the atoms are cooled into a moving frame where the Doppler shift brings both beams to the same frequency. Along the vertical axis, the beams are detuned by δf_v so that the cloud is launched upwards with a velocity $v_z = \delta f_v \lambda$. In the horizontal plane, the \vec{x} and \vec{y} beams are detuned by δf_h so that the resultant velocity is along the Raman axis $v_r = \sqrt{2} \delta f_h \lambda$.

5.2.4 Imaging the Atom Cloud over Time

Once released from the trap, the atom cloud is free to expand at a rate due to its thermal velocity distribution. In addition to this, the centre-of-mass moves due to its initial velocity and acceleration due to gravity (and any other external forces). The temperature of the cloud T was measured by imaging the distribution of atoms after allowing the cloud to expand in the dark for a range of expansion times. A typical atom cloud trajectory is shown in Figure 5.3, in which the cloud was imaged up to 76 ms after being released from the trap.

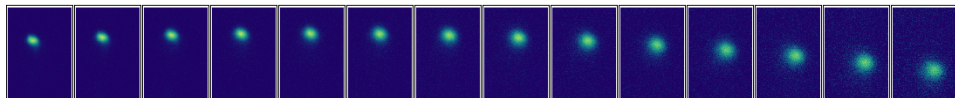


Figure 5.3: A series of images showing the trajectory of the atom cloud after being cooled in a moving molasses. The first image was taken 7 ms after initiating the molasses and a subsequent one every 5 ms. Each image represents a region of interest of dimensions 16.3 mm \times 23.4 mm that covers the spatial extent of the atom cloud during the launch.

Measuring the Temperature

In thermal equilibrium, the velocity distribution of the atoms is described by a Maxwell-Boltzmann distribution. The velocity component along one direction has the distribution

$$f(v_x) = \left(\frac{m}{2\pi k_B T} \right)^{1/2} e^{-\frac{m(v_x - \langle v_x \rangle)^2}{2k_B T}} \quad (5.1)$$

Assuming that the number density is initially a Gaussian, with a peak number density $n_0(x_0)$ at the centre-of-mass, and a mean square radius projected along x of σ_0^2 , the number density (projected along x) at later times is given by a convolution with equa-

tion (5.1)

$$n(x, t) = \int n_0(x_0) \left(\frac{m}{2\pi k_B} \right)^{1/2} e^{-\frac{m(v_x - \langle v_x \rangle)^2}{2k_B T}} e^{-\frac{(x + v_x t - x_0)^2}{2\sigma_0^2}} dv_x \quad (5.2)$$

where σ_0 is the $1/e^2$ initial width of the cloud. As a convolution of two Gaussians, equation (5.2) is also a Gaussian, with a mean-square radius (projected along x) given by

$$\sigma(t)^2 = \sigma_0^2 + \frac{k_B T}{m} t^2 \quad (5.3)$$

Figure 5.4 shows a typical density profile projected along each axis seen by the camera, as described in Section 4.2.3. The width along each axis is estimated using a non-linear least squares fit to equation (5.2). Along the vertical axis, it can be seen that the fit is poor on the left-hand side of the distribution. This can be explained by the irregular shape of the cloud. Close inspection of the images in Figure 5.3 shows a comet-like tail distribution of atoms. This is likely caused by an imbalance in the intensity, and hence scattering rate, from each MOT beam. In spite of this imbalance, the molasses was still able to cool the atoms to a sufficiently cold temperature. Figure 5.5 shows the measured cloud width over a range of expansion times. The initial measurement was made 7 ms after the end of the molasses to allow for enough time to re-lock the laser to -0.5Γ below the $|F = 2\rangle \rightarrow |F' = 3\rangle$ transition and align the bias field to the \vec{z} axis so that the atoms could be optically pumped into the $|2, 2\rangle$ state. The slopes of these graphs give the temperatures along the horizontal and vertical axes of the camera as $T_x = 6.38(11) \mu\text{K}$ and $T_y = 6.38(9) \mu\text{K}$, respectively.

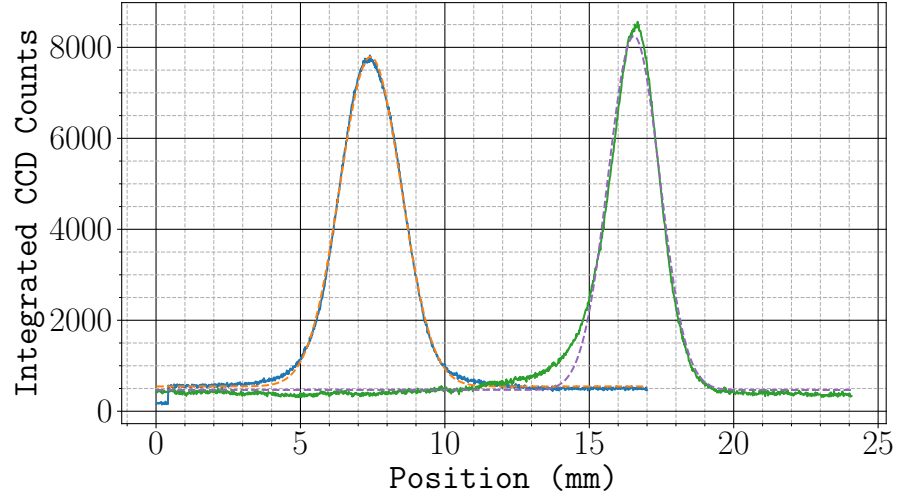


Figure 5.4: Integrated pixel count for a single image after 7 ms of ballistic expansion. The blue curve shows the profile along the horizontal axis while the profile along the vertical axis is shown by the green curve. The dashed lines indicate non-linear least squares fits to a Gaussian function.

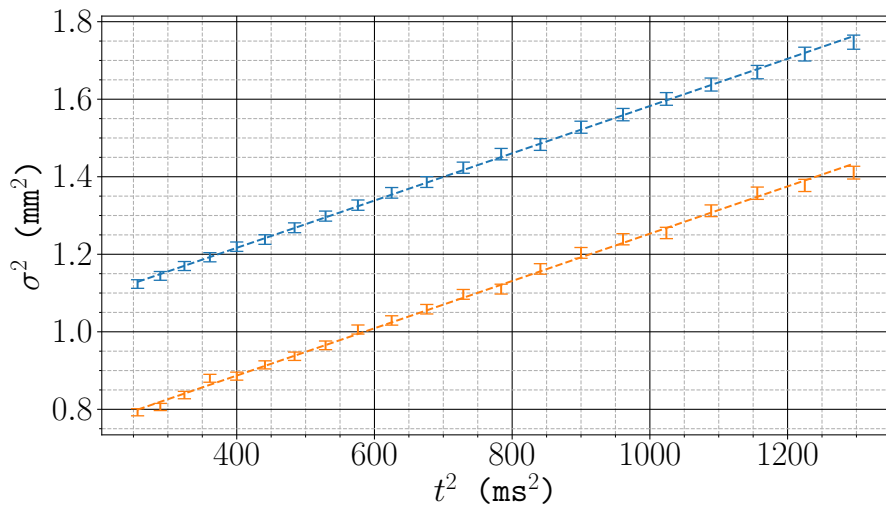


Figure 5.5: Mean squared cloud radius plotted against the square of the ballistic expansion time. After molasses, the cloud is left to expand in the dark and in a region of close to zero magnetic field. Least-squares fits to the camera images give the mean-square radii $\sigma(t)^2$ in the horizontal (blue) and vertical (orange) directions. The gradient of these curves gives temperatures $T_x = 6.38(11)$ μK and $T_y = 6.38(9)$ μK . The error bars are dominated by the systematic contribution from the magnification of the camera optics as opposed to the statistical uncertainty in the estimated width.

Measuring the Launch Trajectory

The same method used to measure the temperature of the cloud can also be used to measure the position of the centre-of-mass $\langle x(t) \rangle$. Since the cloud is in free-fall, the trajectory for the centre-of-mass is then given by the equation-of-motion for a particle moving under constant acceleration

$$\langle x(t) \rangle = \langle x(0) \rangle + v_x t + \frac{1}{2} a_x t^2, \quad (5.4)$$

where v_i is the initial velocity along the given axis and a_i is the acceleration.

To launch the atoms vertically, the (z_+, z_-) AOMs were ramped so that the frequency difference between the light beams was 2×320 kHz. To launch along the Raman beams, the x and y AOM frequencies were ramped to give a frequency difference of 2×75 kHz between each pair of horizontal MOT beams. Figure 5.6 is a plot of the measured centre-of-mass position along the horizontal and vertical camera axes over time. A linear least-squares fit to equation (5.4) gives a vertical launch quantities of $v_v = 25.00(24)$ cm s $^{-1}$ and $a_v = -9.400(51)$ m s $^{-2}$ and $v_h = 7.39(14)$ cm s $^{-1}$ and $a_h = -0.320(36)$ m s $^{-2}$ along the horizontal axis.

When compared to the expected velocities from the detunings, $v_v^{(l)} = 24.96$ cm s $^{-1}$ and $v_h^{(l)} = 5.85$ cm s $^{-1}$, the measured horizontal velocity is far greater than expected. This can be explained by a residual magnetic field, that is not cancelled using the bias coils. In the presence of a magnetic field, atoms cooled in an optical molasses are decelerated to a velocity at which the Zeeman shift is cancelled by the Doppler shift. This velocity-selective resonance depends on the orientation of the magnetic field to the polarisation of the light. In a one-dimensional optical molasses, a resonance occurs at $v_{\text{res}}^{(1)} = -\mu_B g_F B / \hbar k$ when the magnetic field is aligned with the wavevector of the light [52]. When the field is aligned at an arbitrary angle an additional resonance

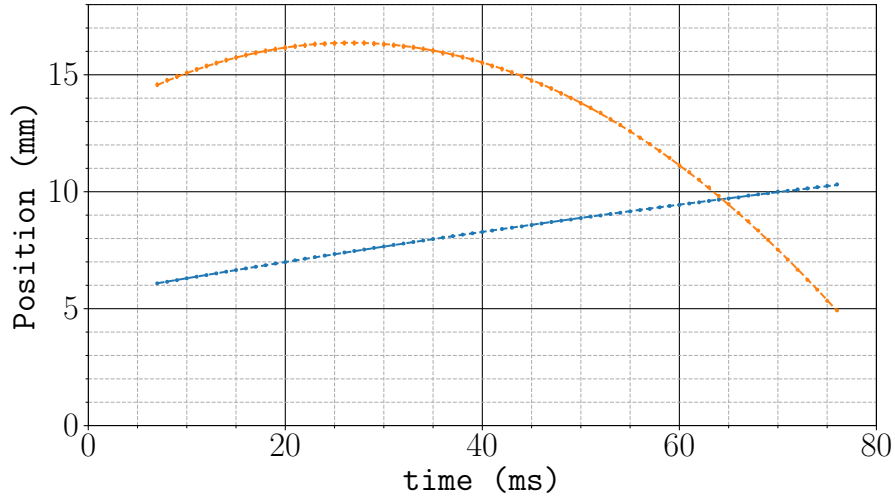


Figure 5.6: Measured centre-of-mass position over time. The horizontal component of the position is shown in blue and the vertical in orange. Each trajectory is fit to equation (5.4) to estimate the launch velocity. The best-fit values are $v_v = 25.00(24) \text{ cm s}^{-1}$ and $a_v = -9.400(51) \text{ m s}^{-2}$ along the vertical axis and $v_h = 7.39(14) \text{ cm s}^{-1}$ and $a_h = -0.310(36) \text{ m s}^{-2}$ along the horizontal.

at $v_{\text{res}}^{(2)} = -\mu_B g_F B / 2\hbar k$ is present, due to additional $(\sigma^\pm - \pi)$ transitions [53, 54]. A residual field along the Raman axis of 20 mG would shift the resonance along \vec{x} and \vec{y} by 1.09 cm s^{-1} corresponding to a velocity of 1.54 cm s^{-1} along the Raman axis. The magnetic field inside the chamber is controlled using bias coils and no attempt was made to cancel magnetic field gradients. It is plausible that a residual field of this magnitude is a result of a magnetic field gradient. For the moment, this does not cause a problem as we simply adjust the molasses detuning to achieve the desired launch velocity. In future, a precisely known launch velocity may be required for sensing rotations, and then it will be necessary to return to this issue.

5.3 State Preparation

After the atoms have been cooled in an optical molasses, the population will mostly be distributed across the $|F = 2, m_F\rangle$ sublevels, along with a small fraction distributed across the $|F = 1, m_F\rangle$ sublevels. With a sufficiently large magnetic field to lift the Zeeman degeneracy and under an appropriate choice of light polarisation, the Raman transition only couples the $|1, 0\rangle$ and $|2, 0\rangle$ states. Atoms in the other hyperfine ground states cannot participate in the interferometer. In fact, since the individual Zeeman sub-levels are not resolved during detection, these background atoms result in a loss of fringe visibility.

The following section discusses a method of preparing the atoms to increase the population in the $|1, 0\rangle$ ground state and minimise the population in all other states. An overview of the scheme is given in Section 5.3.1. This is followed by a discussion of the initial steps which optically pump atoms into the $|1, 0\rangle$ state in Section 5.3.2. A description of the microwave pulse used to drive atoms into the $|F = 2\rangle$ level is given in Section 5.3.3. This section concludes with the method used to blow away the atoms which do not contribute to the interferometer in Section 5.3.4. A key step which has been omitted is the velocity-selective Raman pulse. This is described in more detail later, in Section 7.4.3.

5.3.1 Schemes for Preparation

The scheme used to prepare atoms in the $|1, 0\rangle$ state is the following:

1. Light resonant with the $|F = 2\rangle \rightarrow |F' = 2\rangle$ transition pumps all the $|F = 2\rangle$ atoms into the $|F = 1\rangle$ level.

2. Light resonant with the $|F = 1\rangle \rightarrow |F' = 0\rangle$ transition drives (σ^\pm) transitions to pump atoms into the $|1, 0\rangle$ dark state
3. A microwave π -pulse transfers those atoms to $|2, 0\rangle$
4. A long Raman π -pulse selects a narrow velocity group of atoms in $|2, 0\rangle$ and transfers them back to $|1, 0\rangle$.
5. The atoms which remain in $|F = 2\rangle$ are blown away

A diagram of the population of each hyperfine ground state and the laser frequencies used to drive these transitions is given in Figure 5.7. With the exception of step 4, the light is provided by the μ Quans laser using the MOT collimators aligned to the vertical \vec{z} axis. The frequency of the cooling laser and the repump sideband are set so that the relevant transitions for steps 1 and 2 are addressed.

A timing diagram of the state preparation sequence is shown in Figure 5.8, which indicates the duration for which each optical or microwave pulse is applied, as well as the direction of the applied magnetic field. The field is rotated slowly over 2 ms (which is omitted from the diagram) to preserve the spin state of each atom. The spin state precesses at the Larmor frequency, which is 1.4 MHz G^{-1} . With an applied magnetic field on the order of 1 G, the spin precession period is around $0.7 \mu\text{s}$, so the orientation of the magnetic field evolves at a much slower rate.

5.3.2 Optically Pumping the Atoms

Driving the $|F = 2\rangle \rightarrow |F' = 2\rangle$ transition

After the molasses, the frequency of cooling light is 150 MHz below the $|F = 2\rangle \rightarrow |F' = 3\rangle$ transition. This can off-resonantly excite an atom to the $|F' = 2\rangle$ excited level, but the small scattering rate means that on average, an atom will need to scatter

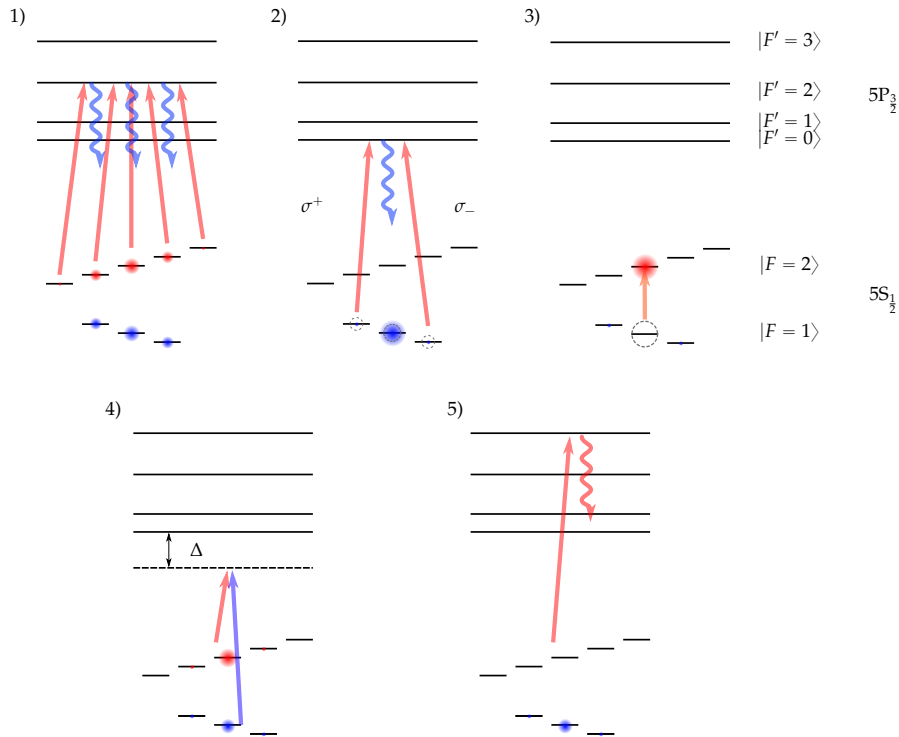


Figure 5.7: Sequence of optical and microwave pulses used to prepare an ensemble of velocity-selected atoms in $|1,0\rangle$. The red arrows indicate optical transitions to and from $|F = 2\rangle$ and equivalently for the blue arrows and $|F = 1\rangle$. A residual population is left in the $|1,\pm 1\rangle$ states, which contributes a background to the interferometer fringes.

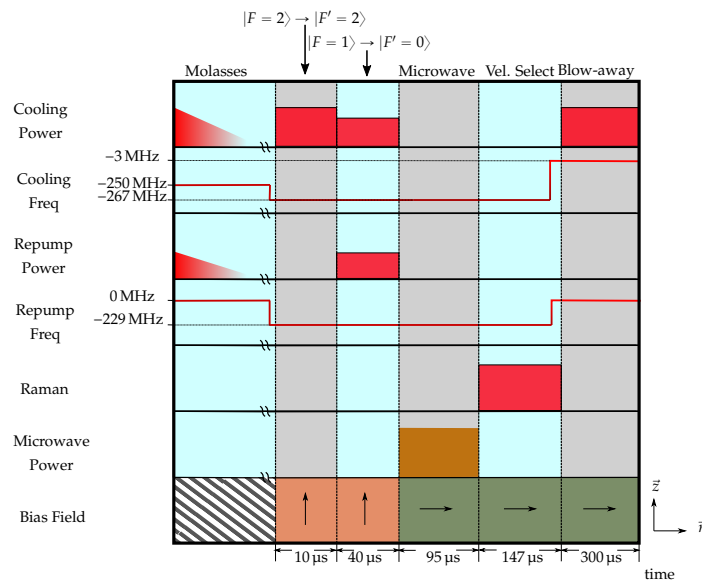


Figure 5.8: Timing diagram for state selection sequence. The durations labelled are indicative of the time required to drive the atoms into the desired state at each step. After the $|F = 1\rangle \rightarrow |F' = 0\rangle$ pumping, the magnetic field is re-oriented along the Raman axis \vec{r} . The 2 ms field switching time has been omitted.

many photons before it is pumped into the $|F = 1\rangle$ level. Therefore, to minimise the heating during this pumping process, the frequency of the cooling light is shifted to be resonant with the $|F = 2\rangle \rightarrow |F' = 2\rangle$ transition.

Figure 5.9 shows the population in the two hyperfine ground states as the duration of the $|F = 2\rangle \rightarrow |F' = 2\rangle$ light is increased. The rate at which atoms are pumped into $|F = 1\rangle$ increases with the strength of the applied magnetic field. At zero field, there exists a dark state which is a coherent superposition of the $|2, m_F\rangle$ states [55]. Applying a magnetic field lifts the degeneracy between the Zeeman sub-levels so that this dark state is no longer stationary. The evolution rate of this dark state, and hence pumping rate, increases with an increasing Zeeman shift. At a field strength of 3 G, the atoms can be pumped into $|F = 1\rangle$ in less than 5 μs .

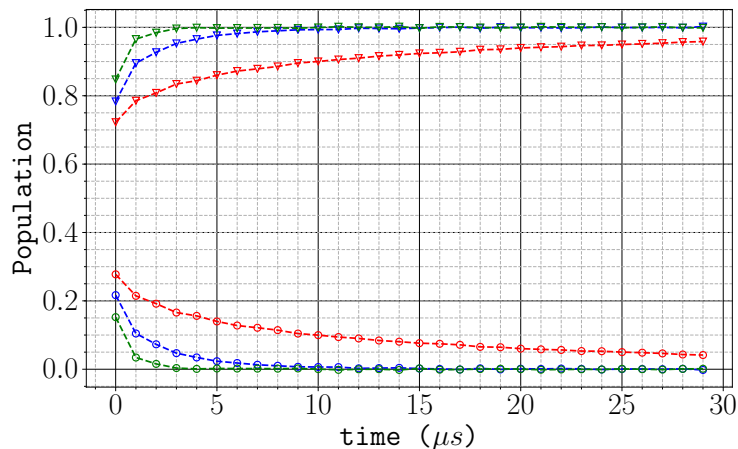


Figure 5.9: Population across the two hyperfine ground states after $|F = 2\rangle \rightarrow |F' = 2\rangle$ pumping under various magnetic field strengths. The \circ (\triangledown) markers indicate the population in $|F = 2\rangle$ ($|F = 1\rangle$). The red, blue and green series correspond to field strengths of -0.16 G, 1.67 G, and 3 G, respectively.

Driving the $|F = 1\rangle \rightarrow |F' = 0\rangle$ transition

After this first pumping step, the atoms are distributed across the Zeeman sub-levels in $|F = 1\rangle$. The next pulse of light is used to increase the population in $|1, 0\rangle$ by driving $|F = 1\rangle \rightarrow |F' = 0\rangle$ transitions. During this time, the $|F = 2\rangle \rightarrow |F' = 2\rangle$ light remains on which helps to prevent atoms from populating the $|F = 2\rangle$ level through off-resonant $|F = 1\rangle \rightarrow |F' = 1\rangle$ excitations. The magnetic field is directed along \vec{z} so that the circularly-polarised \vec{z} MOT beams only drive σ^\pm transitions. This makes the $|1, 0\rangle$ state a dark state into which all the atoms should be optically pumped.

The distribution of atoms across the Zeeman sublevels was measured using a microwave pulse to drive atoms into the $|F = 2\rangle$ level, which is described in Section 5.3.3. For each π microwave transition, the frequency of the microwave field was varied to find the resonant frequency. The resulting spectra for $m_F = -1$ and $m_F = 0$ are shown in Figure 5.10, both with (blue curves) and without (orange curves) applying light to pump into the $|1, 0\rangle$ state. It can be seen that the $m_F = 0$ population is enhanced while the $m_F = -1$ population is suppressed. From Figure 5.10b, the first-order Zeeman shift (1.4 MHz G^{-1}) of the $m_F = -1$ state is -4.435 MHz , which gives a field strength of 3.17 G . This is in close agreement with the value measured from the second-order shift of the $0 \rightarrow 0$ clock transition. Fitting the central peak of the blue curve in Figure 5.10a to a Lorentzian gives a shift from the hyperfine splitting frequency of 5.6 kHz . The second order Zeeman shift is 575.15 Hz G^{-2} , so the corresponding field strength is 3.12 G .

A plot of the population in each Zeeman sub-level for increasing pumping times is given in Figure 5.11. In this instance, the optical pumping does not completely deplete the population from the $m_F = \pm 1$ sub-levels. After pumping for $30 \mu\text{s}$, approximately 5% of the population remains in the $m_F = \pm 1$ sub-levels. The $|1, 0\rangle$ state can only be excited to $|F' = 0\rangle$ by π -polarised light, which suggests that the magnetic field

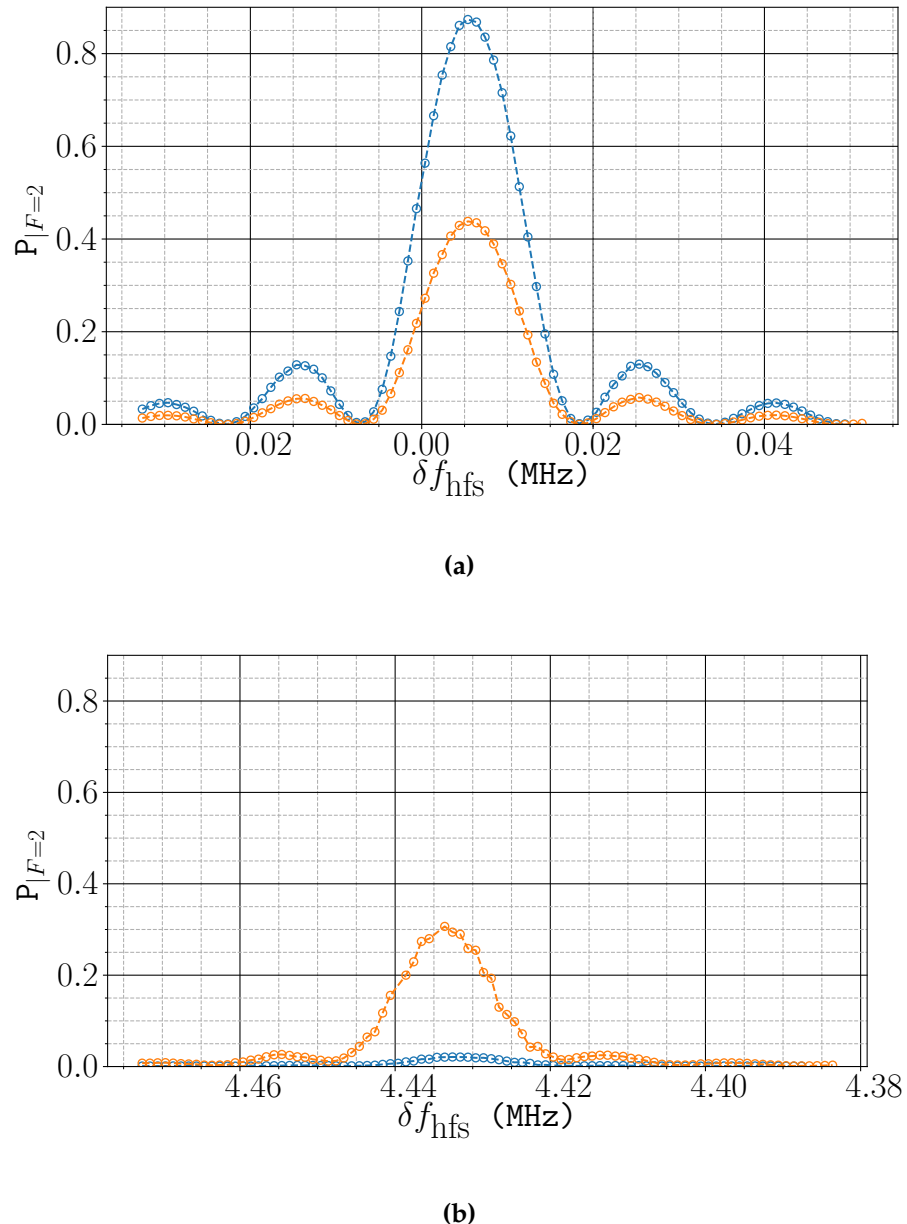


Figure 5.10: Population of atoms in (a) $|1, 0\rangle$ and (b) $|1, -1\rangle$, measured by applying a $68 \mu\text{s}$ microwave pulse to drive atoms into the $|F = 2\rangle$ level. The orange and blue points indicate the measured populations with and without $|F = 1\rangle \rightarrow |F' = 0\rangle$ pumping. The microwave frequency is plotted as a detuning from the hyperfine splitting frequency f_{hfs} .

is mis-aligned with the \vec{z} MOT beams. If the spherical components (σ^- , π , σ^+) of the dipole operator have values $(\sqrt{(1 - \epsilon^2)/2}, \epsilon, \sqrt{(1 - \epsilon^2)/2})$, a value of $\epsilon = 0.085$ is consistent with a residual $m_F = \pm 1$ population of 5%. For circularly polarised light, a π -component of this magnitude can be caused by a mis-alignment of the magnetic field from the \vec{z} axis of 2.4° . This is reasonable given that the coils were fixed around the vacuum chamber without accurately aligning to the vertical axis of the chamber¹. The effect of these background atoms on the measured interferometer signal is discussed later, in Section 7.3.3.

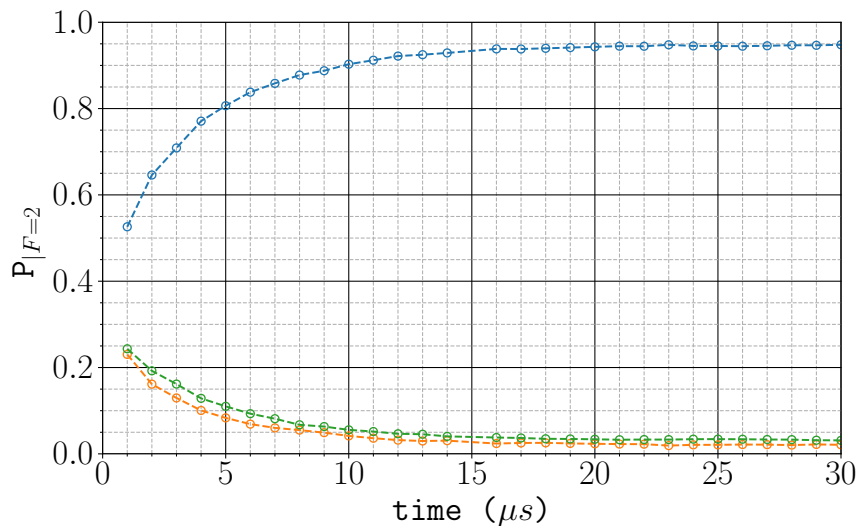


Figure 5.11: Population in each Zeeman sub-level as the $|F = 1\rangle \rightarrow |F' = 0\rangle$ pumping time is increased. The $m_F = 0, -1, +1$ populations are shown in blue, orange and green, respectively. After $30\ \mu\text{s}$, approximately 5% of the population remains in the $m_F = \pm 1$ sub-levels.

¹The alignment of the magnetic field has been subsequently improved and has indeed resulted in a reduction in the residual $m_F = \pm 1$ population to less than 1%

5.3.3 The Microwave Transitions

Microwave Generation

A diagram of the microwave setup is shown in Figure 5.12. The microwave radiation is generated using a *Wind-Freak* synthesiser oscillating at a frequency close to the hyperfine splitting frequency, $f_{\text{hfs}} = 6.838\,46\,\text{GHz}$. This is amplified by a *MiniCircuits MCL ZRON-8G+* amplifier and directed into the chamber using a *Pasternack PE9859/SF-10* microwave horn, which produces a linearly-polarised microwave field. The horn was aligned to the chamber at the position which maximised the population of atoms in the $|2, 0\rangle$ state. The synthesiser is clocked using a stable 100 MHz signal from the μ Quans laser. When the synthesiser was clocked using its internal 27 MHz reference clock, this produced a noticeable jitter in the output frequency, which led to a significant shot-to-shot fluctuation in the $|2, 0\rangle$ population.

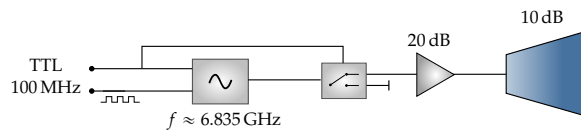


Figure 5.12: Schematic diagram of the microwave assembly. The frequency close to the hyperfine splitting frequency is generated by a *Wind-Freak* synthesiser. A 100 MHz clock signal acts as a stable reference frequency for the synthesiser. The generated microwave power is amplified by a low-power *Mini-Circuits* amplifier, before the microwave horn produces a highly directional, linearly polarised wave. The output is switched on and off using one digital signal at both the synthesiser and at a bi-directional microwave switch. The second port of this is terminated to prevent reflections. A USB connection to the synthesiser is used to control both its power and frequency.

Pulse Characterisation

The blue curve in Figure 5.13a shows a spectrum obtained by varying the frequency of the microwave pulse with an applied magnetic field along the \vec{z} axis of 0.67 G. This spectrum has a central line due to the $\Delta m = 0$ transition from $|1, 0\rangle$. The peaks on either

side of that are a mix of transitions out of $|1, 0\rangle$ and $|1, \pm 1\rangle$. At the far left and right are the peaks from the $\Delta m = 0$ transitions out of ± 1 . The seven transitions that make up these five peaks are illustrated in Figure 5.13b. The orange curve in Figure 5.13a shows that the population in $|1, m_F = \pm 1\rangle$ is very small after the $|F = 1\rangle \rightarrow |F' = 0\rangle$ pumping step is applied. The linewidth of the microwave transition is much narrower than the Zeeman splitting, so only the clock transition is driven when a pulse with a frequency close to f_{hfs} is applied.

Figure 5.14 shows a measurement of the population in the $|F = 2\rangle$ level for increasing durations of the applied microwave pulse. Rabi oscillations between the $|1, 0\rangle$ and $|2, 0\rangle$ states are clearly present. The loss of coherence between the states can be explained by an inhomogeneous driving field. Once inside the chamber, the microwaves reflect and scatter off the interior surfaces which results in a spatially-dependent Rabi frequency. The data is fit to an exponentially damped Rabi oscillation given by

$$P_{|F=2\rangle} = e^{-\gamma t} \sin(\Omega t)^2 \quad (5.5)$$

and gives a characteristic time of $\tau = 1/\gamma = 1016 \mu\text{s}$. It is clear that equation (5.5) does not exactly described the observed dephasing. This is not surprising given that there is no reason that an inhomogeneous microwave field should give an exponential dephasing rate. Nevertheless, this indicates that the coherence time between the two $m_F = 0$ states is sufficiently long. The Raman pulses have linewidths on the order of 100 kHz, with durations on the order of 10 μs . Over this time, the two states remain coherent.

A further cause of inhomogeneity is a mis-alignment of the microwave field to the magnetic field. Referring to Figure 5.13b, the $|1, m\rangle \rightarrow |2, m - 1\rangle$ transitions have the same transition frequency as $|1, m - 1\rangle \rightarrow |2, m\rangle$ transitions. These are the transitions labelled **(b)** and **(d)** in Figure 5.13a. The fact that σ^\pm transitions were observed means

that the microwave field was not parallel with the magnetic field. Initially, around 85% of the $|F = 1\rangle$ population was driven into $|F = 2\rangle$ using a microwave pulse of 100 μs . After improving the alignment of the magnetic field during the microwave pulse, this fraction increased to 97% - the remaining 3% being distributed across the $m_F = \pm 1$ states. The strength of the σ^\pm transitions was also reduced, so that a larger fraction of the $|1, 0\rangle$ population is driven into $|2, 0\rangle$.

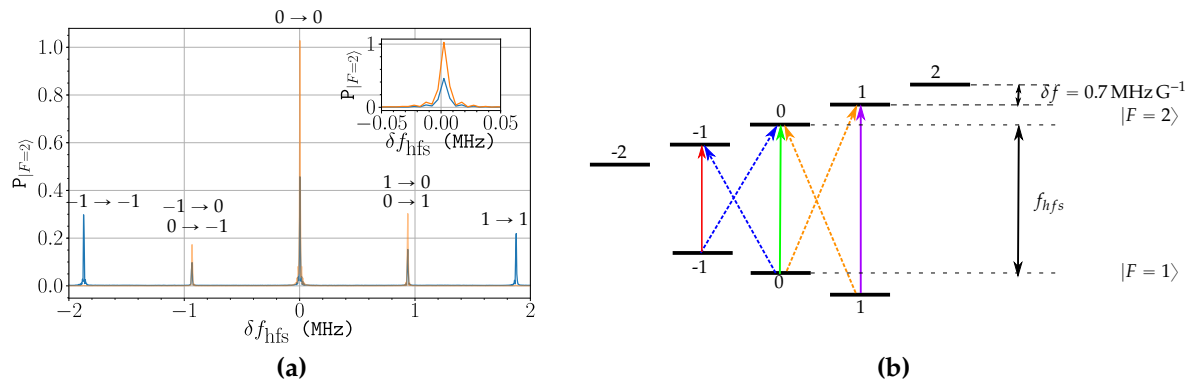


Figure 5.13: (a) shows the microwave transition spectrum before (blue) and after (orange) $|F = 1\rangle \rightarrow |F' = 0\rangle$ pumping. The inset is a magnification around δf_{hfs} showing the $m_F = 0 \rightarrow m'_F = 0$ clock transition. (b) shows the transitions addressed as the microwave frequency is varied. Dashed and lines indicate $\Delta m = \pm 1$ transitions and solid lines indicate $\Delta m = 0$. In order of increasing frequency, the transitions in (a) are highlighted in: red, blue, green, orange and purple.

5.3.4 Blow-Away

After the atoms populate $|2, 0\rangle$, a velocity-selective Raman π -pulse is applied to transfer a fraction of those back into $|1, 0\rangle$ [56]. This step is discussed in detail in Section 7.4.3. The velocity-selective Raman pulse transfers 4% the atoms back to $|1, 0\rangle$. The atoms remaining in $|F = 2\rangle$ need to be removed, otherwise they contribute a large background signal to the interferometer fringes.

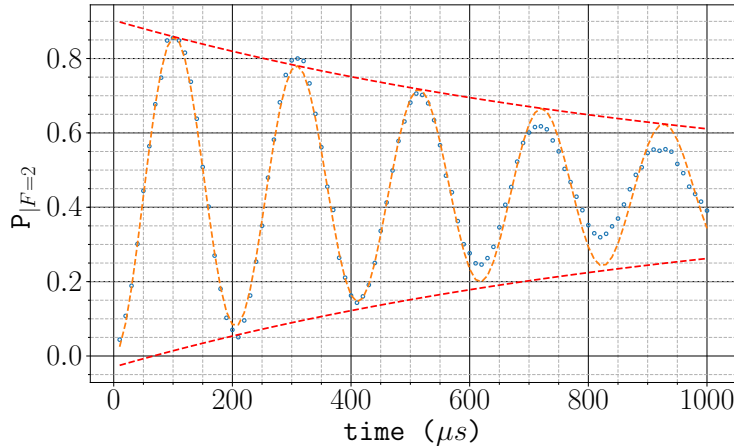


Figure 5.14: Damped Rabi oscillation between $|1,0\rangle$ and $|2,0\rangle$ using a microwave pulse of varying length. At longer pulse times, there is a loss of coherence due to a dephasing between the two states. The red dashed line is an envelope is a fit to a decaying exponential with a characteristic time of $\tau = 1016 \mu\text{s}$.

The final pulse during the state preparation sequence is used to push these non-contributing atoms out of the interferometer region. A single MOT beam is used so that there is a net momentum transfer to the atoms as they absorb light and fluoresce. The frequency of this blow-away beam is detuned from the $|F = 2\rangle \rightarrow |F' = 3\rangle$ transition by -3 MHz , which is the same frequency used for detection (see Section 7.3). A pulse of $50 \mu\text{s}$ is enough to remove all atoms in $|F = 2\rangle$.

5.4 Conclusion

This chapter has presented the stages of the experiment which are used to prepare an ensemble of atoms for interferometry. This requires cooling the atoms to limit the thermal expansion of the cloud during interferometry. The atoms are also launched using a moving molasses so that only one pair of beams is resonant with the Raman transition. Finally, we then apply a sequence of optical and microwave pulses, to increase the population of atoms in $|1,0\rangle$. A velocity-selective Raman pulse with a

narrow linewidth is used to make the velocity spread along the Raman axis much smaller than the Doppler width. Aside from some residual population in $|1, \pm 1\rangle$, the remaining atoms are removed using a pulse of light close to resonance with the $|F = 2\rangle \rightarrow |F' = 3\rangle$ transition. This results in an ensemble of which around 40% of the population contributes to the interferometer signal, the rest being the atoms that were left in $|1, \pm 1\rangle$.

Chapter 6

Raman Optical System

6.1 Chapter Outline

This chapter presents in detail the optical system used to produce a large collimated beam for driving Raman transitions. It begins with a motivation of the need to minimise intensity gradients and wavefront distortions in Section 6.2. This is followed by a description of the components that form the collimator in Section 6.3. Section 6.4 presents an overview of the retro-reflection assembly.

6.2 Requirements

This section outlines the optical characteristics of the light which affect the sensitivity of the atom interferometer. These are discussed in the context of this experiment, where gravity induces transverse motion across the light. The light beams that drive the Raman transition have a intensity profile that varies radially, e.g. along the axis parallel to gravity. The motion of the atoms through a gradient of intensity leads to

a variation in the Rabi frequency that reduces the interferometer fringe contrast and decreases acceleration sensitivity [57]. This places requirements on the beam waist size, which are discussed in Section 6.2.1.

The atom interferometer senses acceleration through the second derivative of the phase of the beat note between the two counter-propagating light fields that drive the Raman transition. Any such phase derivative that does not result from the acceleration of the atoms along the Raman axis is a source of error. One such source is distortion of the Raman beams wavefronts, which can arise from transmission through imperfect optical elements. Because vacuum windows are birefringent and have significant variations in optical thickness, the Raman optical system, described in Section 6.3, was mounted inside the chamber. It was built using optical elements having far better surface qualities than conventional optics. The effect of wavefront distortions as a source of phase noise is discussed in Section 6.2.2.

6.2.1 Gradients of Intensity

The effects of a gradient of intensity on the fringe contrast can be shown by considering an ensemble of atoms with a Gaussian distribution of position. Neglecting the effect of the ensemble's velocity distribution on the Raman detuning, the Rabi frequency Ω varies only as a function of the radial displacement ρ from the optic axis. Recalling Section 2.3.2, the state of the atom (see equation (2.26)) depends on the Rabi frequency Ω , detuning δ , duration τ and phase ϕ of each pulse. The fringe contrast over the ensemble is then a convolution of the contrast for a single atom with the atomic density distribution

$$\mathcal{C} = \int_0^{\infty} \frac{\rho}{\sigma_c^2} e^{-\rho^2/(2\sigma_c^2)} c(\Omega(\rho - \rho_1), \Omega(\rho - \rho_2), \Omega(\rho - \rho_3)) d\rho \quad (6.1)$$

where σ_c is the rms radius of the atom cloud projected along any one Cartesian axis. The fringe contrast for a single atom, denoted by c , is defined in equation (2.28). The arguments refer to the Rabi frequency during each pulse. The duration of each pulse is chosen such that an atom at the centre-of-mass radius ρ_i has a $\pi/2$ or π rotation. It is assumed that the two light beams which drive the Raman transition have the same waist size and Rabi frequency, determined by the product of the electric fields (see equation (2.15)). Therefore, the position-dependent Rabi frequency is

$$\Omega(r) = \Omega_0 e^{-2\rho^2/w^2} \quad (6.2)$$

where Ω_0 is the Rabi frequency along the optic axis and w is the waist size – the distance at which the electric field falls to $1/e$ of its peak value.

Figure 6.1 shows the fringe contrast as a function as beam waist for an atom cloud of rms radius $\sigma_c = 5$ mm and a time between interferometer pulses of $T = 25$ ms for three cases. The state of each atom is calculated using the intensity distribution, atomic trajectory and spatial distribution to determine the Rabi frequency for each atom during each pulse. The contrast for each atom is then determined from the difference in population for interferometer phases of $\Phi = 0$ and $\Phi = \pi/2$ so that the fringe contrast over the ensemble can be calculated using equation (6.1). The blue curve shows the contrast when the atom cloud is initially at the centre of the laser and falls from rest under gravity so that centre-of-mass coordinates are $(0, -\frac{1}{2}gT^2, -2gT^2)$ respectively. The orange curve includes the vertical velocity of $u = 25$ cm s⁻¹ that the atoms are launched with by the molasses. Finally, the green curve displaces the starting position of the atom cloud to an initial position $\rho_0 = \frac{uT}{2} - \frac{gT^2}{4}$, so that each pulse is displaced by the same amount from the centre of the beam and the cloud sees the same intensity gradient. For small beam waists, the intensity gradient across the cloud significantly reduces the fringe contrast, particularly when the atoms are not

launched. A beam waist much greater than the width of the cloud is necessary to achieve a large contrast.

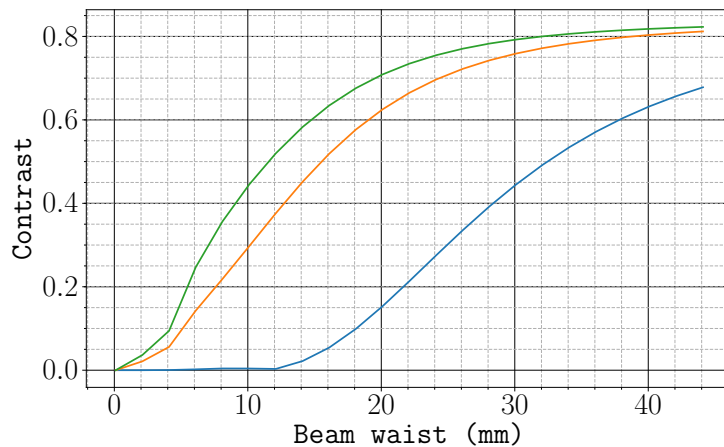


Figure 6.1: Simulated fringe contrast as a function of waist size w for an atom cloud falling under gravity. This model assumes a Gaussian distributed atomic density with a rms radius $\sigma_c = 5$ mm and a time between interferometer pulses of $T = 25$ ms. The blue curve shows the contrast when the atoms fall from rest under gravity. The orange curve includes the vertical launch velocity provided during the molasses phase. In the green curve, the atoms are displaced from the centre such that each pulse has the same intensity gradient (see text).

The velocity distribution of the atoms inhomogeneously detunes each Raman pulse due to the Doppler shift, as well as modifying the spatial distribution due to thermal expansion. Figure 6.2 shows the fringe contrast when including the velocity distribution of an atom ensemble with a temperature of $5 \mu\text{K}$. The most significant difference is for small beam waists in the case of no initial launch velocity, where the contrast is now less suppressed. Aside from this, the fringe contrast is not hugely affected by the velocity distribution of the atoms.

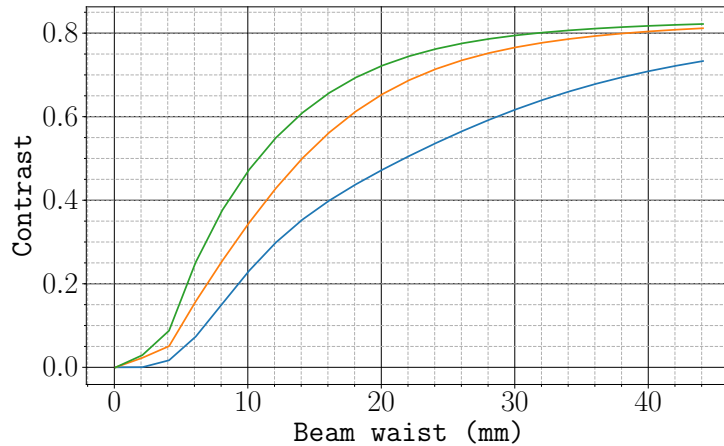


Figure 6.2: Simulated fringe contrast as a function of waist size w , including the effects of a velocity distribution along the Raman beam corresponding to a temperature of $5 \mu\text{K}$. The other parameters are the same as those used in Figure 6.1.

6.2.2 Wavefront Distortions

Systematic Effects

The field that drives the Raman transition comes from the superposition of the two counter-propagating Raman beams. The optical system used to collimate the Raman beams is presented below, in Section 6.3. Ideally, the Raman beams are Gaussian beams and with a beam waist of 35 mm, the Rayleigh length $z_R \approx 5 \text{ km}$ means that when collimated, the two beams have an almost identical radius of curvature. In this case, the effective field will have a planar wavefront. However, if the beams are not collimated they will have different radii of curvature and their superposition will therefore have a parabolic wavefront, as illustrated in Figure 6.3a. Each Raman pulse will impress a different phase to an atom falling under gravity, leading to a component of the interferometer phase that gives a false acceleration. The effects of this can be shown from a simulation of the Raman wavefront. This is calculated by tracing the rays that correspond to each Raman beam. Rays corresponding to the reflected beam are propagated further making the assumption that the mirror is

perpendicular to the optic axis. Based on the experimental apparatus, the first set of rays propagates 43 mm and the second propagates 129 mm. The wavefront for each beam is calculated by taking the slope of each ray and subtracting from the slope of the central ray. Figure 6.3b shows the effects of poor collimation on the Raman phase for several divergence angles. When the Raman beams are diverging, their different radii of curvature results in a parabolic wavefront, as illustrated in Figure 6.3a. Figure 6.3c shows the corresponding interferometer phase for an atom falling from rest under gravity with a pulse separation of $T = 25$ ms. A divergence angle of 350 μrad results in an interferometer phase contribution of 10 mrad. It should also be noted that since the atoms are launched vertically, they do not travel as far and the interferometer phase error will be smaller than indicated here. Provided that the beams are well-collimated, this effect can be neglected as it is unlikely to be a dominant source of error.

Another point to consider is the possible tilt of the Raman beams. Figure 6.4 presents the configuration when the incoming beam is tilted from the optic axis, but is perfectly retro-reflected. The Raman wavefront is planar, but the Raman axis is tilted from the optic axis. If the optic axis is perpendicular to the axis of gravitational acceleration, then the interferometer will measure a component of gravitational acceleration $g \sin(\theta)$. If we require that this acceleration error is no greater than 100 ng , then this is equivalent to requiring that the tilt of the Raman axis is less than 0.1 μrad . Clearly this level of precision will require the transverse position of the input fibre (see Section 6.3.1) to be exceedingly stable.

If instead the mirror is parallel with the optic axis, the two wavefronts are at an angle to each other, as illustrated in Figure 6.5. In this case the phase difference between the incoming and reflected beams is independent of transverse position and there is no systematic offset in the interferometer phase. However, the wavevectors of the two beams are no longer collinear. The Raman wavevector along the optic axis (\hat{x}) is now

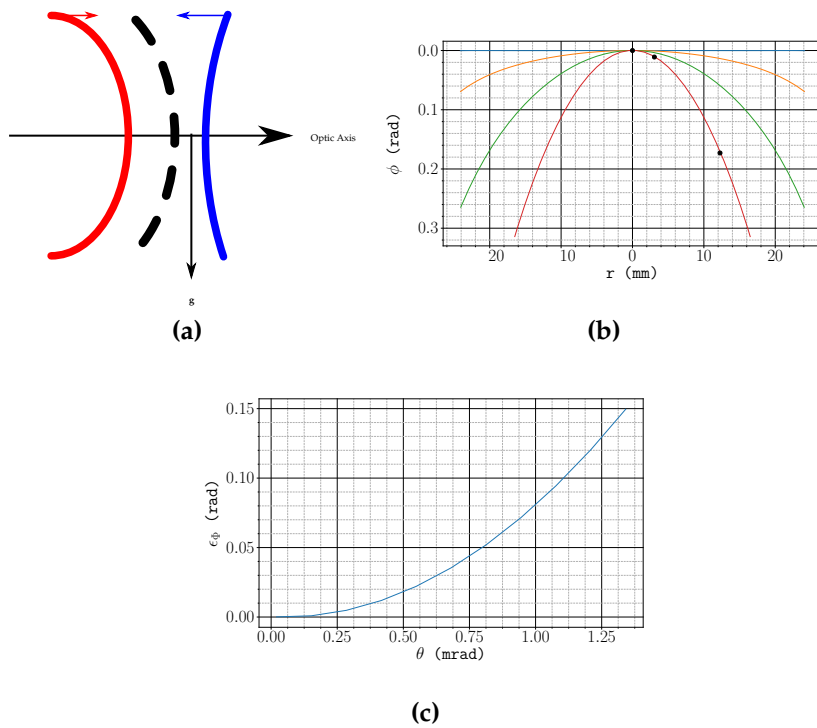


Figure 6.3: Wavefront distortion and interferometer phase error for diverging Raman beams. (a) illustrates the case of diverging Raman beams, where the forward-propagating (shown in red) has a smaller radius of curvature than the backwards-propagating beam (shown in blue). Here, the phase difference varies radially, leading to a parabolic Raman wavefront (shown as a dashed black line). (b) shows the difference in the Raman phase ϕ between the optic axis and a radial displacement r for beam divergence angles of 20 μrad (blue), 400 μrad (orange), 800 μrad (green) and 1.2 mrad (red). The black points indicate the phase shift of each interferometer pulse for an atom falling under gravity and a pulse separation time of 25 ms. (c) shows the resultant interferometer phase error ϵ_ϕ as a function of divergence angle θ for an atom falling under gravity starting at rest on the optic axis. When falling under gravity, a divergence angle of less than 350 μrad results in a phase error of less than 10 mrad which is the value that corresponds to the uncertainty due to sources of phase noise.

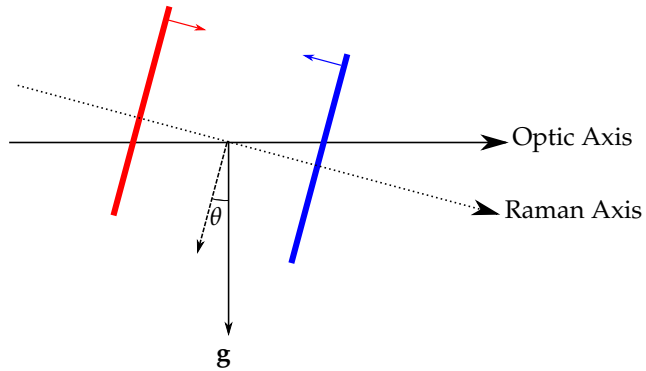


Figure 6.4: Tilted Raman beams with perfect retro-reflection. The Raman wavefront propagates along the Raman axis, indicated by the dotted line. The optic axis is perpendicular to gravity such that the interferometer is sensitive to a component of gravitational acceleration given by $\mathbf{g} \sin(\theta)$.

$\mathbf{k}_{\text{eff}}' = (k_1 - k_2) \cos(\theta) \hat{\mathbf{x}} \approx \mathbf{k}_{\text{eff}}(1 - \frac{1}{2}\theta^2)$. This leads to a calibration error by a factor of $(1 - \frac{1}{2}\theta^2)$. For an acceleration of 0.3 g , a tilt of $\theta = 0.26 \text{ mrad}$ gives an interferometer phase error of 1 mrad . Section 6.4.1 describes a method used to ensure good alignment of the mirror, which renders this error negligible.

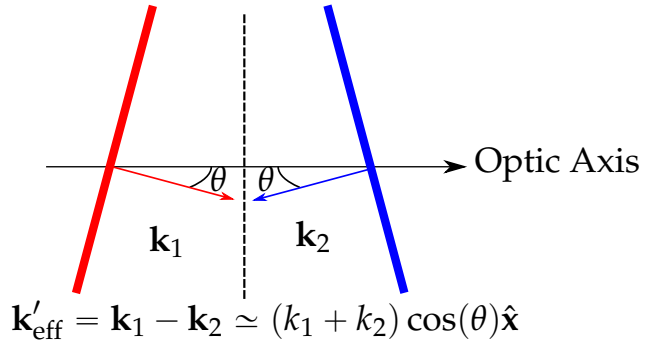


Figure 6.5: Imperfect retro-reflection with a tilted incoming beam. Here, the mirror is perpendicular to the optic axis so that the Raman phase has a planar wavefront (indicated by the dotted line) that travels along that axis. The tilt of the two beams means that their wavevectors are not collinear and the Raman wavevector is $\mathbf{k}_{\text{eff}}' = \mathbf{k}_1 - \mathbf{k}_2 \simeq (\mathbf{k}_1 + \mathbf{k}_2) \cos(\theta) \hat{\mathbf{x}}$, where $\hat{\mathbf{x}}$ is the optic axis.

Random Sources of Phase

The propagation through rough optical elements distorts the wavefronts and introduce a spatially varying component of the Raman phase that is independent of acceleration.

If an atom's trajectory is parallel with the Raman axis, then this phase difference is the same at each laser pulse and makes no contribution to the interferometer phase for that atom. On the other hand, the Raman phase difference can change if the atom moves transverse to the Raman axis and that contributes to the interferometer phase of the atom. If that is the same for all atoms in the cloud then we are once again describing the systematic error discussed immediately above. If it differs for different atoms, then there is a loss of fringe visibility that we estimate now.

For simplicity, let us assume that the interferometer phase has a Gaussian distribution over the cloud with a standard deviation of σ_Φ . Denoting the random interferometer phase as $\delta\phi$, the fringe pattern for a single atom is

$$F = \cos^2(\phi + \delta\phi) \quad (6.3)$$

Following from this, the fringe pattern averaged over the cloud is

$$\langle F \rangle = \frac{1}{\sqrt{2\pi}\sigma_\Phi} \int \cos^2(\phi + \delta\phi) e^{-\delta\phi^2/2\sigma_\Phi^2} d\delta\phi \quad (6.4)$$

$$= \frac{1}{2}(1 + e^{-2\sigma_\Phi^2} \cos(2\phi)) \quad (6.5)$$

This give a fringe contrast of

$$\mathcal{C} = e^{-2\sigma_\Phi^2} \quad (6.6)$$

Figure 6.6 shows the fringe contrast as a function of this random phase. Given the high quality of the optical elements (see Section 6.3), it seems unlikely that the wavefront will wobble by more than $\lambda/50$ over a transverse region of 5 mm. I therefore expect that σ_Φ will not exceed 100 mrad and hence the loss of contrast from this mechanism

will not be large. However, one can see that it is important to use optical components of high quality and that the standard $\lambda/20$ is likely to produce fringes of low contrast.

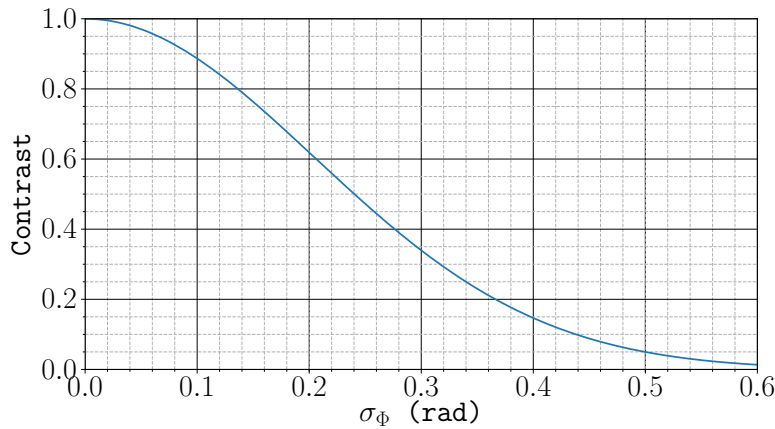


Figure 6.6: Expected contrast as a function of random phase contributions to the interferometer phase. We expect that σ_Φ will not exceed 0.1 rad because of the high-quality optics used.

6.3 Raman Optics

The optical system used to produce the beams for driving Raman transitions, will be referred to as the Raman Optics. For the reasons described in the previous section, this was designed to have good control over the flatness and orientation of the phase fronts of the Raman beams. Principally, the entire optical system was mounted inside the optical chamber so that the Raman light does not pass through any optical viewports before interacting with the atoms. This avoids the phase and polarisation distortions that are typically introduced by passing light through a vacuum window.

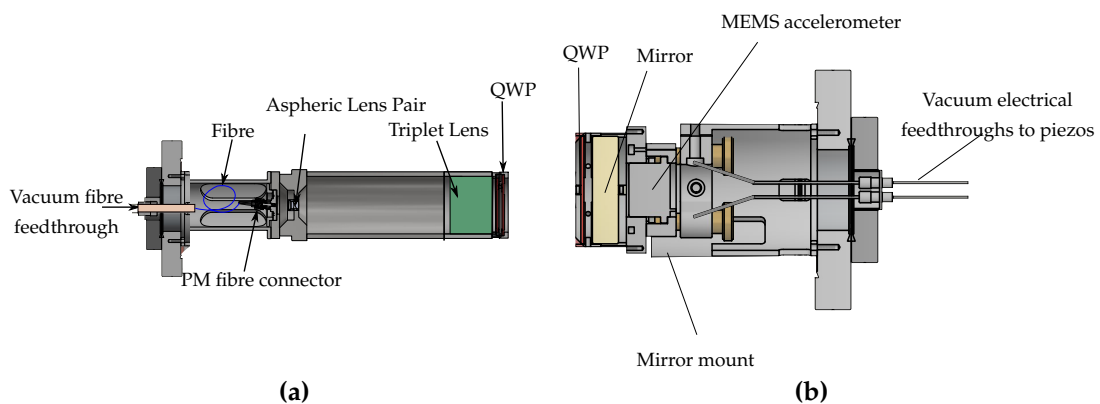


Figure 6.7: Diagrams of the components used in the Raman optical assemblies, not drawn to scale. (a) shows the collimator setup. Light is coupled into the chamber using a UHV fibre feedthrough. A pair of aspheric lenses is used to increase the divergence angle of the fibre output, before the light is collimated by a triplet lens. Finally, a quarter-wave plate is aligned so that it circularly polarises both collimated light fields. (b) illustrates the other half of the setup, which is used to retro-reflect the light. A second quarter-wave plate is used so that the reflected beams have the reversed circular polarisation. A MEMS accelerometer is mounted on the back of the mirror to measure vibrations. These components are all mounted on a piezo-controlled mirror mount whose tilt can be controlled from outside the vacuum chamber.

6.3.1 Component Overview

Figure 6.7a presents a diagram of the components used to send Raman light into the chamber and produce a collimated beam in the centre of the chamber. The light is coupled into the chamber using a UHV compatible PM fibre, manufactured by Diamond photonics. This is a kapton-coated PM-780 HP fibre that is bonded on one end to a DN16 flange using an epoxy resin. The external side of this flange has an FC/APC connector for receiving the fibre input from the laser system. Inside the chamber, the output of the fibre plugs into to an FC/APC fibre plate. This is clamped between a piece which bolts onto the inside of a DN63 flange and another stainless steel plate which bolts onto the rest of the optics assembly. Fine adjustment of the position of the fibre along the optic axis is achieved using shim plates with a thickness ranging from 200–300 μm . The fibre plate is free to rotate so that the fibre is correctly orientated with respect to a QWP at the output of the collimator. This QWP is manufactured by Light Machinery, and is described further in Section 6.4. When the fibre is correctly orientated, the slow axis of the fibre is at 45° to the slow axis of the waveplate and the two Raman light fields are orthogonally circularly polarised.

The original design for the collimator had only the triplet lens, as a system of three lenses is capable of correcting for the five types of Seidel aberrations that distort rays of monochromatic light. This was designed and manufactured by IC Optical Systems to deliver a collimated wavefront quality of $\lambda/100$ with a waist size of around 35 mm so that the visibility of the interferometer fringes would not be limited by the effects of intensity gradients across the atoms. Unfortunately, the triplet was designed with an incorrect Numerical Aperture (NA). With a focal length of 123.4 mm and a diameter of 50 mm, the triplet lens has a NA of 0.194. However, the nominal NA for PM780-HP fibre used in the UHV compatible PM fibre is 0.12. Consequently, the light from this fibre did not fill the NA of the triplet lens and produced a beam with a waist of

13 mm. To address this issue, a pair of aspheric lenses was included to increase the divergence angle of light from the fibre. These are manufactured by Thorlabs and have a focal length of 4.51 mm (352230-B) and 15.29 mm (352260-B), respectively, to give a magnification of 3.39. These lenses are designed to give a diffraction-limited performance when collimating or focusing a beam from a fibre output. Their specified surface quality is 40-20 scratch-dig, which is typical of moderate-quality optical elements. However, it was found that defects in the surfaces of these lenses produced an irregular intensity profile in the collimated beam. This inhomogeneity was subsequently found to significantly dephase the atoms during a Raman transition, which is discussed in Section 7.4.4.

6.3.2 Measuring the Beam Width

To measure the waist of the beam, the scattered light from a flat surface was imaged using a CCD camera. Because the beam is clipped, the profile is not Gaussian, but it could be fitted to a symmetrical quadratic having the same curvature as a Gaussian near its centre. A Taylor expansion of the Gaussian to third order gives

$$\begin{aligned} I(x) &= Ae^{-\frac{2(x-x_0)^2}{w^2}} \\ &\approx A \left(1 - \frac{2(x-x_0)^2}{w^2} \right) + \mathcal{O}(x^4) \end{aligned} \quad (6.7)$$

A typical intensity profile along the horizontal and vertical camera axes is shown in Figure 6.8a. A threshold intensity value excludes contributions to the fit from pixels outside of the spatial extent of the beam. The "waist" parameter w was estimated using a linear least-squares fit of the intensity profile. Measurements were made of w at various distances from the triplet lens ranging from 0 to 1 m with the results plotted in Figure 6.8b. This shows that the beam is not perfectly collimated, but the fit shown

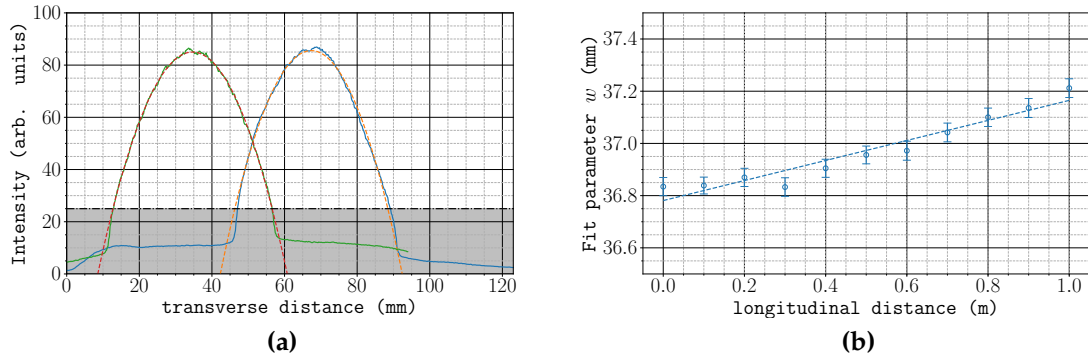


Figure 6.8: (a) shows the intensity profile along each axis, with the fitted parabola. The dot-dashed line is a threshold intensity value, which excludes pixels from outside the spatial extent of the beam. (b) shows the Raman beam waist measured over a distance of 1 m. The dashed line is a best-fit line which gives a gradient of $0.40(3) \text{ mm m}^{-1}$, corresponding to a divergence angle of $0.40(3) \text{ mrad}$.

by the line in Figure 6.8b gives a divergence angle of only $0.40(3) \text{ mrad}$. For an atom starting at rest and falling under gravity that produces an interferometer phase error of only $10(2) \text{ nrad}$. This is sufficiently small that the collimator was installed without further adjustment.

6.4 Retro-Reflection Assembly

The Raman transitions used in the interferometer need to be driven by counter-propagating light fields to give a large momentum transfer of $2\hbar k$ to the atoms. The two beams enter from the same fibre input, with polarisations σ^+ and σ^- , and a mirror is used to retro-reflect them. The retro-reflection assembly includes a QWP to reverse the circular polarisation of each light beam. The polarisation then ensures that the Raman transition is driven by counter-propagating beams - either $\sigma^+ - \sigma^+$ or $\sigma^- - \sigma^-$. This retro-reflection part of the optical train is the most crucial for avoiding transverse spatial variation in the Raman phase.

The mirror is also manufactured by Light Machinery, and the QWP is made to the same specifications as the one that circularly polarises the incoming beams. During the manufacturing process, the waveplates and mirror were polished to reduce irregularities in the thickness of each QWP and the surface of the mirror. Figure 6.9 shows the variation in the thickness of the waveplate in front of the triplet lens, measured by Light Machinery using a white light interferometer. This has a standard deviation of 4.62 nm and corresponds a standard deviation of the optical path length of $8.6 \times 10^{-3}\lambda$. The QWP and mirror are fixed onto the front plate of a UHV compatible MDI-HS

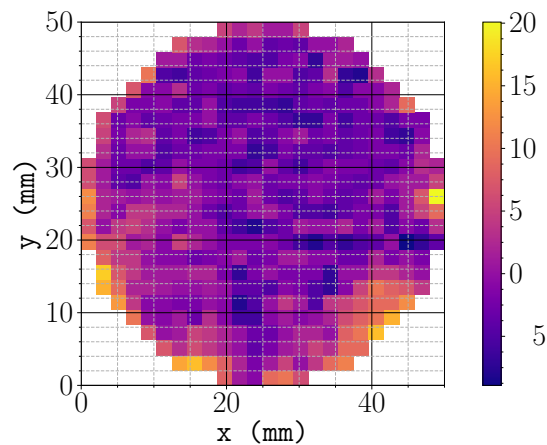


Figure 6.9: Thickness of the first QWP, measured by a white light interferometer. The value is given in nm as a difference from the mean thickness. The standard deviation of this thickness is 4.62 nm and a peak-to-valley (PV) of need number here. Equivalent surface data for the other QWP and mirror were not provided by Light Machinery, but had a PV thickness variation of 19 nm and 9 nm respectively.

mirror mount, manufactured by Radiant dye. The horizontal and vertical tilts of the mirror can be adjusted using two thumbscrew actuators which cause the front plate to tip. This mount is designed for high stability, but of course the alignment will still drift over time. To avoid the need to periodically open the chamber to realign the mirror, a piezo-electric stack is placed between each actuator and the front plate so that the tilt of the mirror can be adjusted externally. Each piezo-stack is connected to a high-voltage feedthrough, so that their length (and hence mirror tilt) can be finely

adjusted by controlling the voltage applied across them. A control voltage ranging between 0–10 V is amplified by a controller to give an applied voltage across the piezo stack between -10–150 V. This corresponds to a travel range of 23 μm .

6.4.1 In-Situ Alignment and Optimisation

After mounting the Raman optical system inside the chamber, the mirror had to be aligned to retro-reflect the light. When the mirror is close to perpendicular to the light's wavevector, some of the power in the reflected beam couples back into the fibre. In principle, this power is maximised when the mirror is exactly perpendicular so maximising this power is a useful technique to align the mirror. A 99:1 fibre splitter was used to couple light into the chamber, which provided a means to measure the back-reflected power without needing any free-space optics. This was set up so that 99% of the incoming light entered the chamber, with the other 1% coupled into the corresponding output port. The beam-splitter acts reversibly so 1% of the back-reflected light which couples into vacuum fibre exits the fibre-splitter on the other input port. By splitting off only a small amount of power, most of the light enters the chamber and is thus useful for driving Raman transitions. The back-reflected power can be used to continuously monitor the alignment of the mirror.

Our sponsors, the dstl, want the accelerometer to have an automated start-up procedure, so an automatic routine was devised to align the retro-reflector. This was carried out using a pair of bipolar stepper motors to adjust each thumbscrew. The revolution of these motors was controlled using an Arduino microcontroller, which communicated with the computer using a serial interface. The motors rotated by 0.9deg/step, which corresponds to a tilt of the mirror by 18.1 μrad .

Using this method, the mirror mount was aligned so that the maximum of the back-reflected power was reachable with the piezo stacks. Of course, it was foreseeable that the mirror would need to be periodically realigned, which would require another systematic iteration through the voltages applied to each piezo stack. Given that this search was quite time consuming, it was not a practical way to maintain alignment. To improve upon this, an optimisation method using the Nelder-Mead simplex algorithm [58] was implemented. This method is suitable for optimising multidimensional functions and has been used to demonstrate the automatic alignment of a fibre with up to 6 degrees of freedom [59].

The Nelder-Mead algorithm aims to optimise the value of an objective function (in this instance, the optical power measured as a voltage by a photodiode) by sampling the function at various locations. For n parameters, a set of $n - 1$ points distributed randomly across the parameter space are chosen as the initial simplex. These are sorted in decreasing order of the value of the objective function and the algorithm proceeds by performing geometric transformations on this simplex, by sequentially reflecting, expanding and contracting it. Each step starts with a reflection about the line between the two greatest values. The coordinates of the simplex are updated if the function has a greater value at the location given by one of these transformations, until the algorithm converges on a maximum value. As with many optimisation algorithms, the Nelder-Mead method has the potential to converge on a local optimum, but this is alleviated by expanding the simplex to look for more optimal values. The termination of the algorithm was decided by using the standard deviation of the last 5 values. Empirically, it was found that terminating when the standard deviation was less than $10 \mu\text{V}$ resulted in stable performance of the algorithm, even when the signal-to-noise ratio of the measured voltage was poor. An example of this algorithm aligning the mirror mount is presented in Figure 6.10. To verify that the converged value was optimal, a systematic scan of the piezo stack control voltages in the region around

this value was also carried out. In this case, the algorithm converged on a local maximum, that was very close to the global maximum and greatly enhanced the coupling efficiency of the reflected light back into the fibre. The difference in the piezo control voltages between the local and global maxima corresponded to a tilt of the mirror mount of less than $13\text{ }\mu\text{rad}$. This scheme was thus selected as the one to incorporate into the start-up routine for the accelerometer.

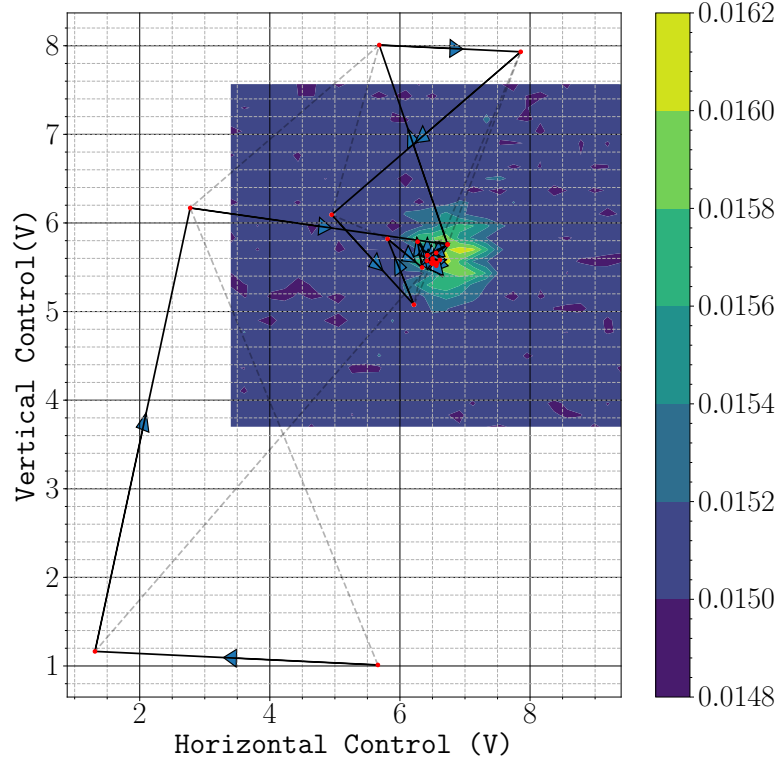


Figure 6.10: Automatic mirror alignment using the Nelder-Mead simplex algorithm. A sequence of geometric transformations on the initial simplex are used to converge on the optimum point, where the back-reflected power is maximised. The shaded lines indicate the simplex bounded by the three co-ordinates at each iteration. A raster scan of the piezo control voltages close to the optimum is also plotted. The irregular shape of the measured power is a result of a hysteresis effect when the horizontal control voltage was changed from its maximum value to the minimum.

6.4.2 The Mechanical Accelerometer

The interferometer phase is proportional to the acceleration of the retro-reflecting mirror relative to the freely-falling atoms. However, the sinusoidal interferometer signal is periodic with period $\Delta a = \frac{\pi}{k_{\text{eff}} T^2}$, so we need to know the order number of the fringe before the acceleration can be deduced from the signal. For this reason, a mechanical (MEMS) accelerometer is mounted on the back of the retro-reflecting mirror to determine the acceleration up to the fringe spacing and the interferometer measures the acceleration more precisely. The MEMS accelerometer is also sensitive to vibrations of the retro-reflecting mirror and can be used to characterise the vibration-induced phase noise. This is discussed in more detail in Section 7.6.2. This technique enables accurate measurements of acceleration in high-noise environments and has been used to measure the acceleration due to gravity at the centre of Paris [19] and in parabolic aircraft flights [12, 60].

The accelerometer is a navigation-grade AI-Q-2010 manufactured by *Innalabs*. This particular device was chosen for its low noise specification of $<7 \mu\text{g}$ in the 0-100 Hz bandwidth. For a pulse separation $T = 25 \text{ ms}$, the fringe spacing is $64 \mu\text{g}$ so it is sensitive enough to measure the acceleration to within one fringe. A schematic of this device is shown in Figure 6.11. It operates using a quartz pendulum which is free to move about one axis [61, 62]. Under an acceleration, the deflection of the pendulum is capacitively detected. A servo loop circuit drives a current through the coils to restore the position of the pendulum. This current is directly proportional to the acceleration of the pendulum. This model has a nominal scale factor of $1.235\,976 \text{ mA g}^{-1}$. The acceleration is measured using a load resistance of $6 \text{ k}\Omega$ to give an output voltage of 7.56 V g^{-1} .

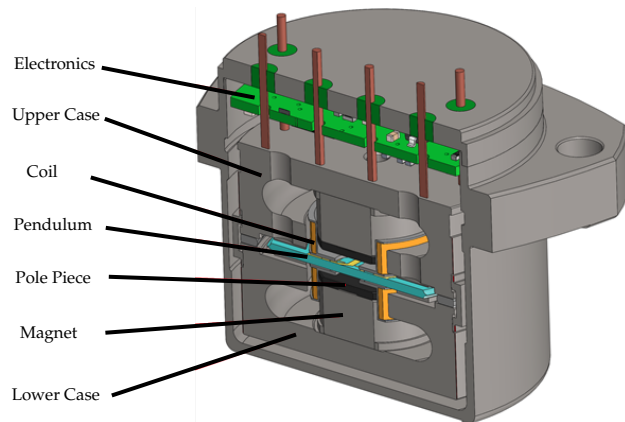


Figure 6.11: Cross-section of the Innalabs AI-Q-2010 accelerometer.

6.5 Conclusion

This chapter has motivated the need for low wavefront distortions to achieve sensitive measurements of acceleration, particularly when there is significant transverse motion across the Raman beam. Following this, the in-vacuum optical system was introduced. This helps to reduce the effect of wavefront distortions by not transmitting the beam through an optical viewport. Finally, the retro-reflection assembly used to produce the counter-propagating beams has been presented.

Chapter 7

Acceleration-Sensitive Interference

7.1 Chapter Outline

This chapter describes the aspects of the project aimed at observing matter-wave interference in ^{87}Rb and its subsequent characterisation. The laser system used to drive the necessary Raman transitions is presented in Section 7.2. This is followed by a discussion of the methods used to detect the population in each internal state in Section 7.3. The Raman transition spectrum and dynamics of the atoms during each Raman pulse are discussed in Section 7.4. This chapter continues with an overview of identified sources of noise and their impact on the interferometer's sensitivity to accelerations in Section 7.5. Finally, a presentation of observed interference and an analysis of its sensitivity to accelerations is given in Section 7.6.

7.2 The M-Squared Laser System

This section describes the laser system manufactured by *M-Squared Lasers*, which is used to drive Raman transitions. A Phase-Locked Loop (PLL) controls the phase difference of two Ti:Sapphire lasers by comparing the beat note with a stable local oscillator. An overview of the laser system can be found in Section 7.2.1, which includes the techniques used to externally communicate with the laser's ICE-BLOC control modules. The control of the frequency and phase-lock is then described in Section 7.2.2. Finally, this section concludes in Section 7.2.3 with a description of the DCS module which is used to control the amplitude, frequency and phase of the Raman laser beat-note during the experiment.

7.2.1 Laser System Overview

The Raman laser system contains two SolsTiS lasers, each generating 780 nm light by pumping a Ti:Sapphire crystal housed inside a resonator. The output light is frequency-stabilised using piezo-electric stacks to adjust the resonator length [66]. A schematic diagram of this laser system is given in Figure 7.1. Each laser is pumped using a 12 W *Lighthouse Photonics* Sprout laser at 532 nm. One SolsTiS acts as the master frequency locked to an absorption feature in the saturated absorption spectrum of ^{87}Rb . The second is slaved to this using a phase-locked loop to keep their beat frequency constant. Since the two beams are orthogonally polarised, they are mixed using a PBS, so that they travel along the same optical path. Two AOMs control the output power.

The system contains 4 ICE-BLOC modules which implement various types of control. The first two (one for each Solstis) are used to stabilise the output power of each laser by feeding back to the corresponding Sprout laser. They are also used to coarsely adjust the output frequency, which is measured using a *HighFinesse* wavemeter. The third is

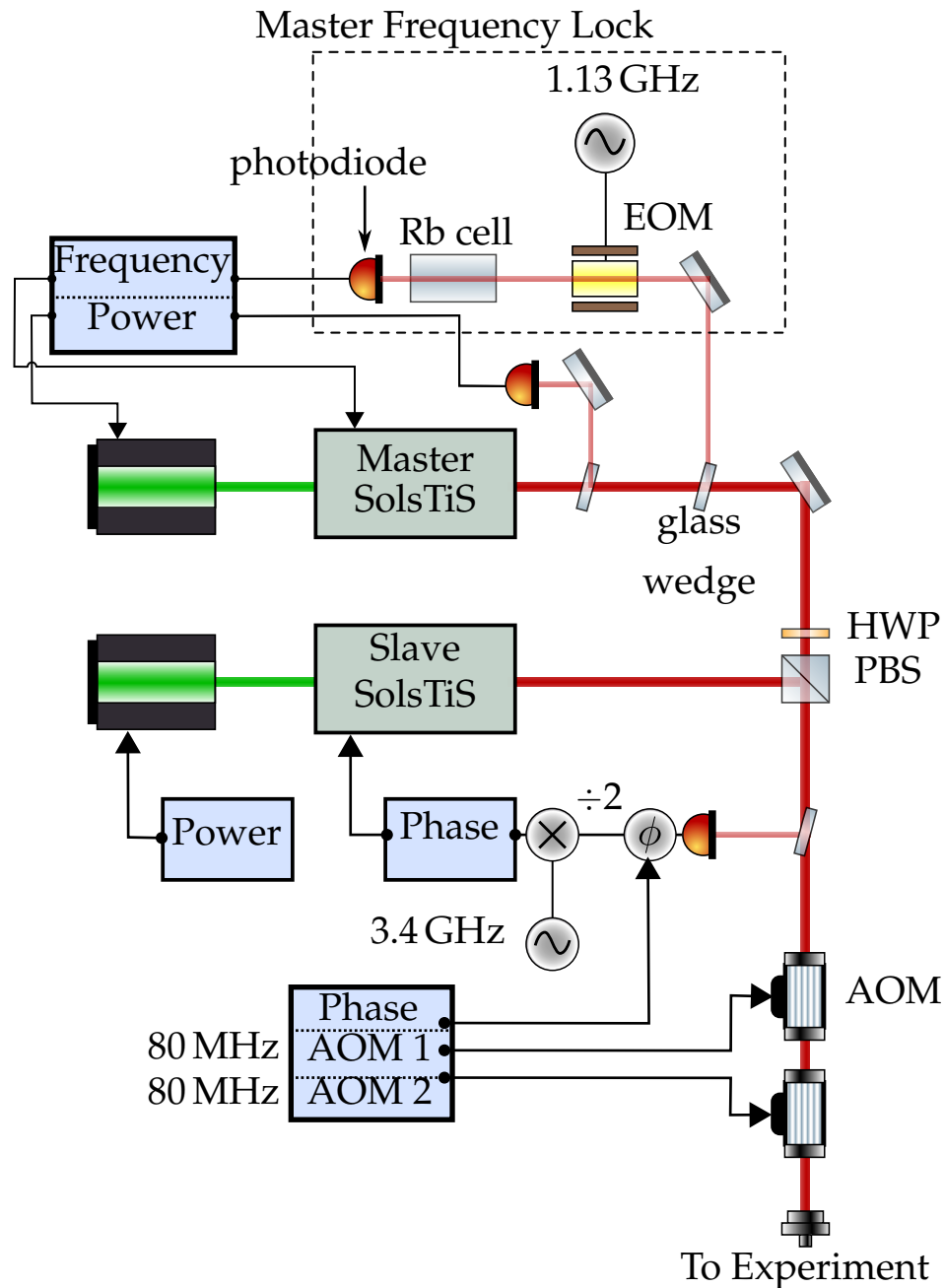


Figure 7.1: Schematic Diagram of the M-Squared laser system. Two SolsTiS lasers provide the two Raman frequencies, which are fibre coupled onto the orthogonal axes of a PM fibre. Control of the power, frequency and phase as required to drive and control the Raman transitions is handled by the four ICE-BLOC modules indicated in blue. Further detail of this control is given in the text.

used for the PLL and feeds-back onto the slave laser to control both the frequency and phase of the optical beat-note between the two lasers. The final ICE-BLOC, referred to as the DCS module, is used to control the lasers in real-time during the experiment.

External ICE-BLOC Control

The ICE-BLOC modules are able to communicate with each other using an Ethernet hub. Another computer connected to this network is able to control them by accessing a web page that each module hosts. These web pages control the ICE-BLOCs by sending structured JSON messages. This graphical interface can be bypassed by directly communicating these messages. This is done using MOTMaster so that various parameters, such as the frequency and phase of the Raman beat-note, can be automatically varied between experiment cycles.

7.2.2 Frequency and Phase Control

Master Lock

The frequency of the master laser is stabilised using saturated absorption spectroscopy in a Rubidium vapour cell. Part of the beam is picked off and modulated by an EOM. The positive frequency sideband is used to lock the master laser to the 2,3 crossover feature. In effect, this means that the modulation frequency of the EOM sets the one-photon detuning of the Raman transition. The modulation frequency is set so that the master laser frequency is 1.13 GHz below the $|F = 2\rangle \rightarrow |F' = 3\rangle$ transition. This frequency is chosen because the light shift of the clock transition vanishes there provided the two Raman beams have the right intensity ratio as discussed in Section 7.4.2. This ensures that the resonant frequency is independent of variations in the over-all intensity of the Raman beams.

Frequency and Phase Lock

The optical beat-note between the two lasers is measured using a fast photodiode. The signal from this is used in a PLL to fix the relative phase between the two lasers. A frequency divider halves the frequency of the signal before comparing it to a VCO of around 3.4 GHz. This creates an error signal which used to control both the frequency and phase of the beat-note by feeding back to the slave laser Solstis. The relative phase between the two lasers is adjusted using an analogue phase shifter and the frequency difference is controlled by tuning the VCO frequency.

The beat-frequency of the Raman lasers can be chirped by triggering a ramp of the control voltage to the VCO. For chirp rates of lower than 24 MHz s^{-1} , the phase-lock is able to keep the beat-note phase-coherent during the chirp.

7.2.3 The DCS Module

The DCS module is used to control the output of the lasers during the experiment. It uses an on-board DDS to synthesise the 80 MHz driving frequencies for each AOM. The majority of the control is done using an Field-Programmable Gate Array (FPGA) that synthesises a timed sequence of analogue and digital voltage waveforms. An example of a sequence created using the DCS web interface is shown in Figure 7.2. The sequence is segmented into individual steps and each channel can be separately configured, much like the MOTMaster user interface.

This module is used to control the amplitude, frequency and phase of each Raman pulse. The pulse amplitude is shaped using an analogue voltage to control the power of the RF frequency. The voltage output has been calibrated so that the pulse can be shaped to produce a square, Gaussian or Blackman amplitude envelope. A frequency

chirp of the beat-note is optionally triggered by sending a digital pulse to the PLL ICE-BLOC.

The synthesiser can be configured to run continuously, or to wait at a chosen timestep for an external trigger. It can also iterate through a set number of parameters, such as timestep duration or phase shift by re-building the sequence after each cycle.

7.3 Atom Detection

This section describes the methods used to measure the number of atoms in each hyperfine ground state and infer the interferometer phase. It begins with a presentation the optical setup used to collect fluorescent light on a photodiode in Section 7.3.1. The scheme used to detect the atoms by driving σ^+ transitions is then described in Section 7.3.1. This concludes with a discussion on converting the measured photodiode signals into atom number and interferometer phase in Section 7.3.3.

7.3.1 Optical Setup

Our aim in this device is to reach the standard quantum noise limit, which comes from the quantum projection noise. Expressed as a fractional accuracy this is given approximately by $N^{-1/2}$ [67], where N is the number of atoms detected. The CCD used initially was not sensitive enough for this as there was a significant amount of noise in reading out the charge collected at each pixel. Instead, a more sensitive photodiode is used to detect the atoms. With a suitably high bandwidth, the readout time is much faster than the CCD as well, so that the atoms can be detected well before they fall out of the field of view.

| DCS | | | | | | | | | | | |
|------------------|----------|-----------|---------------|---------------|-------------------|---------------|-------------------|---------------|---------------|---------------|---------------|
| I/O Sequencer | FEP: 0 | Status: 0 | Setup | Wait | State Selection 1 | Delay | State Selection 2 | Delay | Dark 1 | Pulse 1 | Dark 2 |
| Instruction List | Index: 0 | 0.1 ms | 0 ms | 64 µs | 1 ms | 64 µs | 1 ms | 25 ms | 8 µs | 25 ms | 8 µs |
| User Function | Output | Live | | | | | | | | | |
| Phase Control | DDS All | - | Clear & Reset | Clear & Reset | Blackman | Clear & Reset | Blackman | Clear & Reset | Clear & Reset | Clear & Reset | Clear & Reset |
| AOM Master | VGA1 | - | -9.5 dB | -5.5 dB | 80 MHz | -9.5 dB | 80 MHz | -9.5 dB | 22 dB | -5.5 dB | 22 dB |
| | DDS1 | 80MHz | - | 80 MHz | 80 MHz | 80 MHz | 80 MHz | 80 MHz | 80 MHz | 80 MHz | 80 MHz |
| AOM X-Axis | VGA2 | - | -9.5 dB | -5.5 dB | 22 dB | -9.5 dB | 22 dB | -9.5 dB | 22 dB | -5.5 dB | 22 dB |
| | DDS2 | 80MHz | - | 80 MHz | 80 MHz | 80 MHz | 80 MHz | 80 MHz | 80 MHz | 80 MHz | 80 MHz |
| AOM Y-Axis | VGA3 | - | -9.5 dB | -5.5 dB | -9.5 dB | -9.5 dB | -9.5 dB | -9.5 dB | -9.5 dB | -9.5 dB | -9.5 dB |
| | DDS3 | 80MHz | - | 80 MHz | 80 MHz | 80 MHz | 80 MHz | 80 MHz | 80 MHz | 80 MHz | 80 MHz |
| AOM Z-Axis | VGA4 | - | -9.5 dB | -5.5 dB | -9.5 dB | -9.5 dB | -9.5 dB | -9.5 dB | -9.5 dB | -9.5 dB | -9.5 dB |
| | DDS4 | 80MHz | - | 80 MHz | 80 MHz | 80 MHz | 80 MHz | 80 MHz | 80 MHz | 80 MHz | 80 MHz |
| Sequence Trigger | DIO5 | Off | | | | | | | | | |
| X-Axis Running | DIO6 | Off | Off | Off | Off | Off | On | On | On | On | Off |
| Y-Axis Running | DIO7 | Off | Off | Off | Off | Off | Off | Off | Off | Off | Off |
| Z-Axis Running | DIO8 | Off | Off | Off | Off | Off | Off | Off | Off | Off | Off |
| Chirp Control | DIO9 | Off | Off | Off | Off | Off | Off | Off | Off | Off | Off |
| RF Switch Master | DIO18 | On | Off | Off | On | Off | On | Off | Off | Off | Off |
| RF Switch X | DIO19 | Off | On | Off | Off | Off | Off | Off | Off | Off | Off |
| RF Switch Y | DIO20 | On | Off | Off | Off | Off | Off | Off | Off | Off | Off |
| RF Switch Z | DIO21 | Off | Off | Off | Off | Off | Off | Off | Off | Off | Off |
| Phase Shift | AN08 | 0.00 rad | 0 rad | 0 rad | 0 rad | 0 rad | 0 rad | 3.8 rad | 3.8 rad | 0 rad | 0 rad |

Figure 7.2: DCS module user interface. The sequence is synthesised from individual steps. The parameters of each Raman laser pulse can be configured independently.

A diagram of the setup used to detect the atoms is given in Figure 7.3. It is a triplet system which uses lenses with focal lengths 150 mm, 75 mm and 60 mm, with the 150 mm lens closest to the atoms and the 60 mm lens closest to the photodiode. A ray-tracing simulation of the optical system indicates spherical aberrations on the image. This is caused by the third lens, which was added to shorten the back focal length. This has the effect of limiting the resolution of the image and leads to a reduction in the intensity of the light collected from atoms away from the front focus of the lens. This problem was alleviated by ensuring that the optical system was focused on the atoms during detection. The front lens has a diameter of 50.4 mm, so the solid angle subtended by the optics is $4\pi \times 7.1 \times 10^{-3} \text{ sr}$.

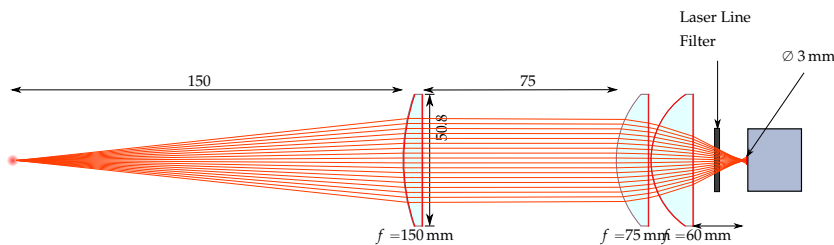


Figure 7.3: Optical setup for photodiode detection. A triplet lens system focuses light from radiated from the atoms onto a photodiode. This is mounted using a translation stage to position the photodiode at the back focal point.

Photodiode Calibration

The photodiode used is a *Femto LCA-S-400K-SI*, which has a trans-impedance amplifier with a bandwidth of 400 kHz and a photo-sensitive area with a diameter of 3 mm. The scaling factor from incident optical power to output voltage was measured as $1.84 \times 10^6 \text{ V W}^{-1}$.

7.3.2 Detection using σ^+ transitions

The atoms are detected using resonance fluorescence from the two vertically aligned MOT beams in the presence of a vertical magnetic field. For the MOT and molasses these are polarised σ^+ and σ^- , but for this detection step, we use a liquid-crystal HWP to give both beams σ^+ polarisation. This causes the atoms to be optically pumped into $|2,2\rangle$ and cycle on the $|2,2\rangle \rightarrow |3,3\rangle$ transition, which allows the atoms to scatter many photons with minimum probability of unwanted optical pumping into $|F = 1\rangle$.

Figure 7.4 shows the setup used to invert the polarisation of one MOT beam prior to detection. The liquid-crystal waveplate is an electro-optical device whose birefringence changes when an ac voltage is applied across it. The waveplate is placed at the output of the downward-propagating (\vec{z}_-) collimator. The liquid-crystal waveplate is triggered to rotate the incoming linearly polarised light by $\pi/2$ rad.

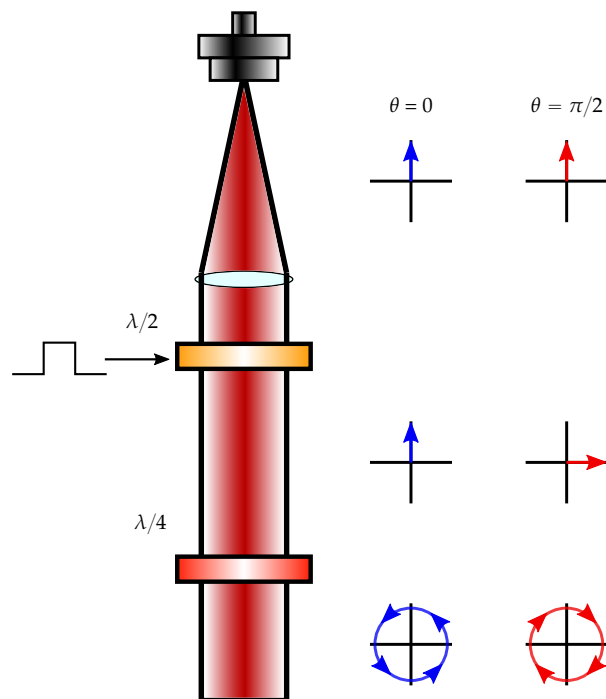


Figure 7.4: Scheme to invert beam polarisation. In the MOT loading phase of the experiment, the liquid crystal HWP is oriented to give a right-hand circular polarised beam shown in blue. Prior to detection, a digital pulse triggers a re-orientation of its slow axis. This results in a left-hand circular polarised beam, shown in red.

Detection Sequence

The sequence used to detect the atoms is shown in Figure 7.5. Shortly before the sequence starts, the bias field is aligned to the \bar{z} axis and the liquid-crystal waveplate is triggered to change the handedness of the \bar{z}_- beam. The cooling laser frequency is set so it is detuned by $\delta_D = 3 \text{ MHz}$ below the $|F = 2\rangle \rightarrow |F' = 3\rangle$ transition and the repump laser is set to resonance with the $|F = 1\rangle \rightarrow |F' = 2\rangle$ transition. This creates an optical molasses which avoids heating the atoms so that they remain in the detection volume for a longer period of time. The intensity of the light is reduced to around $3I_{\text{sat}}$. As shown below, this intensity was empirically found to minimise the variance in output voltage. The acquisition of the photodiode voltage is triggered to start at the first Dwell time. The cooling light is first switched on without any repump light so that only atoms in $|F = 2\rangle$ scatter light. After this, the repump is switched on, so that atoms in $|F = 1\rangle$ are optically pumped into $|F = 2\rangle$ and all the atoms scatter light. Now the fluorescence measures the total number of atoms N . This repump light is a sideband of the cooling laser, so the total output is increased to ensure that the intensity of the cooling light remains constant. Each detection step lasts $250 \mu\text{s}$, but the first $50 \mu\text{s}$ is discarded to allow time for the intensity to stabilise and for optical pumping into $|F = 2\rangle$. All the atoms are then blown away by switching off one of the detection beams before the sequence is repeated to collect a background signal.

Maximum Detection Time

As the atoms scatter light during detection, the cloud will be heated and expand due to the momentum exchanged from absorption and spontaneous emission. The atoms are only cooled along the axis of the detection beams, so the heating rate is greatest along the other two axes. It is necessary to ensure that the heating rate is low enough that the atoms remain within the detection beam for the entire detection time. A requirement

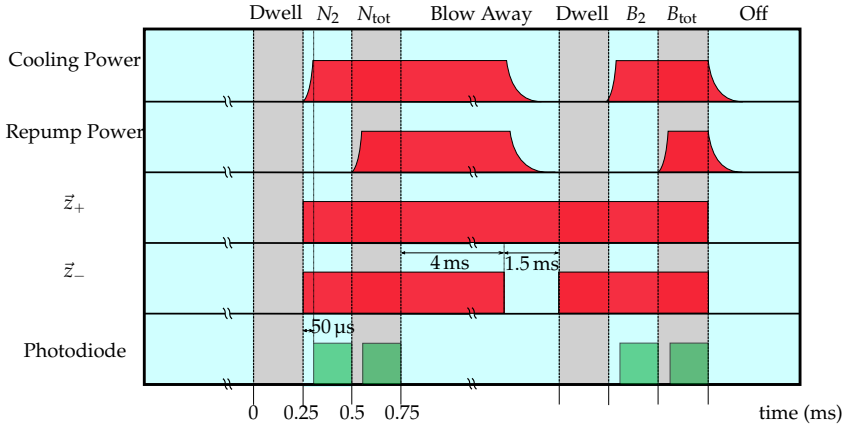


Figure 7.5: Timing diagram for state detection. Atoms in $|F = 2\rangle$ are detected first, then repump light pumps the $|F = 1\rangle$ atoms into $|F = 2\rangle$ so they are detected as well. A background light measurement follows the measurement of the atom numbers.

on the maximum detection time can be obtained as follows. The momentum of an atom scattering photons follows a random walk, so if the cloud has a Gaussian spatial distribution with an initial width of σ_0 , the width at a later time of is given by

$$\sigma_x^2(t) = \sigma_0^2 + \frac{2n_p v_r^2 t^2}{3} \quad (7.1)$$

where $v_r = \frac{\hbar k}{m_{\text{rb}}} = 6 \text{ mm s}^{-1}$ is the recoil velocity and n_p is the number of photons scattered. The factor of $2/3$ is because only the transverse component of the recoil is relevant here. To remain within the detection region, the width of the cloud must be smaller than the detection beam waist w , so the detection time must satisfy

$$t_D \ll \sqrt{\frac{3(w^2 - \sigma_0^2)}{2(nv_r^2)}} \quad (7.2)$$

For a beam waist of 7.5 mm, initial cloud size of 5 mm and a maximum scattering rate of $2 \times 10^7 \text{ s}^{-1}$ the detection time must be much less than 4.7 ms. This inequality is amply satisfied by our detection time of 100 μs .

Detection Intensity

The intensity for detection was chosen by varying the total power in the detection beams and recording the photodiode voltage for a fixed detection time of 200 µs. Figure 7.6 shows the average voltage measured when detecting atoms in the $|F = 2\rangle$ state as the intensity of the light increases. The saturation parameter s is inferred from the control voltage used to control the light through the AOM at the output of the μ Quans laser (see Figure 4.13). This value assumes that the atoms are at the peak intensity of the MOT beams. However, by the time the atoms are detected, they have moved away from the region of peak intensity, so the intensity on the atoms is smaller than indicated. A fit parameter b is introduced to account for this reduction. This is estimated using a non-linear least squares fit to the function

$$V = a \frac{bs}{1 + bs + 4(\delta_D/\Gamma)^2} \quad (7.3)$$

which for $\delta_D = 3\text{ MHz}$ gives a value of $b = 0.83(11)$ and . Figure 7.7 shows the voltage recorded by the photodiode during detection for a range of detection intensities. We can see that there is evidence of a de-population of the $|F = 2\rangle$ state, which is not expected given that the detection beams are polarised to both drive the σ^+ transition. However, as previously seen in Section 5.3.2, we know that the magnetic field is not perfectly aligned with the axis of the \vec{z} MOT beams. It is likely that a small component of the light is driving off-resonant transitions to $|F' = 2\rangle$ and de-populating the $|F = 2\rangle$ state for the same reason that we do not see a complete population of the $|F = 1, 0\rangle$ state. The photodiode signal is most stable at an intensity of $3I_{\text{sat}}$, where approximately 5% of the population is pumped out of $|F = 2\rangle$ ¹

¹It is surprising that there is a fast decay of the $|F = 2\rangle$ population at low intensities. This is due to the light generated by the μ Quans laser, but the exact cause is yet to be determined. After changing the laser used to detect the atoms, this fast decay was no longer observed.

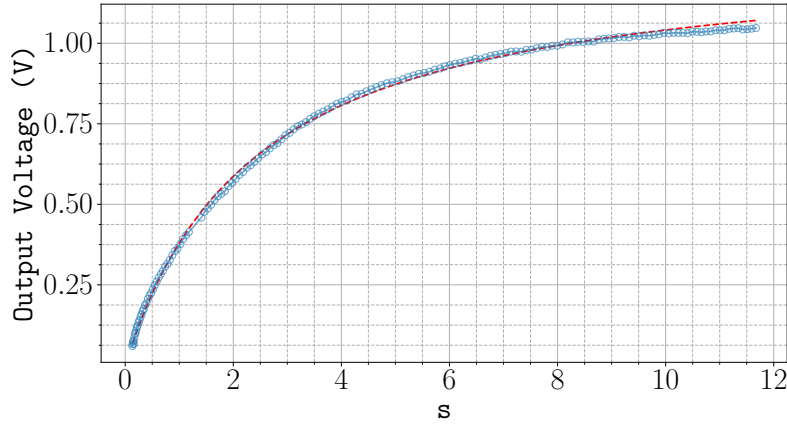


Figure 7.6: Photodiode output voltage for increasing detection beam intensity. The red dashed line indicates a fit to equation (7.3) to estimate the scaling factor for the saturation parameter s .

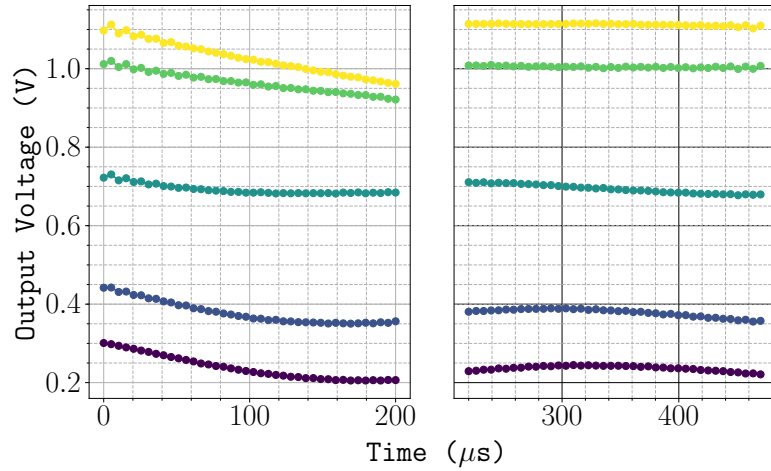


Figure 7.7: Photodiode voltage during atom detection. The left-hand plot shows the signal measured when detecting atoms in $|F = 2\rangle$. The right-hand plot shows the signal after turning on light to drive atoms from $|F = 1\rangle$. In both plots, the signal was measured for $200\ \mu\text{s}$. The saturation parameters are $s = 0.5, 1, 3, 7, 10$ in order from purple to yellow. There is a noticeable decay of the population in $|F = 2\rangle$, which is expected at high intensities. An decay of the signal at low intensities is also present, which is caused by the μ Quans laser. When detecting atoms in both hyperfine ground states, the signal remains stable.

7.3.3 Measuring the Occupation Probability

The occupation probability of the $|F = 2\rangle$ state is obtained by measuring the proportion of atoms in each hyperfine ground state. The voltage of the amplified photodiode signal is related to the number of atoms n_{at} that scatter light on the cycling transition by

$$V = \eta R_{\text{sc}}(s, \delta) n_{\text{at}} \hbar \omega G \quad (7.4)$$

where $\eta = \Omega/4\pi$ is the fractional solid angle subtended by the collection optics, $\hbar \omega = 1.6 \text{ eV}$ is the photon energy, R_{sc} is the scattering rate per atom defined in equation (4.2) and G is the photodiode conversion gain of $1.84 \times 10^6 \text{ V W}^{-1}$. At the saturation intensity and a detuning of 3 MHz , the voltage measured per atom is around 30 nV per atom. With a detection time of $200 \mu\text{s}$, around 7 photons per atom are detected. The probability of an atom occupying $|F = 2\rangle$ is estimated as follows

$$P_{|F=2\rangle} = \frac{N_2}{N_{\text{Tot}}} \quad (7.5)$$

Here the subscript 2 indicates the average voltage measured with cooling light only (detecting $|F = 2\rangle$ atoms) while the subscript Tot indicates the average voltage with the repump light as well (detecting all the atoms). The interferometer phase difference Φ is determined from equation (7.5) using

$$P_{|F=2\rangle} = P_0 - \frac{C}{2} \cos(\Phi) \quad (7.6)$$

where P_0 is the mean probability of detecting atoms in $|F = 2\rangle$ and C is the interferometer fringe contrast. These are experimentally determined by varying Φ as described in Section 7.6.1.

Atom Number Bias

After the initial state preparation is complete, there are still some residual atoms left in the states $|F = 1, m_F = \pm 1\rangle$. Also, as shown in Figure 7.7, the photodiode signal that yields N_2 is not constant because some of the $|F = 2\rangle$ atoms are optically pumped into the $|F = 1\rangle$ state. In the following, we consider how both these defects affect the validity of equation (7.6).

If atoms are pumped out of $|F = 2\rangle$ at a rate γ , then the number of atoms in $|F = 2\rangle$ is given by

$$n_2(t) = n_{20}e^{-\gamma t} \quad (7.7)$$

where n_{20} is the initial number in $|F = 2\rangle$. After averaging over a time τ , this gives

$$N_2 = \frac{n_{20}(1 - e^{-\gamma\tau})}{\gamma\tau} \quad (7.8)$$

The total number of atoms, measured during the second detection pulse is

$$N_{\text{Tot}} = n_{10} + n_{20} + n_{\pm 1} \quad (7.9)$$

where $n_{\pm 1}$ is the background population in $|1, \pm 1\rangle$ and n_{10} is the initial population in $|1, 0\rangle$. The detected probability is then

$$\begin{aligned} P &= \frac{N_2}{N_{\text{Tot}}} \\ &= \frac{\frac{n_{20}(1 - e^{-\gamma\tau})}{\gamma\tau}}{n_{10} + n_{20} + n_{\pm 1}} \end{aligned} \quad (7.10)$$

which is not the same as occupation probability from the interferometer fringe

$$P_0 = \frac{n_{20}}{n_{10} + n_{20}} \quad (7.11)$$

Dividing equation (7.10) by $n_{10} + n_{20}$, the detected probability is expressed in terms of P_0 as follows

$$P = \frac{P_0}{1 + \epsilon} \frac{1 - e^{-\gamma\tau}}{\gamma\tau} \quad (7.12)$$

where $\epsilon = \frac{n_{\pm 1}}{n_1 + n_2}$ is the ratio of the number of residual atoms to the number in the interferometer. Similarly, the contrast C of the detected fringe is related to the actual contrast C_0 by

$$C = \frac{C_0}{1 + \epsilon} \frac{1 - e^{-\gamma\tau}}{\gamma\tau} \quad (7.13)$$

For small $\gamma\tau$, this multiplicative factor is well-approximated by $\frac{1 - \gamma\tau}{1 + \epsilon}$. From Figure 7.7, around 7% of the signal is lost for $s = 3$, so $\gamma = 360 \text{ s}^{-1}$ and $\tau = 200 \mu\text{s}$. From the imperfect state preparation, after velocity selection there is roughly equal population in the $m_F = 0$ state as the $m_F = \pm 1$ states, so we assume $\epsilon = 1$. Now the detected contrast is $C = 0.46C_0$, which includes a factor of 1/2 from the $m_F = \pm 1$ atoms. This background population greatly reduces the detected fringe contrast. Increasing the purity of the state prior to interferometry will certainly be required to improve this fringe contrast.

7.4 Individual Pulse Characterisation

This section presents a characterisation of the pulses used to drive Raman transitions between the two hyperfine ground states. First, the properties of the Raman transition

spectrum are presented in Section 7.4.1. Following this, a discussion of cancelling the systematic phase from a differential ac Stark Shift is given in Section 7.4.2. Finally, this section concludes with specific details about the individual pulses used in the experiment. The first Raman pulse, which is used to select a subset of atoms with a narrow velocity spread, is presented in Section 7.4.3. This section concludes with a presentation of the dynamics of the three pulses used to coherently control the atoms during the interferometer in Section 7.4.4

7.4.1 Raman Transition Spectrum

When a circularly polarised light beam excites an atom, the angular momentum of the light is transferred to the atom. Therefore, a σ^+ circularly polarised beam raises the m_F quantum number by 1 when a photon is absorbed. Similarly, the stimulated emission induced by a σ^+ beam lowers m_F by 1. In the case of our Raman transitions, one beam (with wavevector \mathbf{k}_1) excites the atom and another (wavevector \mathbf{k}_2) stimulates it back down to the other hyperfine ground state. Table 7.1 shows the polarisation selection rules for these transitions.

Figure 7.8 shows an example of the Raman transition spectrum taken with atoms that have been launched along the Raman axis at about 8 cm s^{-1} . The beat frequency between the two Raman lasers is scanned and the light is pulsed for $160 \mu\text{s}$ to drive atoms from $|1, 0\rangle$ into the $|F = 2\rangle$ state. The labels in Figure 7.8 indicate the initial and final m_F values. There is a large narrow peak labelled $0 \rightarrow 0$ close to the hyperfine splitting frequency. This is a result of velocity-insensitive co-propagating transitions². Looking at the entry in Table 7.1 for $\Delta m = 0$, this peak indicates that the co-propagating beams do not have exactly the $\sigma^+ - \sigma^+$ polarisation that was intended. This is further

²When the two light fields are co-propagating, the Doppler shift, being proportional to $\vec{k}_1 - \vec{k}_2$ is close to zero

| Transition | k_1 | k_2 |
|-----------------|------------|------------|
| $\Delta m = -1$ | σ^- | π |
| | π | σ^+ |
| $\Delta m = 0$ | σ^+ | σ^+ |
| | σ^- | σ^- |
| $\Delta m = +1$ | σ^+ | π |
| | π | σ^- |

Table 7.1: Allowed polarisation configurations for a Raman transition coupling $|F = 1, m_F\rangle \rightarrow |F = 2, m_F + \Delta m\rangle$.

supported by the fact that there are $\Delta m = \pm 1$ transitions, which can only occur if one of the lasers drives a π transition. The Zeeman shifts on the co-propagating transitions between $|F = 1, 0\rangle \rightarrow |F = 2, 1\rangle$ and $|F = 1, 1\rangle \rightarrow |F = 2, 1\rangle$ are 0.95 MHz and 1.895 MHz, and are perfectly consistent with the known applied magnetic field of 1.4 G.

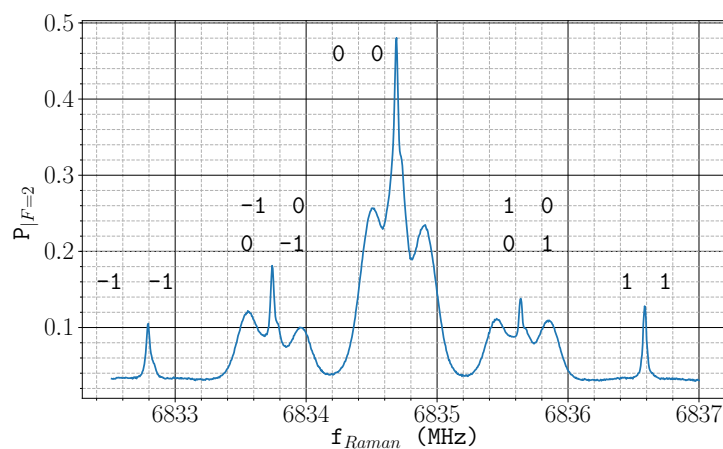


Figure 7.8: Raman transition spectrum, obtained by scanning the beat frequency of the two Raman lasers. The transitions $|1, m_F\rangle \rightarrow |2, m'_F\rangle$ are indicated at each observed peak.

Each narrow transition from $|1, 0\rangle$ has broader peaks on either side which are the Doppler-sensitive transitions produced by counter-propagating beams. The central peak is shown in more detail in Figure 7.9. The shoulder visible on the right, but not the left, of the central peak suggests an asymmetry in the forwards and backwards-propagating Raman beams which has not yet been understood. The counter-propagating transitions are shifted from the central co-propagating peak by -185 kHz and $+215\text{ kHz}$ respectively. This difference is explained by the recoil shift $\Delta f_r = \frac{1}{2\pi} \frac{\hbar k_{\text{eff}}^2}{2m} = 14.9\text{ kHz}$, which increases the resonance frequency of both counter-propagating transitions. After subtracting the recoil shift, the Doppler shifts of $\pm 200\text{ kHz}$ corresponding to velocity of 7.69 cm s^{-1} . The same Doppler shifts are also observed in the peaks corresponding to the $|F = 1, m_F = 0\rangle \rightarrow |F = 2, m_F = \pm 1\rangle$ transitions. The counter-propagating transitions are Doppler-broadened by the thermal velocity of the atoms along the direction of the Raman beams. Fitting the transition to the lineshape expected from a thermal distribution of atoms gives a temperature of $15\text{ }\mu\text{K}$ and $13.5\text{ }\mu\text{K}$ from each counter-propagating transition. At the time this spectrum was measured, the molasses was not optimised to give the lowest temperature.

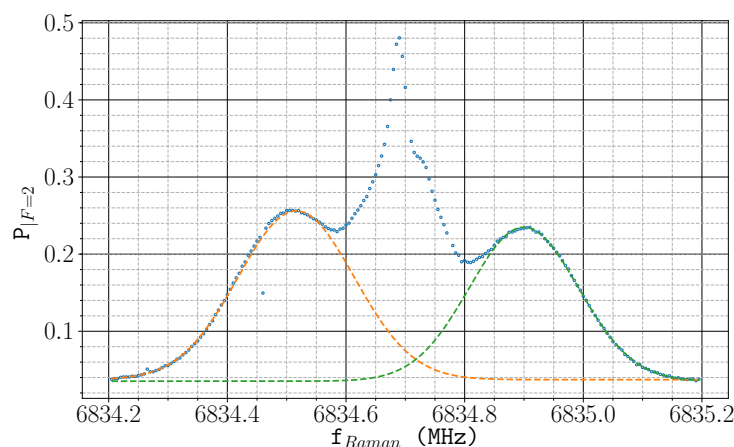


Figure 7.9: Transition spectrum showing the $\Delta m = 0$ transition from $|1, 0\rangle$. The orange and green dashed lines are fits to a Doppler-broadened lineshape for each of the counter-propagating profiles.

7.4.2 Cancelling the Differential ac Stark Shift

It is worth considering the effects of ac Stark shifts on the atom interferometer [68]. They are intrinsically related to the effective Rabi frequency and as such, cannot be avoided. Each light beam couples each hyperfine ground state to intermediate states in the $5P_{1/2}$ and $5P_{3/2}$ levels in Rubidium-87. The total ac Stark shift of each level³ is a sum over the shift from each coupled excited state

$$\Omega_j^{\text{ac}} = \sum_{ik} -\frac{|\Omega_{ijk}|^2}{2\Delta_{ijk}} \quad (7.14)$$

in terms of the one-photon Rabi frequencies Ω_{ijk} and detunings Δ_{ijk} where the index $i = 1, 2$ labels each light field, $j = 1, 2$ labels each hyperfine ground state and k labels each excited state that is coupled by a dipole transition to j . From the free evolution of the atom's internal state, there is a contribution to the phase along each path that is proportional to the sum of the light shifts of each hyperfine ground state ($\Omega_1^{\text{ac}} + \Omega_2^{\text{ac}}$). For an interferometer pulse separation of $T = 25$ ms, the maximal separation of each path is $\frac{\hbar k_{\text{eff}}}{m} T = 300 \mu\text{m}$. Close to the centre of the Raman beams, there is a negligible variation of intensity over this distance, so the sum of the ac Stark shifts of each state should not lead to an observable interferometer phase shift.

The Raman resonance depends on the difference in energy of the two states $\hbar(\omega_2 - \omega_1)$. The ac Stark shifts of each state therefore leads to a contribution to the detuning that depends on the differential ac Stark shift $\delta^{\text{ac}} = \Omega_2^{\text{ac}} - \Omega_1^{\text{ac}}$. can lead to an observable phase shift. Using the results from Ref. [28] for π and $\frac{\pi}{2}$ pulses, the phase shift to a Mach-Zender type interferometer is

$$\Delta\Phi^{\text{ac}} = \frac{\delta_3^{\text{ac}}}{\Omega_{\text{eff}}} - \frac{\delta_1^{\text{ac}}}{\Omega_{\text{eff}}} \quad (7.15)$$

³The ac Stark shift term in equation (2.20a) was defined assuming that each field E_j couples to only one ground state $|j\rangle$. Here, we do not make that assumption.

where δ_3^{ac} and δ_1^{ac} are the ac Stark shifts of the last and first $\frac{\pi}{2}$ pulses, respectively, and Ω_{eff} is the effective Rabi frequency defined in equation (2.30). Note that there is no sum over the beam index k , because in making the rotating wave approximation, terms which contain Δ_{21k} and Δ_{12k} are dropped as they oscillate much faster than the retained terms.

As the atoms fall under gravity, they move through the Raman beam profile and experience the interferometer pulses at different intensities. To the extent that there is a light shift of the clock transition, this can produce a non-zero interferometer phase. Fortunately, it is possible to eliminate such a shift using an appropriate choice of intensity and detuning of the Raman lasers. This can be seen by first writing out the differential ac Stark shift

$$\delta^{\text{ac}} = \Omega_1^{\text{ac}} - \Omega_2^{\text{ac}} = \sum_{ik} \frac{|\Omega_{i1k}|^2}{2\Delta_{i1k}} - \sum_{ik} \frac{|\Omega_{i2k}|^2}{2\Delta_{i2k}} \quad (7.16)$$

When both Raman beams are red-detuned from all the one-photon transitions, both terms in equation (7.16) are strictly negative. Here, we consider transitions to states in the $5P_{1/2}$ and $5P_{3/2}$ levels, so this is indeed the case. Therefore, δ^{ac} can be cancelled by choosing the correct intensities for each Raman beam. Figure 7.10 shows the results of a calculation of differential ac Stark shift. Using a specified intensity, polarisation and detuning for each beam, the Rabi frequencies of the couplings between each ground state and each excited state were calculated. From these, the Rabi frequency of the Raman transition and the differential ac Stark shift are then obtained.

Figure 7.10 shows the differential ac Stark shift δ^{ac} for various Raman beam intensities as a function of the ratio of their intensities (relative to the intensity of the light closest to resonance with transitions from the $|F = 2\rangle$ state). There is a ratio at which the differential ac Stark shift cancels and is independent of the total intensity. The one-photon detuning Δ_R is defined such that the laser frequency ω_2^l is detuned from the

$|F = 2\rangle \rightarrow |F' = 3\rangle$ transition (in the absence of light shifts) by Δ_R . The ratio that cancels δ^{ac} for increasing Δ_R is shown in Figure 7.10b. When Δ_R is 1.13 GHz below the $|F = 2\rangle \rightarrow |F' = 3\rangle$ transition, this ratio is maximised. The differential ac Stark shift is cancelled when the intensity ratio of light driving $|1, 0\rangle$ transitions to $|2, 0\rangle$ transitions is $\mathcal{R} = 0.583$.

It is not straight-forward to directly measure the intensity of each Raman beam on the atoms, so the transition spectrum was used to cancel the differential ac Stark shift and determine when the intensities of the lasers are set to the appropriate ratio. Experimentally, this was done by adjusting the power of the pump lasers for the master and slave SolsTiS lasers. When the master is seeded with 10 W and the slave with 6.5 W, the differential ac Stark shift is eliminated. Figure 7.11 shows the transition spectrum using two different effective Rabi frequencies, corresponding to π pulse times of 22.5 μ s and 45 μ s. In this instance, the frequency difference of the two co-propagating peaks, shown in blue and orange, is 880 Hz. If we assume that their shifts are entirely due to the ac Stark shift and that these Rabi frequencies corresponded to those of the first and last interferometer pulses, respectively, this results in an interferometer phase shift of $\Delta\Phi^{ac} = 23$ mrad. This is almost certainly an overestimate, as it is unlikely that the Rabi frequency and differential ac Stark shift will vary as much as this between the first and last interferometer pulses. There is also a shift of 1.4 MHz from f_{hfs} . This is a result of a second-order Zeeman shift and corresponds to a field strength of 1.56 G, which is consistent with the value measured previously in Section 7.4.1.

7.4.3 Velocity-Selective Pulse

The accelerometer has to use the velocity-sensitive transitions induced by counter-propagating beams in order to be sensitive to acceleration. In order for all the atoms

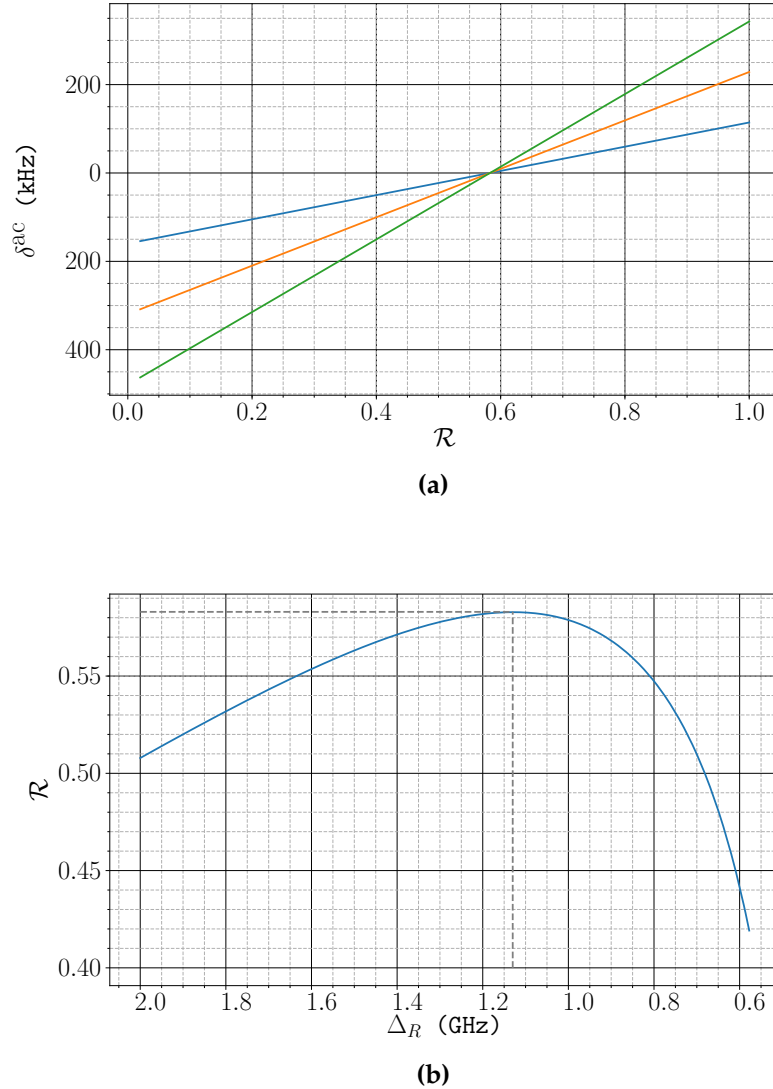


Figure 7.10: A simulation of the effects of the Raman beam intensities and detuning on the differential ac Stark shift δ^{ac} . The Raman Rabi frequency and ac Stark shifts of the two hyperfine ground states are calculated using the transition matrix elements to states in the $5P_{1/2}$ and $5P_{3/2}$ levels. (a) shows δ^{ac} as a function of the intensity ratio \mathcal{R} between the light which drives transitions from $|1, 0\rangle$ to the light that couples to $|2, 0\rangle$ for the two-photon detuning of $\Delta_R = -1.13$ GHz used in the experiment. Example intensities for the $|2, 0\rangle$ light are 100 W m^{-2} (blue), 200 W m^{-2} (orange) and 300 W m^{-2} (green). (b) shows how the ratio for which $\delta^{ac} = 0$ varies as Δ_R increases. The dashed lines indicate the value of $\Delta_R = -1.13$ GHz and its corresponding ratio of 0.583.

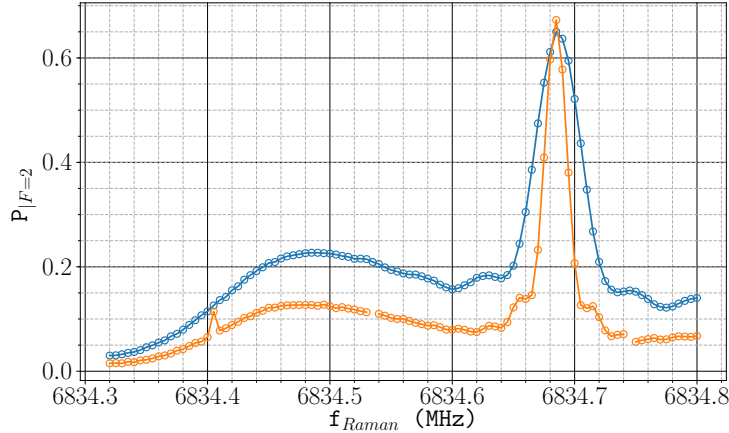


Figure 7.11: Raman transition spectrum after cancelling the differential ac Stark shift. The blue curve shows a pulse with a π pulse time of 22.5 μs and the orange shows the spectrum using a less intense pulse with a π -pulse time of 45 μs .

to experience the same desired pulse areas of $\pi/2 - \pi - \pi/2$, it is necessary for the Doppler width to be much less than the natural width arising from the duration of the Raman pulses. In this apparatus, the laser cooling gives a temperature of 6 μK , for which the Doppler width (FWHM) is $\sigma_f = \frac{4\sqrt{2\ln(2)}}{\lambda} \sqrt{\frac{k_b T}{m}} \approx 140 \text{ kHz}$. A π -pulse duration of 6 μs gives a linewidth close to this Doppler width, but the intensities required for this are above what is attainable with our Raman laser.

We therefore reduce the Doppler width of the participating atoms by first applying a long Raman pulse to select a subset of the population with a narrower velocity spread [69]. This velocity-selective pulse gives a narrower Doppler linewidth than the subsequent shorter interferometer pulses thereby ensuring that the Rabi frequencies are reasonably homogeneous across the cloud of selected atoms.

Starting with a velocity distribution of atoms described by a 1-D Maxwell-Boltzmann distribution all occupying the $|1, 0\rangle$ state, the population in $|2, 0\rangle$ after applying a

Raman pulse is distributed according to

$$P_{|2,0\rangle}(v) = \frac{\Omega_{\text{eff}}^2}{\Omega_{\text{eff}}^2 + \delta^2} \sin \left(\frac{\sqrt{\Omega_{\text{eff}}^2 + \delta^2} \tau}{2} \right)^2 p(v) \quad (7.17)$$

where δ is the Raman detuning defined in equation (2.17), $p(v) = \sqrt{\frac{m}{2\pi k_B T}} e^{-\frac{mv^2}{2k_B T}}$ is the velocity distribution and Ω_{eff} is the effective Rabi frequency defined in equation (2.30). Figure 7.12 shows the expected distribution of Doppler shifts in the selected atoms after a 6 μK cloud has been driven by a π pulse with a duration of 40 μs . The population that is stimulated has a mean velocity shifted by twice the recoil velocity. In this instance, the rms Doppler shift is $\sigma_f = 19.7 \text{ kHz}$.

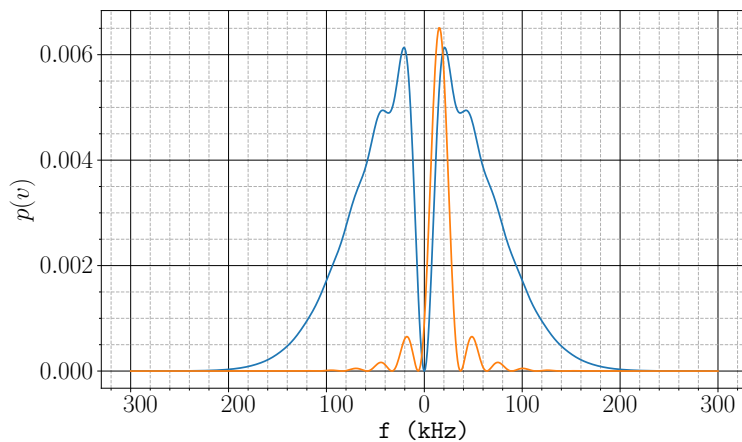


Figure 7.12: Calculated distribution of frequency shifts in the ensemble selected from a 6 μK cloud by a 40 μs Raman π pulse. Blue curve: atoms not selected. Orange curve: atoms selected. Note the recoil shift of the selected atoms in addition to their Doppler shifts.

Velocity-Selected Distribution

The velocity distribution of atoms after the velocity selective pulse can be measured using a second Raman pulse as a probe. This probe must be much longer duration

than the velocity-selection pulse so that it gives even narrower resonances. Figure 7.13 shows a measurement of the transition spectrum close to the peak of the Doppler-sensitive transition that is greater in frequency than the Doppler-insensitive peak. The orange curve shows the spectrum obtained before velocity selection, using a single Raman π pulse of duration 40 μ s. The blue curve, which illustrates the distribution of atoms after velocity selection, is obtained by first applying a 40 μ s π pulse with a Raman beat frequency $f_v = 6834.51$ MHz. This prepares atoms in $|1,0\rangle$, then the atoms which remain in $|F = 2\rangle$ are blown away. After 10 ms, a 80 μ s π pulse transfers some of the remaining population back into $|2,0\rangle$. The frequency of the probe pulse is varied by chirping the Raman laser beat frequency. In this instance, the power of the 80 μ s pulse was not tuned to give a π pulse area so the measured population is not indicative of the maximum driven by the Raman transition. The red curve shows a fit to a Doppler-broadened lineshape, which gives an effective temperature of around 1 μ K. Comparing this to the peak from before velocity selection, it is clear that the velocity distribution of the selected atoms is much narrower.

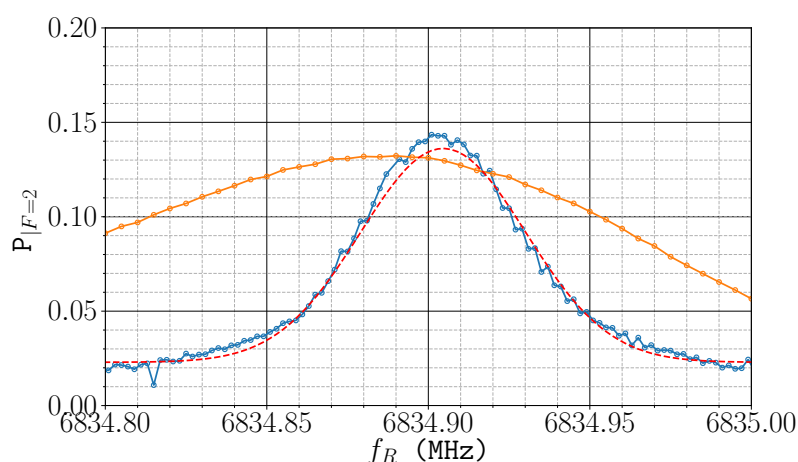


Figure 7.13: $|F = 2\rangle$ population after a Raman pulse at a frequency $f_v = 6834.51$ MHz transfers atoms to $|1,0\rangle$. This distribution is probed by applying a narrow pulse at a frequency f_R . The population measured in $|F = 2\rangle$ is shown in blue. The red dashed line is a fit to the Doppler-broadened transition peak. The orange curve shows transition spectrum (without velocity selection) from a π -pulse of duration $\tau = 40 \mu\text{s}$.

7.4.4 Interferometer Pulses

The power settings needed to make Raman π and $\pi/2$ pulses were empirically determined by observing Rabi oscillations. These are shown in Figure 7.14. For a π pulse, the Raman laser power was set so that the Rabi oscillation reached its maximum after a pulse duration of $\tau = 15 \mu\text{s}$. It is clear that the oscillations are rapidly damped. This dephasing rate depends on the time at which the pulse is applied. Since the atoms are at different positions in the beam, this suggests that the dephasing is caused by a spatial variation of the Rabi frequency. This is largely a result of irregularities in the Raman beam intensity profile from defects in the two small aspheric lenses. The Gaussian intensity distribution of each beam is unlikely to cause such a fast dephasing, since the atoms remain close to the centre of the beam. At longer pulse durations, spontaneous decay from the intermediate states of the Raman transition becomes apparent.

7.5 Noise

This section presents a discussion of the identified sources of noise in the interferometer and their effects on the sensitivity to accelerations. It begins with a discussion of the noise that arises from detecting atoms in Section 7.5.1. This defines an uncertainty in measuring the occupation probability, which is then used to express the corresponding acceleration uncertainty in Section 7.5.2. The Allan variance used to characterise the stability of the interferometer signal is defined in Section 7.5.3. The sensitivity function and an analytic method for calculating the influence of random phase fluctuations is given in Section 7.5.4. This is applied to phase noise from the Raman laser in Section 7.5.5 and external vibrations in Section 7.5.6. Finally, the section concludes with a summary of the identified sources of noise in Section 7.5.7.

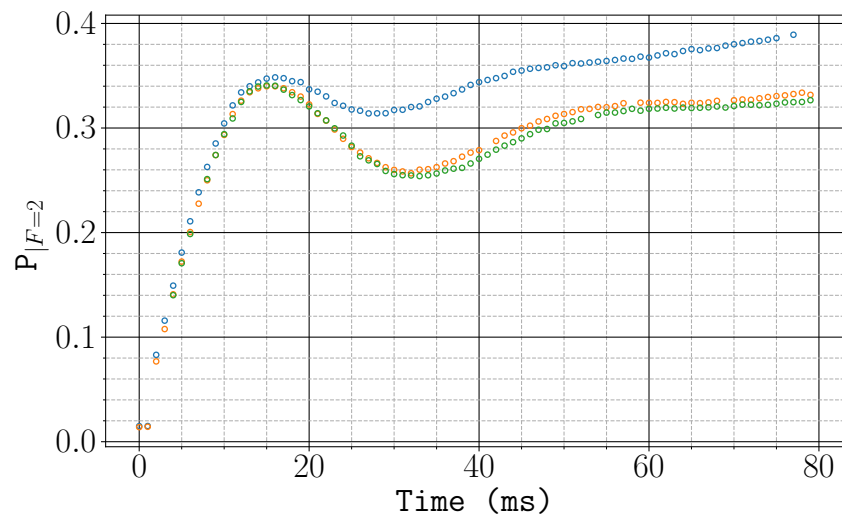


Figure 7.14: Rabi oscillations between the $|1,0\rangle$ and $|2,0\rangle$ states. The atoms are pre-selected using a narrow velocity-selective pulse of duration $40\text{ }\mu\text{s}$ after launching along the Raman axis and vertically with a velocity of 27 cm s^{-1} so the atoms remain close to the centre of the beam. Each pulse occurs at different times after the MOT is released. The times shown are 13 ms (blue), 23 ms (orange) and 33 ms (green). The atoms come to rest after 27.5 ms and close to the apogee, the coherence is stronger. Full population transfer is not observed due to the atoms in $|1,\pm 1\rangle$ which have not been removed.

7.5.1 Detection Noise

Each measurement of the number of atoms has an uncertainty due to random processes that influence the voltage measured by the detector. These errors combine to give an uncertainty in the interferometer phase and hence, acceleration. It is worth distinguishing between the different sources of noise in measuring the occupation probability $P_{|F=2\rangle}$. Fluctuations in the number of atoms and detected photons lead to an uncertainty in the measured voltages that correspond to N_2 and N_{Tot} . However, the main fundamental limitation is the noise that arises when an atom is projected into either the $|1, 0\rangle$ state or the $|2, 0\rangle$ state. In what follows, these three sources of detection noise are discussed in the context of the detection sequence previously described in Section 7.3.2. Naturally, we aim to have a good enough photo-detector that this is not a limiting source of noise.

Atom and Photon Number Fluctuations

The random processes by which atoms are loaded and cooled in the initial stages of the experiment, as well as the random direction a photon is spontaneously emitted mean that both the total number of atoms after interferometry and the number of photons arriving at the detector within a given time duration will have shot noise fluctuations. Thus, the mean voltage measured by the detector over an integration time of τ should have a shot-noise variation of

$$\sigma_v^2 = \alpha^2 \eta^2 R_{\text{sc}}^2 n_{\text{at}} \left(1 + \frac{1}{q \eta R_{\text{sc}} \tau} \right) \quad (7.18)$$

where $\alpha = \hbar \omega G$ converts the photon rate incident on the photodiode to an output voltage and q is the quantum efficiency of the photodiode. The first and second terms

represent the number fluctuations of atoms and photons respectively. The denominator $q\eta R_{sc}\tau$ is just the number of photons detected per atoms.

As previously discussed in Section 7.3.2, around 7 photons per atom so the photon shot noise is much less than that of the atoms. For few million atoms that we use, the predicted statistical noise is approximately 0.1 mV. In practice however, the measured shot-to-shot noise is much higher than that – typically 3 mV. This is due to fluctuations in the number of atoms collected in the MOT, which arise in turn from fluctuations of the MOT laser intensity and polarisation. Fortunately, the method we use for determining acceleration makes us insensitive to the atom number fluctuations. The occupation probability $P_{|F=2\rangle}$ is determined by taking the ratio of N_2 and N_{Tot} . Because these are both measured on the same group of atoms, the number of atoms cancels out in the ratio and the shot-to-shot noise is suppressed in $P_{|F=2\rangle}$.

Quantum Projection Noise

Although the determination for $P_{|F=2\rangle}$ does not suffer from atom number fluctuations, there is an uncertainty arising from the projection of an atom's internal state onto the $|2,0\rangle$ state when we detect N_2 . Consider a number of atoms n_{10} prepared in state $|1,0\rangle$. Let the probability of their making a transition to $|2,0\rangle$ be $\langle p_2 \rangle$. Then the number arriving in state $|2,0\rangle$ is $n_{10}(\langle p_2 \rangle \pm \langle p_2 \rangle(1 - \langle p_2 \rangle))$, where the uncertainty is the quantum projection noise [67]. Therefore, the measured transition probability is given by

$$\begin{aligned} P_{|F=2\rangle} &= \frac{\langle p_2 \rangle n_{10} \pm \sqrt{n_{10} \langle p_2 \rangle (1 - \langle p_2 \rangle)}}{n_{10}(1 + \epsilon)} \\ &= \frac{\langle p_2 \rangle}{1 + \epsilon} \pm \frac{1}{1 + \epsilon} \sqrt{\frac{\langle p_2 \rangle (1 - \langle p_2 \rangle)}{n_{10}}} \end{aligned} \quad (7.19)$$

where as discussed in Section 7.3.3, ϵ accounts for the unwanted atoms left in $m_F = \pm 1$ (and it is assumed for simplicity that this ratio does not fluctuate). For a given interferometer phase Φ , $\langle p_2 \rangle = \sin^2(\Phi/2)$, giving an interferometer fringe pattern, including the quantum projection noise, of

$$P_{|F=2\rangle} = \frac{1 - \cos(\Phi)}{2(1 + \epsilon)} \pm \frac{1}{2(1 + \epsilon)} \frac{\sin(\Phi)}{\sqrt{n_{10}}} \quad (7.20)$$

A useful measure of the interferometer's sensitivity is given by the ratio of the noise to the fringe amplitude which is

$$S = \frac{\sin(\Phi)}{\sqrt{n_{10}}} \quad (7.21)$$

and is independent of ϵ . The interferometer is most sensitive to acceleration at the mid-point of a fringe where $\Phi = \frac{\pi}{2}$. There, the quantum projection noise has its maximum value relative to the fringe amplitude of $1/\sqrt{n_{10}}$. The corresponding uncertainty in acceleration is derived in Section 7.5.2. Note that the photon shot noise, being small compared with the noise from atom number fluctuations, is also small compared with projection noise.

Photodiode Technical Noise

The quantum projection noise is an irreducible noise level coming from the atoms⁴. Not wishing to have more noise than that, we should choose a suitably quiet detector. Technical noise in the detector typically arises from multiple electronic processes – such as Johnson noise and shot noise in the current [71]. The technical noise of the detector was determined by measuring the output voltage when no light is collected. A plot of the power spectral density of the photodiode is shown in Figure 7.15 taken

⁴This can be reduced by squeezing the pseudospin representing the clock transition coherence [67], but we do not do that here.

with a sampling frequency of 200 kHz. The photodiode was covered and the output voltage was sampled for 2 s. The power spectral density has been calculated using Welch's method [72]. The data are partitioned before calculating the Fourier transform of each subset and taking the average. This has the effect of reducing the variance in the estimated power spectrum at the expense of reducing the frequency resolution. Below 10 kHz the power spectral density is close to uniform with a value of around $5 \times 10^{-13} \text{ V}^2 \text{ Hz}^{-1}$, which corresponds to a noise-equivalent power of $391 \text{ fW Hz}^{-1/2}$. For higher frequencies, the power spectral density starts to increase.

The variance of the detector noise is given by the integral of the noise power spectral density over the bandwidth B , which is related to the integration time τ according to $B = 1/(2\tau)\text{Hz}$. The blue solid line in Figure 7.16 shows how the detector noise variance, obtained using the power spectral density from Figure 7.15, decreases as the integration time is increased and the high-frequency noise averages out. In the same plot, the dashed red line shows the variance of the signal voltage resulting from quantum projection noise when $n_{10} = 3 \times 10^6$, as is typical in the apparatus. The dot-dashed line corresponds to a detection time of 200 μs which is normally the time we use. One can see that the detector noise is a little larger than the quantum projection noise. Adding the two variances and taking the square root, we find that the quantum projection noise of 40 μV is inflated by the detector noise to 90 μV . In future, it would be good to replace the detector by one with lower noise. It might also be possible to increase τ , but in practice this causes an undesirable deterioration of the signal.

Summary of Detection Noise

It is worth summarising the various contributions to the noise in the occupation probability $P_{|F=2\rangle}$. Fluctuations in the atom number and detected photon number lead to shot noise contributions to the voltages corresponding to N_2 and N_{Tot} . However,

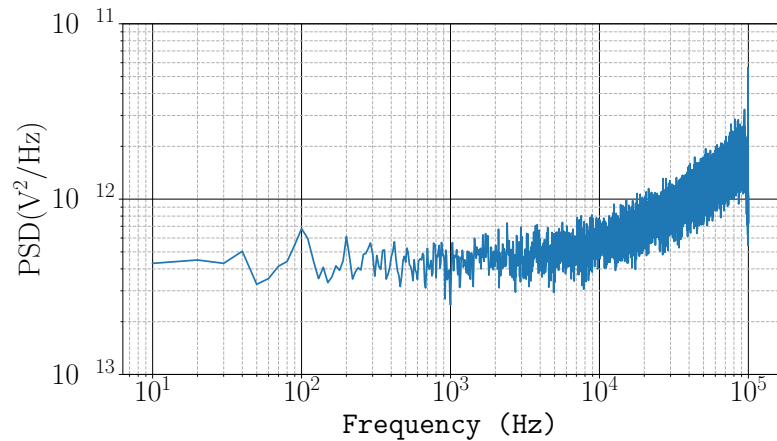


Figure 7.15: Power spectral density of the voltage from the amplified photodiode signal sampled for 2 s at a rate of 200 kHz.

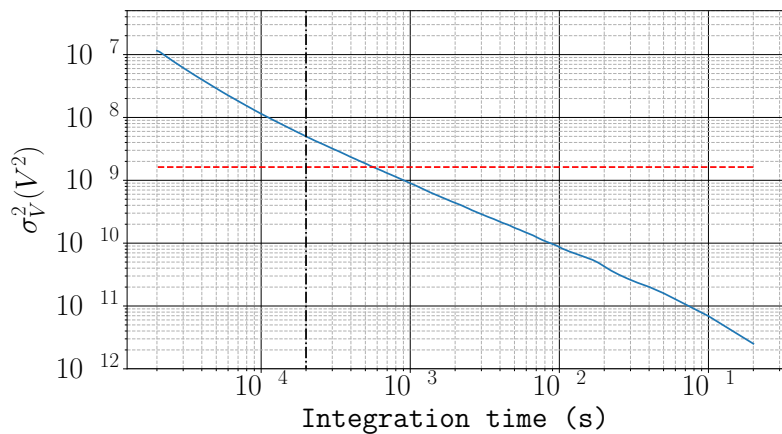


Figure 7.16: Detector noise variance as a function of integration time, shown in blue. This is obtained by integrating the power spectral density from Figure 7.15 up to a frequency corresponding to the inverse of twice the integration time. The red curve is the variance in the voltage expected from the quantum projection noise of 3×10^6 atoms. The dot-dashed line indicates the integration time of 200 μs that is presently used.

we detect many photons per atom and in taking the ratio of the two voltages, the contribution of variations in the total atom number to $P_{|F=2\rangle}$ is largely suppressed. Thus the main fundamental noise comes from the quantum projection noise. There is also technical noise in the detector. At present, the technical detector noise is slightly greater than the projection noise. In the future, it would be good to replace the detector with a quieter one.

7.5.2 Acceleration Uncertainty

The measurement of $P_{|F=2\rangle}$ is interpreted as a measurement of acceleration assuming that $P_{|F=2\rangle}$ has the form $P_0 - (C/2) \cos(\Phi)$. In the sensitive region of the fringe pattern, where the slope is highest, we may rewrite $\Phi = (2n - 3/2)\pi + \theta$. Here n is the order number of the fringe. That gives $P_{|F=2\rangle} = P_0 + (C/2) \sin(\theta)$, or $P_0 + (C/2)\theta$ for small θ . Similarly, on the sides of the fringe with the most negative slope, we have $\Phi = (2n - 1/2)\pi + \theta$ which yields $P_0 - (C/2)\theta$ for small θ . The accelerometer is calibrated by measuring P_0 and C . Then, recalling from Section 2.2.2 that $\Phi = k_{\text{eff}}aT^2$, it is straightforward to determine a as long as the order number is known. Operating near these points of large slope, the noise σ_{P_2} translates to acceleration noise $\sigma_a = \frac{2}{Ck_{\text{eff}}T^2} \frac{1}{(1+\epsilon)\sqrt{n_{10}}}$. So it is clear that the uncertainty in measuring the acceleration is made small by increasing the number of atoms or by increasing the time between interferometer pulses. The wavelength of the Rubidium transition fixes the value of k_{eff} . Taking the best possible case in which $C = 1$, $\epsilon = 0$ and there is no detector noise, our current number of 3×10^6 atoms and our current interaction time of 25 ms together give $\sigma_a = 100 \text{ nm s}^{-2}$. In terms of the interferometer phase, that corresponds to a noise $\sigma_\Phi = \frac{2}{\sqrt{n_{10}}} = 1 \text{ mrad}$. At present however, the phase lock for the Raman beams has approximately 10 mrad of noise, leading us to expect an uncertainty to acceleration of order $1 \mu\text{m s}^{-2}$ in practice, as discussed further in Section 7.5.4 below.

7.5.3 The Allan Variance

So far we have only considered random noise, for which the variance converges over a large enough sample. For correlated noise, this is not necessarily the case and then it is useful to measure the Allan variance. This measures the mean square difference between averages over successive groups of N measurements. Thus the Allan variance is [73].

$$\sigma_{\text{av}}^2(N) = \frac{1}{2} \left\langle \left(\frac{1}{N} \sum_{k=0}^{N-1} a_{n+1} - \frac{1}{N} \sum_{k=N}^{2N-1} a_n \right)^2 \right\rangle \quad (7.22)$$

The Allan variance can be used to identify the timescales that characterise the behaviour of the bias in an accelerometer [74]. At short timescales the variance in successive measurements is typically uncorrelated, giving white noise for which the Allan variance scales as $1/N$. At longer timescales the bias instability – fluctuations of the bias value – causes the Allan variance to reach a minimum value. Finally, at still longer timescales, the bias drift – a long-term change in the bias value – causes an increase in the Allan variance. Table 7.2 summarises these three processes and their characteristic dependences on the number of samples N in each group.

| Process | N dependence |
|------------------|----------------|
| White noise | N^{-1} |
| Bias instability | N^0 |
| Bias drift | N^2 |

Table 7.2: Allan variance characteristic timescales.

7.5.4 The Sensitivity Function $g(t)$

The sources of noise presented thus far arise from various uncertainties in measuring the number of atoms from their fluorescence. When using the atom interferometer to measure accelerations, there is additional noise from fluctuations of the Raman phase and from real vibration noise. I consider first the effect on the interferometer phase Φ from fluctuations of the Raman phase ϕ .

Let a small fluctuation $\delta\phi$ at time t produce a fluctuation $\delta\Phi$ of the interferometer phase. Making a first-order Taylor expansion, we can write

$$\delta\Phi = \lim_{\delta\phi \rightarrow 0} \left(\frac{\delta\Phi}{\delta\phi(t)} \right) \delta\phi(t) = g(t)\delta\phi(t) \quad (7.23)$$

where the last step defines the sensitivity function $g(t)$ [75]. If ϕ fluctuates continuously, then the total shift of Φ is

$$\begin{aligned} \Delta\Phi &= \int_{-\infty}^{\infty} g(t) d\phi(t) \\ &= \int_{-\infty}^{\infty} g(t) \frac{d\phi}{dt} dt \end{aligned} \quad (7.24)$$

Consider our $\pi/2 - \pi - \pi/2$ interferometer where the three pulses have an identical Rabi frequency Ω and durations $\tau, 2\tau$ and τ . Defining $t = 0$ to be at the middle of the sequence, the first pulse begins at time $-(2\tau + T)$ and the last pulse ends at $(2\tau + T)$. Outside that region the Raman phase has no influence on the interferometer phase and $g(t) = 0$. Within that region, we have for positive times [76]

$$g(t) = \begin{cases} \sin(\Omega t) & 0 < t < \tau \\ 1 & \tau < t < \tau + T \\ \sin(\Omega(t - T)) & \tau + T < t < 2\tau + T \end{cases} \quad (7.25)$$

and for negative times we have $g(t) = -g(-t)$.

7.5.5 The Interferometer Transfer Function $H(\omega)$

The sensitivity function $g(t)$ is now used to derive the transfer function $H(\omega)$, which relates the frequency dependent response of the interferometer phase to fluctuations of the Raman phase. We first consider the response to a phase modulation at a fixed frequency ω and an arbitrary phase offset ψ , which is written as $\phi(t) = A_\omega \cos(\omega t + \psi)$. Substituting this into equation (7.24) we obtain

$$\Delta\Phi = -A_\omega \omega \cos(\psi) \int_{-\infty}^{\infty} g(t) \sin(\omega t) dt \quad (7.26)$$

where the term proportional to $\cos(\omega t)$ has been dropped, since $g(t)$ is an odd function. The integral in equation (7.26) is the Fourier transform of $g(t)$. Let us define

$$H(\omega) = -\omega \int_{-\infty}^{\infty} g(t) \sin(\omega t) dt, \quad (7.27)$$

then we can write equation (7.26) as

$$\Delta\Phi = A_\omega \cos(\psi) H(\omega) \quad (7.28)$$

Using equation (7.25) we find that

$$H(\omega) = \frac{4\omega\Omega}{\omega^2 - \Omega^2} \sin\left(\frac{\omega(T+2\tau)}{2}\right) \left(\cos\left(\frac{\omega(T+2\tau)}{2}\right) + \frac{\Omega}{\omega} \sin\left(\frac{\omega T}{2}\right) \right). \quad (7.29)$$

Figure 7.17 plots $|H(\omega)|$ using equation (7.29) for $T = 25$ ms and $\tau = 20$ μ s. The asymptotic properties of this function can be summarised as follows:

- At low frequencies $\omega \ll \Omega$, then

$$H(\omega) \approx 4 \sin^2 \left(\frac{\omega T}{2} \right) \quad (7.30)$$

which is a periodic function that is zero at frequency multiples of $2\pi/T$

- At frequencies $\omega \gg \Omega$, then

$$H(\omega) \approx 2 \frac{\Omega}{\omega} \sin(\omega T) \quad (7.31)$$

which is zero when ω is an integer multiple of π/T .

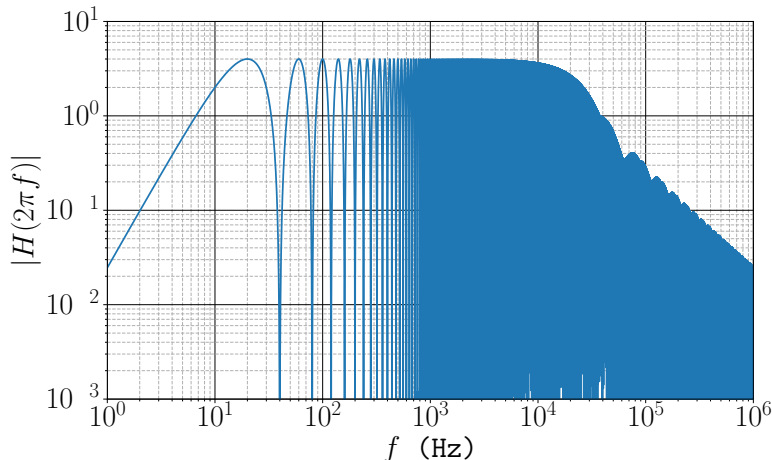


Figure 7.17: Transfer function for Raman phase noise calculated using equation (7.29). Here, the separation between pulses is $T = 25$ ms and the $\pi/2$ pulse time is $\tau = 20$ μ s.

Let us return to an arbitrary Raman phase with a power spectral density $S_\phi(\omega) = \frac{1}{2}|A_\omega|^2$, where the factor 1/2 is obtained by averaging over $\cos^2(\psi)$. The power spectral density of the interferometer phase is given by $S_\phi(\omega)|H(\omega)|^2$. Therefore, its variance is given by the following integral

$$\sigma_{\Delta\Phi}^2 = \int_{-\infty}^{\infty} S_\phi(\omega)|H(\omega)|^2 d\omega \quad (7.32)$$

The Raman phase noise is measured using the beat-note between the two Raman frequencies together (see Figure 7.1). The phase is extracted from the Fourier transform of the beat-note time series. Figure 7.18a shows the Raman phase measured over a period of 20 s⁵ where there is a drift on the order of 10 rad. Fortunately, this is not of great concern because the interferometer is only sees the change of the Raman phase during the sequence of three pulses. Figure 7.18b shows the variation of the Raman phase over the first 50 ms, which is the total interrogation time for a pulse separation of $T = 25$ ms (the duration of each pulse is negligible). Over this short time, the Raman phase is much more stable. Figure 7.18c shows the power spectral density of the Raman phase noise obtained by averaging the power spectra for each of ten two-second samples. Below 1 kHz, the power spectral density shows a $1/f^2$ dependence, which is characteristic of integrated white noise. Below 1 Hz, there is an excess of noise which corresponds to the slow drift seen in Figure 7.18a. Resonances around 2 kHz, 2.4 kHz, 3 kHz and 3.4 kHz (and multiples thereof) are also present. In future, it would be ideal to reduce these. Figure 7.18d shows the calculated power spectral density of the interferometer phase, obtained by multiplying the measured laser phase noise power spectral density with $H(\omega)^2$. The highest peak is at 20 Hz which corresponds to the inverse of the interrogation time $1/(2T)$. The bandwidth of the Raman laser PLL is much greater than the 5 kHz bandwidth of this phase noise measurement (sampled at 100 μ s intervals) as evidenced by the fact that the Raman laser PLL ensures that the power spectral density of the interferometer phase is suppressed. A measurement of the Raman phase power spectral density at higher frequencies has not yet been undertaken. It is expected that the phase noise spectral density will increase as the frequency approaches the bandwidth of the PLL. Since this is much greater than both the Rabi frequency and the inverse of the interrogation time, it is unlikely that the

⁵Credit for acquiring this data goes to M-Squared Lasers.

higher-frequency Raman phase noise will contribute to the interferometer phase noise.

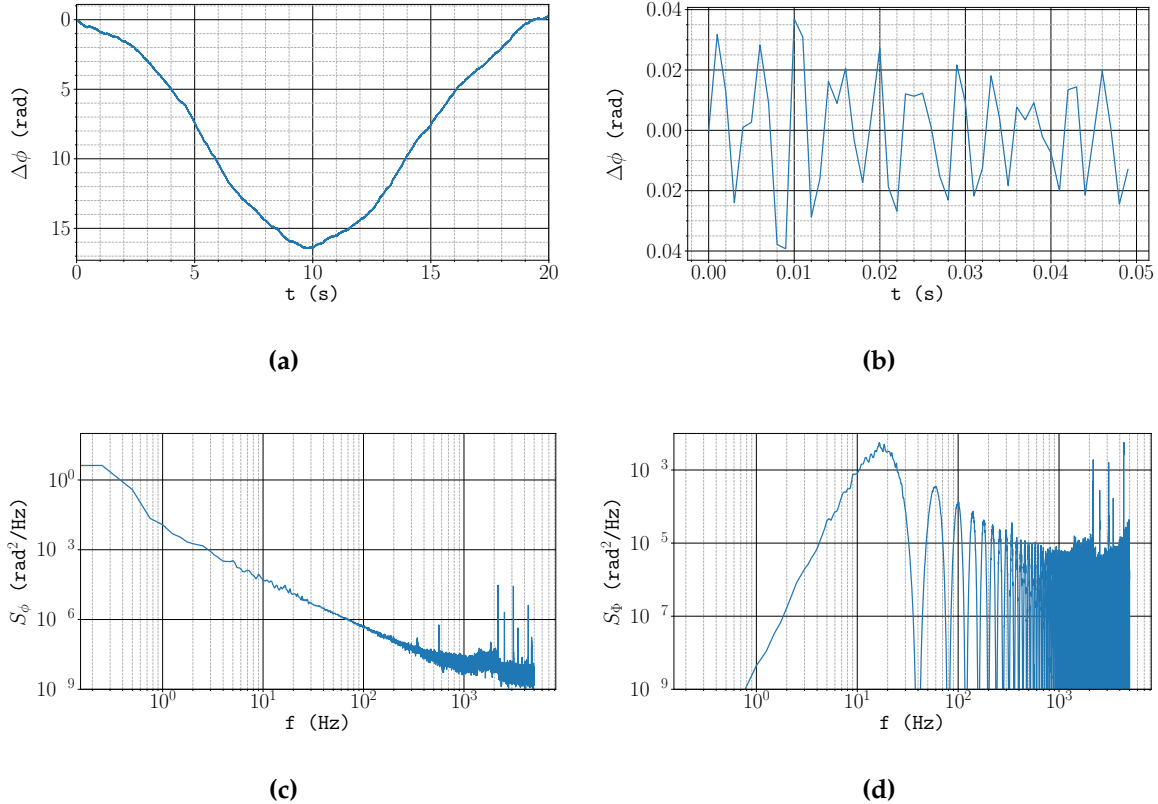


Figure 7.18: (a) shows the variation in the Raman phase over a period of 20 s sampled at a frequency of 10 kHz. (b) shows the first 50 ms of this same variation. (c) is the power spectral density of the laser phase noise, obtained by averaging over 10 samples, each of duration 2 s. (d) is the resultant power spectral density of the interferometer phase, which is multiplied by $|H(\omega)|^2$.

One can see in Figure 7.18a that there are slow drifts in the Raman phase, so it is natural to characterise the shot-to-shot variation of the interferometer phase using the Allan deviation introduced in Section 7.5.3 . The measured Raman phase variation is first partitioned into sets of duration $2T = 50$ ms, from which the interferometer phase shift $\Delta\Phi$ is calculated using equation (7.24) to represent a single "measurement". Figure 7.19 shows the Allan deviation of the interferometer phase as a function of N , the number of measurements averaged in each group. Large short term fluctuations on

the order of 50 mrad are present. In spite of the slow drift in the Raman phase, the Allan deviation decreases as N increases. When averaging over at least 5 measurements, we can expect an Allan deviation of less than 15 mrad. This fluctuation is an order of magnitude larger than the previously discussed quantum projection noise and photodiode technical noise and therefore limits the acceleration sensitivity in the absence of external effects such as vibrations. This ultimately depends on the stability of the reference oscillator in the Raman laser PLL. Replacing this with one of lower phase noise will act to reduce the shot-to-shot variation of the interferometer phase.

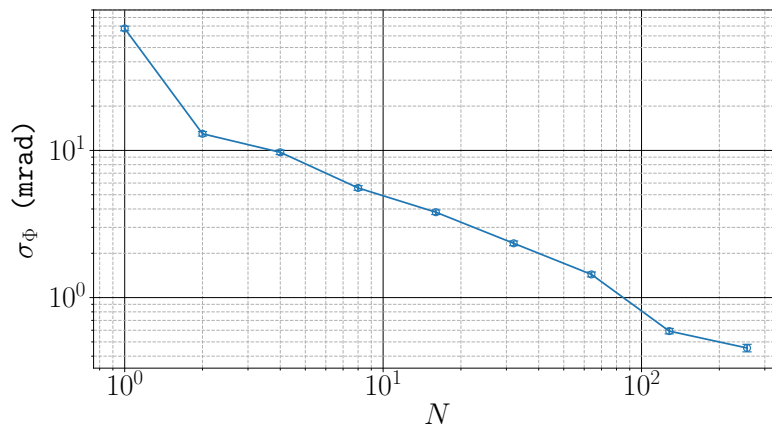


Figure 7.19: Allan deviation of the interferometer phase due to the Raman laser phase with an interferometer pulse separation of $T = 25$ ms for number of samples N . It is assumed that there is no measurement dead-time.

7.5.6 Vibrations

Mechanical vibrations also introduce Raman phase noise. If the mirror moves by an amount δz and we assume that \mathbf{k}_2 is the reflected beam then the Raman phase changes by an amount $\delta\phi = 2k_2\delta z$. Therefore, in terms of the position power spectral density of the mirror $S_z(\omega)$, the interferometer phase power spectral density is $4k_2^2 H(\omega)^2 S_z(\omega)$. To see how this relates to acceleration noise, we first express $z(t)$ in terms of its Fourier

spectrum. After differentiating twice, it is straightforward to see that the acceleration power spectral density $S_a(\omega)$ is given by

$$S_a(\omega) = \omega^4 S_z(\omega) \quad (7.33)$$

If $H_a(\omega)$ is the acceleration transfer function, then $H_a(\omega)^2 S_a(\omega) = H(\omega)^2 S_\phi(\omega)$ which results in

$$H_a(\omega)^2 = \frac{4k_2^2}{\omega^4} H(\omega)^2 \quad (7.34)$$

In the low frequency limit $\omega \ll \Omega$, this simplifies to

$$H_a(\omega)^2 = \frac{64k_2^2}{\omega^4} \sin^4 \left(\frac{\omega T}{2} \right) \quad (7.35)$$

Figure 7.20 shows the acceleration transfer function for a pulse separation time of 25 ms. There is a significant suppression of the response at frequencies greater than $1/(2T)$. This can be understood by the fact that the phase shift arising from high-frequency vibrations will average out over the duration of the interrogation time $2T$. In the limit where $\omega \rightarrow 0$, equation (7.35) gives $H_a(\omega)(0) = 2k_2 T^2$. When the whole apparatus is accelerated with a component a_z along the Raman axis, the ratio of the interferometer phase to a_z is $(k_1 + k_2)T^2$. There is a difference of $(k_1 - k_2)T^2$ between these two transfer functions because the acceleration of the apparatus moves the fibre tip that launches the Raman beams as well as the mirror that reflects beam k_2 .

Measuring the Acceleration Noise Power Spectral Density of the Mirror

Even in a laboratory environment, acoustic vibrations are large enough that it is necessary to use of some mechanical isolation to reduce them. We employ two methods.

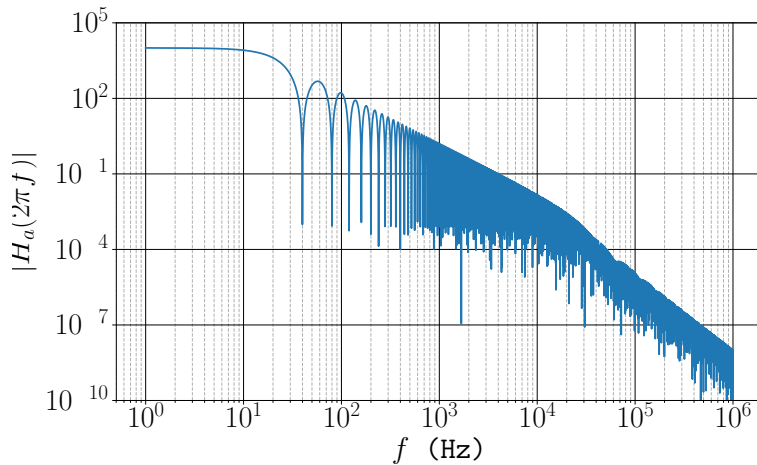


Figure 7.20: Acceleration noise transfer function. The parameters used here are the same as those previously defined for Figure 7.17.

Firstly, the apparatus sits on an optical table. Secondly, the vacuum chamber is mounted with a layer of Sorbothane placed between it and the optical table. The optical table is passively isolated from the ground using a pneumatic suspension system between the optical table and its supporting legs. This pneumatic suspension system can be easily switched off, so that the table sits hard on the legs. This makes it possible to compare the effect on the interferometer phase with both low and high levels of vibration.

Figure 7.21a shows a measurement of the MEMS accelerometer signal over a period of 1 s. The blue curve, which was obtained when the pneumatic suspension was disabled, shows significantly higher levels of vibration noise. The orange curve was obtained with the additional isolation and accordingly shows a quieter signal. An oscillation of the signal at 50 Hz is also apparent in both cases. This is characteristic of interference from other electrical sources and has since been reduced by isolating the power source of the MEMS accelerometer. Figure 7.21b shows the power spectral density of the MEMS accelerometer signal. There are clear peaks at 10 Hz, 50 Hz, 100 Hz, 200 Hz, 250 Hz and 700 Hz, which are reduced when the table is floated. The

50 Hz peak is of particular interest because it is also narrower, which indicates that the noise has been damped. This suggests that there is also acoustic noise originating from electro-mechanical devices driven by the 50 Hz mains line, as well as the previously mentioned electrical hum. One can see in Figure 7.21b that the pneumatic suspension mechanically filters the acceleration noise within the 6-200 Hz band, which is reduced by around a factor of 100. It is also clear that the low frequency acceleration noise is amplified by around a factor of 100^6 . This can be understood be the fact that the table is slowly oscillating under the pneumatic suspension. As the table tips, a component of gravitational acceleration is projected along the Raman axis. At frequencies above 1 kHz, it can be seen that there is no benefit from floating the optical table.

We calculate the corresponding interferometer phase power spectral density using $S_\Phi(\omega) = H_a(\omega)^2 S_a(\omega)$. Figure 7.21c shows this spectrum for a pulse separation time of $T = 25$ ms with and without the pneumatic suspension. The filtering of the noise within the 6-200 Hz band is also apparent here, as is the amplification of the low frequency noise.

The Allan deviation for the interferometer phase that results from mechanical vibrations is shown in Figure 7.22. This has been calculated by grouping the acceleration measurements into durations of 50 ms and integrating once to give $\frac{d\phi}{dt} = 2k_2 \int_{-T}^t a(t') dt'$, where $a(t')$ is the acceleration measured by the MEMS accelerometer at the time t' . The interferometer phase shift is then calculated using equation (7.24). Figure 7.22 shows the Allan deviation of the interferometer phase as calculated from the measured acceleration noise. For one measurement, we calculate an Allan deviation with the table floating of around 250 mrad and without the pneumatic support, that increases to 650 mrad. These are significantly larger than the other sources of noise discussed thus far. However, even up to $N = 10^3$, the acceleration noise remains

⁶Of course, there is less power within this band so the total noise is lower. This is shown in the acceleration time-series in Figure 7.21a.

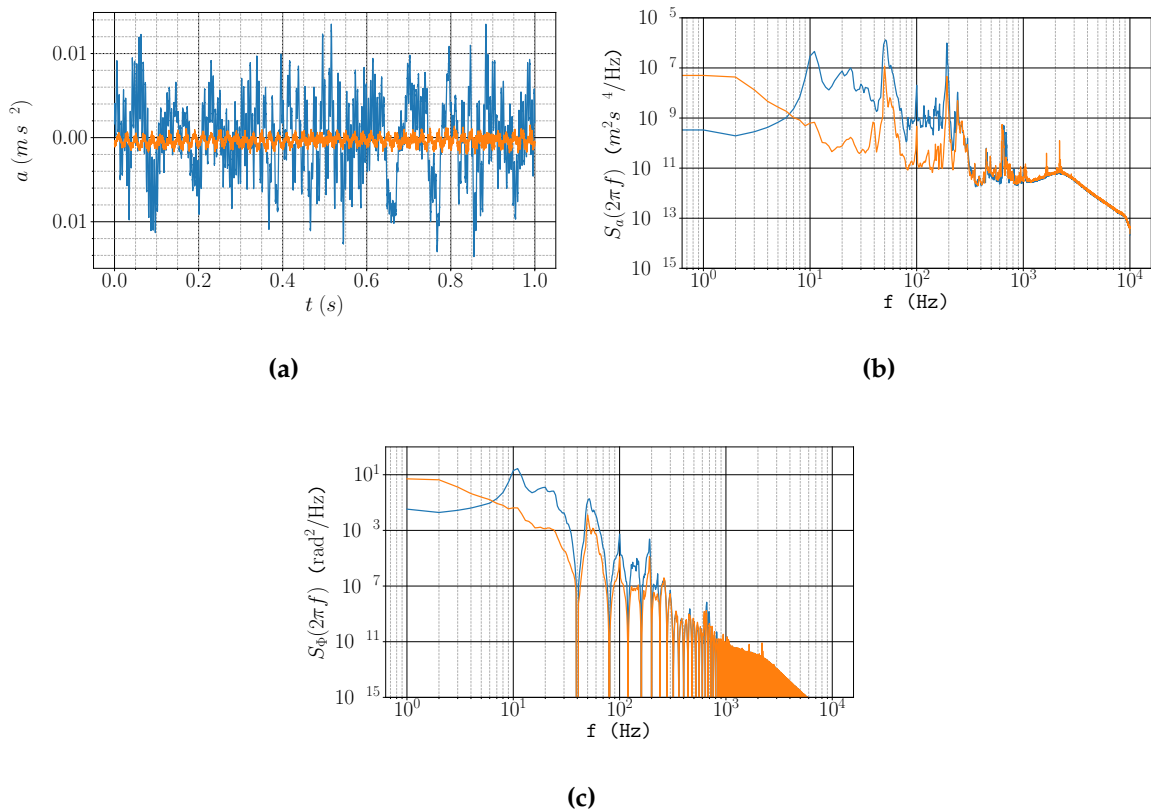


Figure 7.21: **a** Measured acceleration of the retro-reflecting mirror measured by the MEMS accelerometer. **b** Calculated power spectral density of the MEMS accelerometer. **c** Calculated interferometer phase power spectral density due to vibrations for an interferometer pulse separation of $T = 25$ ms. In each plot, the blue curves were taken without further isolation using pneumatic suspension (see text). The orange curves were obtained with this enabled.

uncorrelated and the Allan deviation exhibits a N^{-1} dependence⁷. Therefore, it is expected that the mechanical noise will be the dominant source of noise.

The vibration noise in our lab is likely much lower than on a moving vehicle such as a submarine. A sensitive, mobile sensor will therefore probably require a more sophisticated method of isolating the apparatus from external vibrations. For instance, active vibration isolation systems can be engineered to have a low natural frequency, on the order of 0.01 mHz [80]. An active isolator would substantially suppress vibration noise up to the interferometer phase bandwidth of $1/(2T)$ and enhance the sensitivity to the atoms' acceleration.

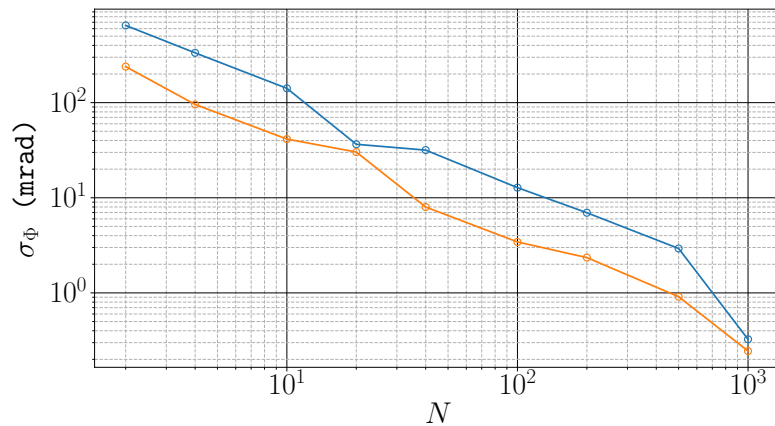


Figure 7.22: Calculated Allan deviation of the interferometer phase from vibration noise versus number of samples (each measurement lasts for 50 ms). As in Figure 7.21, the blue curve shows the high vibration noise case and the orange curve shows the low vibration noise case.

⁷It is possible that correlations at longer times may become apparent. For instance, the Earth's rotation could introduce acceleration noise at the tidal period of 12.4 h. The low-frequency band of the acceleration noise has not yet been investigated, but it is certainly worth doing so.

7.5.7 Summary of Identified Noise Sources

To conclude this discussion, it is worth summarising the sources of noise that have been presented. Table 7.3 shows the expected contributions from each of these sources to Allan deviation of the interferometer phase after 2 samples and 50 samples of the interferometer phase and the corresponding acceleration uncertainty for an interferometer pulse separation time of $T = 25\text{ ms}$. At a low number of samples, the largest contribution to the acceleration uncertainty comes from low-frequency oscillations of the optical table due to the pneumatic suspension. As mentioned above, an improvement to the vibration isolation system could reduce this. As the number of samples increases, we find that the contribution from each source decreases. However, it is not known if stronger correlations at longer times from vibrations or the laser phase may limit the sensitivity.

| Noise Source | 2 samples | | 50 samples | |
|---|----------------------|-------------------------------------|----------------------|-------------------------------------|
| | σ_Φ (mrad) | σ_a ($\mu\text{m s}^{-2}$) | σ_Φ (mrad) | σ_a ($\mu\text{m s}^{-2}$) |
| Projection noise (3×10^6 atoms) | 1 | 0.1 | 0.2 | 0.02 |
| Technical detector noise | 2 | 0.2 | 0.4 | 0.04 |
| Laser phase noise | 11 | 1.1 | 1.7 | 0.17 |
| Vibrations | 250 | 25 | 6.5 | 0.65 |

Table 7.3: Comparison of identified noise sources and their effects on acceleration measurements for a small and large number of samples. These values are estimated assuming a separation between pulses of $T = 25\text{ ms}$ and a $\pi/2$ pulse time of $\tau = 20\text{ }\mu\text{s}$. The projection noise assumes perfect fringe contrast.

Other effects can influence the interferometer phase. For instance, a magnetic field gradient over the region where the atoms move in free fall can produce a changing second-order Zeeman shift of the Rubidium-87 clock transition. Also, fluctuations in the intensity of the Raman beams can induce phase shifts through the ac Stark shift discussed in Section 7.4.2. It is expected that these have a smaller effect on the

acceleration sensitivity than the vibration noise and Raman phase noise, and have yet to be characterised. It is also worth noting that inertial effects, such as the Coriolis force and gravity gradients lead to higher-order contributions to the interferometer phase [81]. These effects are particularly relevant to inertial navigation, which relies on accurate measurements of the Earth's rotation and local gravitational field to determine the acceleration and rotation of a moving body. A characterisation of these effects on the interferometer will be required to improve its performance as an inertial sensor.

7.6 Measuring Accelerations

This section presents the technique used to characterise the atom interferometer and its sensitivity to accelerations. It begins with a calibration of the fringe pattern in Section 7.6.1. Following this, a method for subtracting the vibration-induced interferometer phase is given in Section 7.6.2. Finally, this section concludes with a measurement of the Allan deviation to examine the stability of the interferometer signal in Section 7.6.3.

7.6.1 Fringe Calibration

The presence of background atoms (in the $|F = 1, m_F = \pm 1\rangle$ states) and inhomogeneities in the Rabi frequency across the atom cloud mean that we do not observe a perfect interferometer fringe contrast. A simple way to map out the fringes is to scan the Raman phase of one of the pulses. Recalling from Section 7.5.5, the interferometer phase involves $-(\phi_0)_1 + 2(\phi_0)_2 - (\phi_0)_3$, where $-(\phi_0)_j$ is the Raman phase during the j -th pulse. Figure 7.23 shows an interference fringe obtained by varying $(\phi_0)_2$ for an interferometer pulse separation time of $T = 25$ ms. In this instance, the contrast is $C = 0.042(3)$ and the mean transition probability is $P_0 = 0.390(1)$. The fringe contrast is far smaller than the ideal case of $C = 1$. Since the acceleration uncertainty σ_a is inversely

proportional to the fringe contrast, we expect a quantum projection noise-limited value for a single measurement of $\frac{1}{C} 0.1 \mu\text{m s}^{-2} \approx 2.5 \mu\text{m s}^{-2}$. It should also be noted that the characteristic sinusoidal dependence of the quantum projection noise is not observed in the fringe pattern, since the vibration noise is dominant.

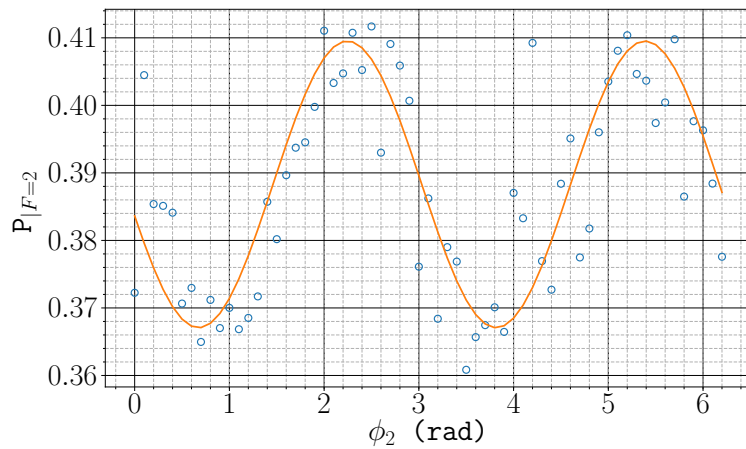


Figure 7.23: Interference fringe obtained by varying the phase difference of the two Raman lasers during the middle π pulse for a pulse separation time of $T = 25 \text{ ms}$. The orange curve is a non-linear least squares fit to the data, giving a contrast of $C = 0.042(3)$ and a mean transition probability of $P_0 = 0.390(1)$.

7.6.2 Comparing the atom accelerometer with the MEMS accelerometer

The MEMS accelerometer records an output voltage $V_m(t)$, corresponding to the (perpendicular) acceleration of the mirror $a_m(t) = KV_m(t)$, where $K = 0.793 \text{ m s}^{-2} \text{ V}^{-1}$ is the calibration factor. The integral of this gives the velocity of the mirror. Recalling equation (7.24), the corresponding interferometer phase is

$$\Phi_m = 2k_2 K \int_{-T}^T g(t) U_m(t) dt \quad (7.36)$$

where $U_m(t) = \int_{-T}^t V_m(t')dt'$ and $g(t)$ is the sensitivity function, defined in equation (7.25). As usual, we neglect τ compared with T . To test the validity of this, the interferometer transition probability $P_{|F=2\rangle}$ is fitted to the following form

$$P_{|F=2\rangle} = P_0 + \frac{C}{2} \sin(\kappa\Phi_m + \Phi_{\text{off}}) \quad (7.37)$$

A departure from $\kappa = 1$ would indicate a scaling error in converting from the MEMS accelerometer voltage to the interferometer phase. A departure from $\Phi_{\text{off}} = 0$ would indicate a difference between the two due to a zero error or to noise. A zero error would show up as a constant offset, whereas noise would appear in the residuals of the fit to equation (7.37). The plot in Figure 7.24a shows the measured value of $P_{|F=2\rangle}$ versus Φ_m . One sees that the interferometer phase is swept over roughly two radians by the ambient acceleration noise and drift. The orange curve is a fit to equation (7.37), with $P_0 = 0.348$, $C = 0.05$, $\kappa = 0.95$ and $\Phi_{\text{off}} = 0.24$ rad. The fact that κ differs from 1 is explained by the resistor used to convert the current generated by the MEMS to a voltage. The value of K assumed the nominal resistance of $10\text{ k}\Omega$, but a subsequent measurement confirmed that it was typically off by 5%. It was then replaced with a $6\text{ k}\Omega$ precision resistor with a measured value of $6000.11\text{ }\Omega$ and the discrepancy was removed. The value of $\Phi_{\text{off}} = 0.24$ rad corresponds to a bias (zero offset) of $24\text{ }\mu\text{m s}^{-2}$. Given that the MEMS accelerometer specifications cite a bias of 21 mm s^{-2} at room temperature, with a temperature coefficient of $82\text{ }\mu\text{m s}^{-2}\text{ K}^{-1}$, it is almost certain that Φ_{off} is simply due to that. Indeed, it is expected that the atom interferometer will have negligible bias and that it may be of most use in correcting the bias of a conventional accelerometer in a hybrid arrangement.

We turn now to the noise. The blue histogram in Figure 7.24b shows the distribution of accelerations inferred from the data points in Figure 7.24a. There are inferred without reference to the MEMS accelerometer, except that we use the fitted orange curve to

convert the measured values of $P_{|F=2\rangle}$ into values of acceleration a . These therefore include the noise due to ambient vibrations. By contrast, the green histogram shows the residuals of the fit to Figure 7.24a, measured along the abscissa, which give the acceleration noise after subtracting the MEMS accelerometer reading. This narrower distribution shows that the MEMS accelerometer is able to remove at least some of the vibration noise. The dashed lines indicate fitted Normal distributions for which the respective standard deviations of the acceleration are $\sigma_a^{(i)} = 55 \mu\text{m s}^{-2}$ and $\sigma_a^{(v)} = 27 \mu\text{m s}^{-2}$. If the vibration-induced phase noise were perfectly rejected, we would expect to reach an uncertainty on the order of $\sigma_a = 3 \mu\text{m s}^{-2}$, coming roughly equally from the Raman phase noise and quantum projection noise. The actual uncertainty is much greater than this because the MEMS accelerometer is specified to have an intrinsic noise level of $< 30 \mu\text{m s}^{-2}$ in the 0-20 Hz ($1/2T$) band. The agreement between this expectation and our experimental result shows that the additional noise from the atom interferometer is indeed small, as expected.

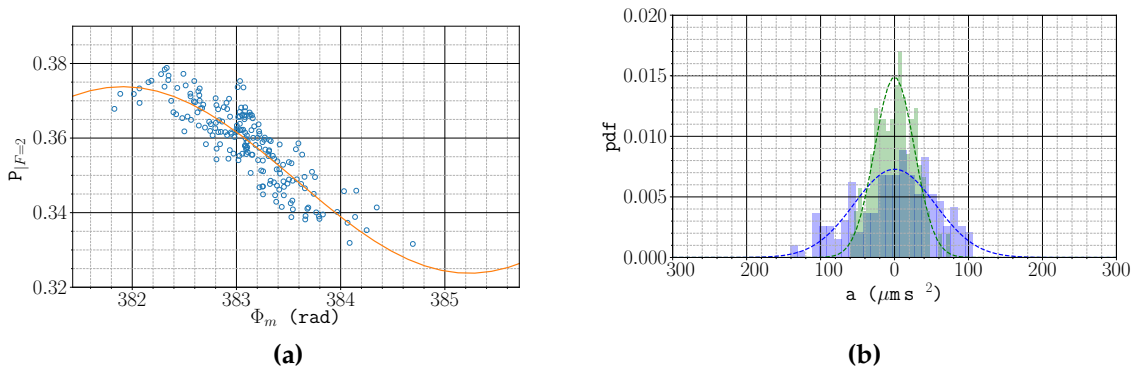


Figure 7.24: (a) Single interferometer readings plotted against the interferometer phase as inferred from the MEMS accelerometer. The laser table is floating. (b) Histogram of measured acceleration noise. The blue points show the spread of accelerations without reference to the MEMS accelerometer. These include vibration noise. The green points show the noise in the difference between the MEMS and atom accelerometers. The vibration noise is suppressed to the noise level of the MEMS accelerometer. The dashed lines are fitted Normal distributions.

Figure 7.25 shows a repeat of this experiment without floating the laser table. In this case, the vibrations give a standard deviation of acceleration of $460 \mu\text{m s}^{-2}$, but after subtracting the MEMS accelerometer reading, this collapses to $29 \mu\text{m s}^{-2}$, limited once again by the noise floor of the MEMS accelerometer.

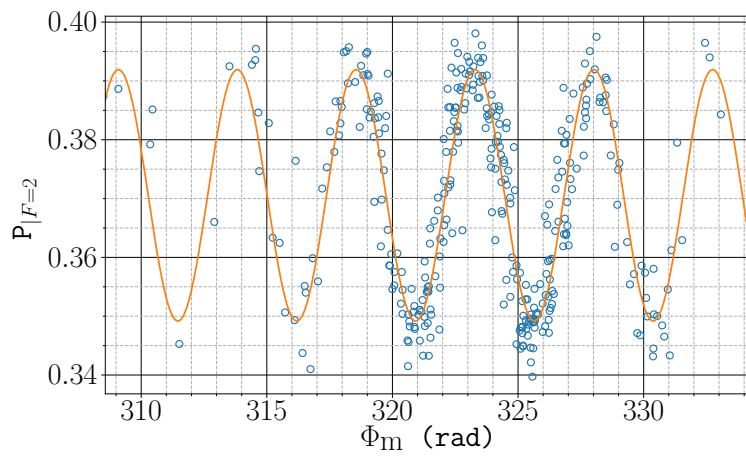


Figure 7.25: Single interferometer readings plotted against the interferometer phase inferred from the MEMS accelerometer, when the table is grounded.

7.6.3 Expected vs observed Allan deviation

Figure 7.26 shows the Allan deviation of the interferometer phase derived from a set of 200 interferometer measurements. The orange curve shows the noise as measured from the transition probability alone whereas the blue curve shows the noise remaining after subtracting the acceleration measured by the MEMS accelerometer, as discussed in the previous section. In both cases, the Allan deviation shows the $N^{-1/2}$ dependence that is characteristic of uncorrelated noise. The blue and orange dashed lines correspond to deviations of $0.21 \text{ rad } N^{-1/2}$ and $0.4 \text{ rad } N^{-1/2}$, respectively. Because these measurements were spaced by 800 ms, these correspond to sensitivities of around $40 \mu\text{m s}^{-2} \text{ Hz}^{-1/2}$ and $20 \mu\text{m s}^{-2} \text{ Hz}^{-1/2}$. These figures will be improved in the future, simply by increasing the repetition rate to 10 shots per second. The black

dashed line shows the interferometer phase expected from the Raman phase noise, shown previously in Figure 7.19, and the orange dotted line shows the phase noise due to vibrations shown previously in Figure 7.22. It appears that after subtracting the acceleration measured by the MEMS, the Allan deviation of the interferometer phase is limited by the intrinsic noise of the MEMS. After 50 measurements (40 s), the interferometer reaches a sensitivity to acceleration of $3 \mu\text{m s}^{-2}$. This is far greater than the current state-of-the-art ($3 \times 10^{-12} \text{ m s}^{-2}$ after 5 s reported in [60]) but given that the first generation gravimeter reached a sensitivity of $3 \times 10^{-5} \text{ m s}^{-2}$ after 1000 s [5], it is anticipated that the sensitivity will be enhanced in the future. It is also worth mentioning that the calculated contribution from the Raman phase noise may be too high because we did not allow any dead time between sequential determinations of the interferometer phase, whereas the real measurements are 800 ms apart. This may result in less noise than calculated⁸ because there is less opportunity for aliasing of the high-frequency noise.

7.7 Conclusion

This chapter has described the methods used to observe matter-wave interference and determine the acceleration from the measured transition probability. We have seen that the presence of background atoms in $m_F = \pm 1$ reduces the contrast of the interferometer. We have seen that mechanical vibrations contribute a dominant amount of noise at short averaging times, even with a Sorbothane mount on a floating laser table. An improvement of the vibration isolation system is underway to improve

⁸In the context of atomic clocks, this phenomenon is known as the Dick effect [85].

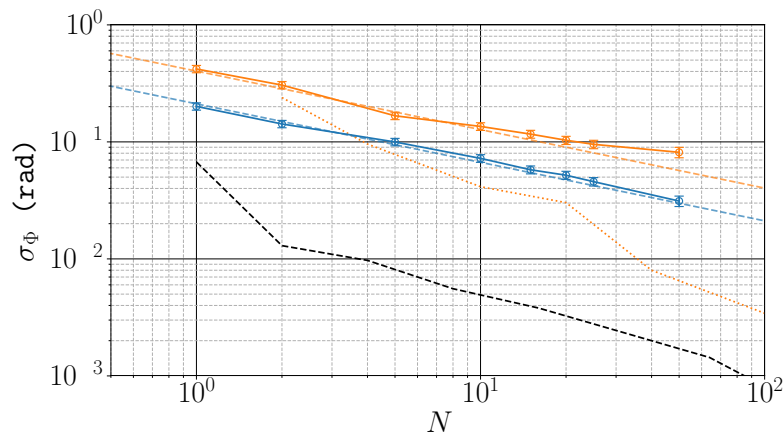


Figure 7.26: Allan deviation of the interferometer phase with floating table. Orange curve: measured deviation including vibrations. Blue curve: measured deviation after subtracting MEMS accelerometer reading, where the uncertainty is dominated by the noise floor of the MEMS. Orange dotted line: Allan deviation expected from vibration noise. Orange dashed line: $N^{-1/2}$ scaling before subtracting vibrations. Blue dashed line: $N^{-1/2}$ scaling after subtracting vibrations. Black dashed line: contribution from Raman phase noise.

the short-term sensitivity. It is also planned to improve the Raman phase noise so that the sensitivity can approach the limit set by the projection noise.

Chapter 8

Outlook

8.1 Conclusions

This project set out to develop an atom interferometer that could be suitable for inertial navigation. The specific aim was to build a device and demonstrate sensitivity to horizontal accelerations where gravitational acceleration acts perpendicularly to the sensitive axis. Requirements for a high measurement bandwidth and low dead time influenced the development of the experiment. The project was a team effort in which my particular tasks were to design, build and programme the computer control systems and to control the whole complex apparatus through a user interface. I was also responsible for characterising and understanding the various sources of noise in the device.

The dead time between measurements is reduced by loading the atoms from a 2D MOT and through an improved design of the control software. Using a 2D MOT reduces the time required to load a sufficient number of atoms when compared to loading from a background vapour. The hardware that controls the experiment regenerates

the necessary voltage patterns, removing the need for additional time to re-calculate the experimental sequence. This made it possible to load 10^8 atoms into the 3D MOT after 100 ms. With a maximum interrogation time of $2T = 50$ ms, the interferometer can currently be operated up to a rate of 4 Hz, which corresponds to a duty cycle of 20%. With further optimisation of the 2D MOT system, such as increased cooling beam power, it will be possible to increase the atomic flux and hence increase the experiment cycling rate.

The design of the in-vacuum optical system for the interferometer light pulses ensures that the fringe visibility is not lost due to transverse motion of the atoms. Wavefront distortions of the interferometer light pulses are minimised by not requiring optical viewports between the Raman laser and the atoms. The beams are also collimated to a large waist size to reduce dephasing of the atoms from an intensity gradient. A beam waist of at least 34 mm necessitated an aspheric lens pair in the collimation optics train. These lenses are not manufactured to the same optical quality as the triplet lens. It was found that they introduced an irregular intensity distribution of the laser which led to dephasing of the atomic states. An improved optical system has been designed by Shane de Souza, the latest student on this experiment. It is anticipated that this will improve the wavefront quality for the interferometer light pulses.

The sequence of optical and microwave pulses that prepares atoms in the $|1, 0\rangle$ state is very effective at increasing the population in the $m_F = 0$ state beyond the fraction expected after an optical molasses. Despite this, there remains a residual population in the $|1, \pm 1\rangle$ states. These are detected as a background, which reduces the interferometer fringe contrast. Since preparing this thesis, the state preparation sequence has been improved by increasing the polarisation purity of the light driving the $|F = 1\rangle \rightarrow |F' = 0\rangle$ transition. There is now less de-population of the $|1, 0\rangle$ state due to π -transitions.

It has been possible to observe interference with a fringe contrast of around 5%. This admittedly low value is likely due to the reasons stated above. In fact, since reducing the $|1, \pm 1\rangle$ population, the fringe contrast has increased to around 20%. Further details of this can be found in Xiaxi Cheng's PhD thesis [88].

The sensitivity to horizontal accelerations was demonstrated by comparing the interferometer signal in differing levels of vibration noise. This also highlighted the importance of vibration isolation for accurate acceleration measurements. A study has been made of a hybrid system in which the atom interferometer works together with a MEMS accelerometer. Using this, we have been able to reach a sensitivity to acceleration of $3 \mu\text{m}^{-2}$ after an integration time of 40 s. This will be particularly important in a high-vibration environment where the classical accelerometer can identify the order number of the atom interferometer fringe.

8.2 Avenues of Further Research

Although this work represents the first step towards inertial navigation using atom interferometry, there is still more to be done. The bias is one area to study. It is believed that the interferometer will have exceedingly low bias and that its main role might be to correct the bias of an associated conventional accelerometer. This is important as any bias can result in significant position error at long times. When navigating on the surface of the Earth, there is a feedback mechanism which partially corrects for bias and leads to Schuler oscillations [89]. Nevertheless, it is desirable to have no bias and that seems possible with atom interferometry. Further work is planned to extend this system to measure accelerations along 3 axes. This requires a modification of the Raman laser system so that it can provide enough power from three outputs. It will be important to have good control over the orientation of the accelerometer.

A comparison of the interferometer with conventional accelerometers will greatly benefit research aimed towards practical applications of atom interferometry. This has already been demonstrated in the context of gravimeters [90,91], where a mobile atomic system has demonstrated greater insensitivity to vibration noise and better short-term stability than the state-of-the-art classical counterpart. Additionally, this interferometer has yet to be tested outside of a laboratory environment. As a first step in that direction, it was demonstrated at the UK National Quantum Technologies Showcase in November 2018 in the Queen Elizabeth II conference centre (see Figure 8.1), where it operated in a normal room in the presence of 800 people and a large fluctuating ambient magnetic field. A recent experiment has investigated the bias stability of a hybrid sensor in a simulated harsh environment [92].

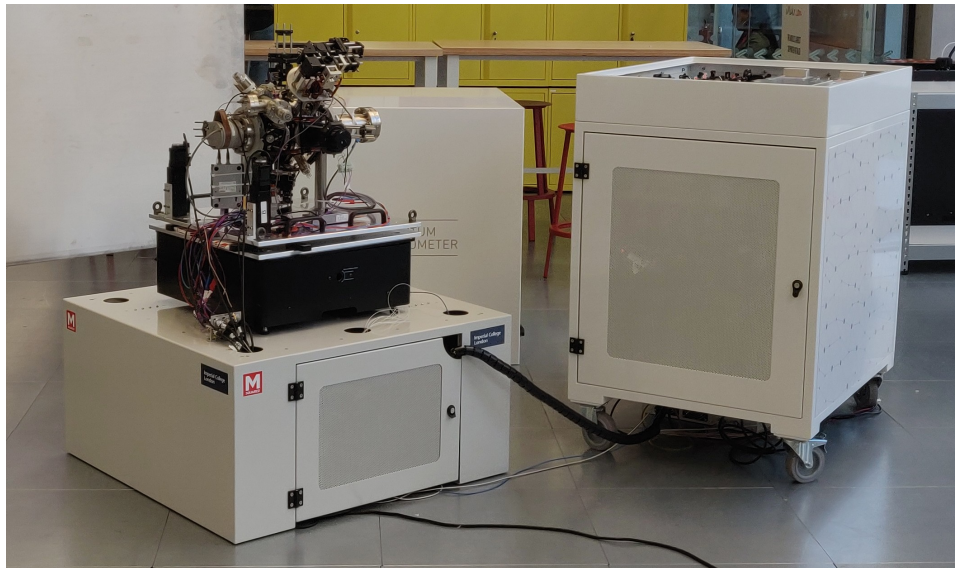


Figure 8.1: Demonstration of the atom interferometer as a mobile sensor of a range of horizontal accelerations at the UK National Quantum Technologies Showcase in November 2018.

8.3 Concluding Remarks

The application of newly understood physics has often led to the development of more advanced technology. In turn, this has contributed to further progress in scientific disciplines, and society in general. This describes well the present effort to use matter-wave interferometry for inertial sensing. There already exists a significant body of research that demonstrates the technical feasibility of measuring inertial forces using cold atomic systems. In addition, the practical requirements for navigation have served to identify a need for the unique benefits of atom interferometers. The work presented in this thesis has helped to address this need. It is anticipated that the application of quantum mechanics to technology will bring practical benefits as well as enable a deeper understanding of physical phenomena.

Bibliography

- [1] L. ESSEN and J. V. L. PARRY, “An Atomic Standard of Frequency and Time Interval: A Cæsium Resonator”, *Nature* **176** (Aug, 1955) 280–282,
[doi:10.1038/176280a0](https://doi.org/10.1038/176280a0).
- [2] J. Levine and T. Parker, “The algorithm used to realize UTC(NIST)”, in *Proceedings of the 2002 IEEE International Frequency Control Symposium and PDA Exhibition (Cat. No.02CH37234)*, pp. 537–542. IEEE.
[doi:10.1109/FREQ.2002.1075941](https://doi.org/10.1109/FREQ.2002.1075941).
- [3] J. Clauser, “Ultra-High Sensitivity Accelerometers And Gyroscopes Using Neutral Atom Matter-Wave Interferometry”, *Physica B+ C* **151** (1988) 262–272.
- [4] C. Bordé, “Atomic interferometry with internal state labelling”, *Physics Letters A* **140** (Sep, 1989) 10–12, [doi:10.1016/0375-9601\(89\)90537-9](https://doi.org/10.1016/0375-9601(89)90537-9).
- [5] M. Kasevich and S. Chu, “Atomic Interferometry Using Stimulated Raman Transitions”, *Physical Review Letters* **67** (Mar, 1991) 181–184,
[doi:10.1097/01.NUMA.0000442649.24195.3c](https://doi.org/10.1097/01.NUMA.0000442649.24195.3c).
- [6] M. Kasevich and S. Chu, “Measurement of the Gravitational Acceleration of an Atom with a Light-Pulse Atom Interferometer”, *Applied Physics B* **332** (1992) 321–332.
- [7] D. S. Durfee, Y. K. Shaham, and M. A. Kasevich, “Long-Term Stability of an Area-Reversible Atom-Interferometer Sagnac Gyroscope”, *Physical Review Letters* **97** (Dec, 2006) 240801, [doi:10.1103/PhysRevLett.97.240801](https://doi.org/10.1103/PhysRevLett.97.240801).
- [8] B. Dubetsky and M. Kasevich, “Atom interferometer as a selective sensor of rotation or gravity”, *Physical Review A* **74** (Aug, 2006) 023615,
[doi:10.1103/PhysRevA.74.023615](https://doi.org/10.1103/PhysRevA.74.023615).
- [9] C. J. Borde, “Atomic clocks and inertial sensors”, *Metrologia* **39** (2002), no. 5,

- 435–463, doi:[10.1088/0026-1394/39/5/5](https://doi.org/10.1088/0026-1394/39/5/5).
- [10] B. Barrett, P. a. Gominet, E. Cantin et al., “Mobile and remote inertial sensing with atom interferometers”, *Proceedings of the International School of Physics “Enrico Fermi”*, Vol 188 (2013) doi:[10.3254/978-1-61499-448-0-493](https://doi.org/10.3254/978-1-61499-448-0-493), arXiv:[1311.7033](https://arxiv.org/abs/1311.7033).
 - [11] R. Nyman, G. Varoquaux, F. Lienhart et al., “I.C.E.: a transportable atomic inertial sensor for test in microgravity”, *Applied Physics B* **84** (Aug, 2006) 673–681, doi:[10.1007/s00340-006-2395-7](https://doi.org/10.1007/s00340-006-2395-7).
 - [12] R. Geiger, V. Ménoret, G. Stern et al., “Detecting inertial effects with airborne matter-wave interferometry.”, *Nature communications* **2** (Jan, 2011) 474, doi:[10.1038/ncomms1479](https://doi.org/10.1038/ncomms1479).
 - [13] F. A. Faruqi and K. J. Turner, “Extended Kalman filter synthesis for integrated global positioning/inertial navigation systems”, *Applied Mathematics and Computation* **115** (Oct, 2000) 213–227, doi:[10.1016/S0096-3003\(98\)10068-1](https://doi.org/10.1016/S0096-3003(98)10068-1).
 - [14] K. Wen, C. K. Seow, and S. Y. Tan, “Inertial navigation system positioning error analysis and Cramér-Rao lower bound”, in *2016 IEEE/ION Position, Location and Navigation Symposium (PLANS)*, pp. 213–218. IEEE, Apr, 2016. doi:[10.1109/PLANS.2016.7479704](https://doi.org/10.1109/PLANS.2016.7479704).
 - [15] A. V. Rakholia, H. J. McGuinness, and G. W. Biedermann, “Dual-axis, high data-rate atom interferometer via cold ensemble exchange”, arXiv:[1407.3847](https://arxiv.org/abs/1407.3847).
 - [16] G. W. Biedermann, H. J. McGuinness, A. V. Rakholia et al., “Atom Interferometry in a Warm Vapor”, *Physical Review Letters* **118** (Apr, 2017) 163601, doi:[10.1103/PhysRevLett.118.163601](https://doi.org/10.1103/PhysRevLett.118.163601).
 - [17] C. Jekeli, “Navigation Error Analysis of Atom Interferometer Inertial Sensor”, *Navigation* **52** (Mar, 2005) 1–14, doi:[10.1002/j.2161-4296.2005.tb01726.x](https://doi.org/10.1002/j.2161-4296.2005.tb01726.x).
 - [18] I. Dutta, D. Savoie, B. Fang et al., “Continuous Cold-Atom Inertial Sensor with 1 nrad/sec Rotation Stability”, *Physical Review Letters* **116** (may, 2016) 183003, doi:[10.1103/PhysRevLett.116.183003](https://doi.org/10.1103/PhysRevLett.116.183003).
 - [19] S. Merlet, J. Le Gouët, Q. Bodart et al., “Operating an atom interferometer beyond its linear range”, *Metrologia* **46** (Feb, 2009) 87–94, doi:[10.1088/0026-1394/46/1/011](https://doi.org/10.1088/0026-1394/46/1/011).

- [20] J. Lautier, L. Volodimer, T. Hardin et al., "Hybridizing matter-wave and classical accelerometers", *Applied Physics Letters* **105** (Oct, 2014) 144102, [doi:10.1063/1.4897358](https://doi.org/10.1063/1.4897358).
- [21] S. Dimopoulos, P. Graham, J. Hogan et al., "Atomic gravitational wave interferometric sensor", *Physical Review D* **78** (Dec, 2008) 122002, [doi:10.1103/PhysRevD.78.122002](https://doi.org/10.1103/PhysRevD.78.122002).
- [22] "IEEE Standard Specification Format Guide and Test Procedure for Linear, Single-Axis, Non-Gyroscopic Accelerometers", *IEEE Std 1293-1998 (R2008)* (2011) 1–249, [doi:10.1109/IEEESTD.2011.5960745](https://doi.org/10.1109/IEEESTD.2011.5960745).
- [23] G. Grynberg, A. Aspect, and C. Fabre, "Introduction to Quantum Optics: From the Semi-Classical Approach to Quantized Light", *Contemporary Physics* (Nov, 2011) 45–106, [doi:10.1080/00107514.2011.604134](https://doi.org/10.1080/00107514.2011.604134).
- [24] H. Metcalf and P. V. D. Straten, "Laser cooling and trapping of atoms", *JOSA B* (2003).
- [25] Y. Wu, "Effective Raman theory for a three-level atom in the Λ configuration", *Physical Review A - Atomic, Molecular, and Optical Physics* **54** (1996), no. 2, 1586–1592, [doi:10.1103/PhysRevA.54.1586](https://doi.org/10.1103/PhysRevA.54.1586).
- [26] P. R Berman, "Atom Interferometry". 1997.
- [27] P. Storey and C. Cohen-Tannoudji, "The Feynman path integral approach to atomic interferometry. A tutorial", *Journal de Physique II* (1994).
- [28] D. S. Weiss, B. C. Young, and S. Chu, "Precision measurement of \hbar/m Cs based on photon recoil using laser-cooled atoms and atomic interferometry", *Applied Physics B Lasers and Optics* **59** (Sep, 1994) 217–256, [doi:10.1007/BF01081393](https://doi.org/10.1007/BF01081393).
- [29] R. Han, H. K. Ng, and B.-G. Englert, "Raman transitions without adiabatic elimination: A simple and accurate treatment", *Journal of Modern Optics* **60** (sep, 2012) 17, [arXiv:1209.6569](https://arxiv.org/abs/1209.6569).
- [30] N. F. Ramsey, "A Molecular Beam Resonance Method with Separated Oscillating Fields", *Physical Review* **78** (Jun, 1950) 695–699, [doi:10.1103/PhysRev.78.695](https://doi.org/10.1103/PhysRev.78.695).
- [31] D. M. Brink and G. R. Satchler, "Matrix Elements of Tensor Operators", in *Angular Momentum*, pp. 56–60. 1968.

- [32] D. Steck, “Rubidium 87 D Line Data”,
- [33] A. Gauguet, B. Canuel, T. Lévèque et al., “Characterization and limits of a cold-atom Sagnac interferometer”, *Physical Review A* **80** (Dec, 2009) 063604, [doi:10.1103/PhysRevA.80.063604](https://doi.org/10.1103/PhysRevA.80.063604).
- [34] A. Keshet and W. Ketterle, “A Distributed GUI-based Computer Control System for Atomic Physics Experiments”, [doi:10.1063/1.4773536](https://doi.org/10.1063/1.4773536), [arXiv:1208.2607](https://arxiv.org/abs/1208.2607).
- [35] K. Dieckmann, R. J. C. Spreeuw, M. Weidemüller et al., “Two-dimensional magneto-optical trap as a source of slow atoms”, *Physical Review A* **58** (Nov, 1998) 3891–3895, [doi:10.1103/PhysRevA.58.3891](https://doi.org/10.1103/PhysRevA.58.3891).
- [36] T. Müller, T. Wendrich, M. Gilowski et al., “Versatile compact atomic source for high-resolution dual atom interferometry”, *Physical Review A* **76** (Dec, 2007) 063611, [doi:10.1103/PhysRevA.76.063611](https://doi.org/10.1103/PhysRevA.76.063611).
- [37] C. Roos, P. Cren, J. Dalibard et al., “A Source of Cold Atoms for a Continuously Loaded Magnetic Guide”, *Physica Scripta* **T105** (2003), no. 1, 19, [doi:10.1238/Physica.Topical.105a00019](https://doi.org/10.1238/Physica.Topical.105a00019).
- [38] E. L. Raab, M. Prentiss, A. Cable et al., “Trapping of Neutral Sodium Atoms with Radiation Pressure”, *Physical Review Letters* **59** (Dec, 1987) 2631–2634, [doi:10.1103/PhysRevLett.59.2631](https://doi.org/10.1103/PhysRevLett.59.2631).
- [39] “μQuans Laser System Specifications”.
- [40] V. Ménoret, R. Geiger, G. Stern et al., “Dual-wavelength laser source for onboard atom interferometry”, *Optics Letters* **36** (Nov, 2011) 4128, [doi:10.1364/OL.36.004128](https://doi.org/10.1364/OL.36.004128).
- [41] T. Lévèque, L. Antoni-Micollier, B. Faure et al., “A laser setup for rubidium cooling dedicated to space applications”, *Applied Physics B* **116** (Sep, 2014) 997–1004, [doi:10.1007/s00340-014-5788-z](https://doi.org/10.1007/s00340-014-5788-z), [arXiv:1309.2075](https://arxiv.org/abs/1309.2075).
- [42] J. M. Supplee, E. A. Whittaker, and W. Lenth, “Theoretical description of frequency modulation and wavelength modulation spectroscopy”, *Applied Optics* **33** (Sep, 1994) 6294, [doi:10.1364/AO.33.006294](https://doi.org/10.1364/AO.33.006294).
- [43] A. M. A. Steane, M. Chowdhury, and C. J. Foot, “Radiation force in the magneto-optical trap”, *Journal of the Optical Society of America B* **9** (dec, 1992) 2142, [doi:10.1364/JOSAB.9.002142](https://doi.org/10.1364/JOSAB.9.002142).

- [44] C. J. Dedman, K. G. H. Baldwin, and M. Colla, “Fast switching of magnetic fields in a magneto-optic trap”, *Review of Scientific Instruments* **72** (2001), no. 11, 4055–4058, [doi:10.1063/1.1408935](https://doi.org/10.1063/1.1408935).
- [45] M. Haw, N. Evetts, W. Gunton et al., “Magneto-optical trap loading rate dependence on trap depth and vapor density”, *Journal of the Optical Society of America B* **29** (Feb, 2012) 475, [doi:10.1364/JOSAB.29.000475](https://doi.org/10.1364/JOSAB.29.000475).
- [46] M. Prentiss, E. L. Raab, D. E. Pritchard et al., “Atomic-density-dependent losses in an optical trap”, *Optics Letters* **13** (Jun, 1988) 452, [doi:10.1364/OL.13.000452](https://doi.org/10.1364/OL.13.000452).
- [47] C. Salomon, J. Dalibard, W. D. Phillips et al., “Laser Cooling of Cesium Atoms Below 3 μK ”, *Europhysics Letters (EPL)* **12** (Aug, 1990) 683–688, [doi:10.1209/0295-5075/12/8/003](https://doi.org/10.1209/0295-5075/12/8/003).
- [48] J. Dalibard and C. Cohen-Tannoudji, “Laser cooling below the Doppler limit by polarization gradients: simple theoretical models”, *Journal of the Optical Society of America B* **6** (Nov, 1989) 2023, [doi:10.1364/JOSAB.6.002023](https://doi.org/10.1364/JOSAB.6.002023).
- [49] K. Berg-Sørensen, Y. Castin, E. Bonderup et al., “Momentum Diffusion of Atoms Moving in Laser Fields”, *Journal of Physics B: Atomic, Molecular and Optical Physics* **25** (1992), no. 20, 4195–4215, [doi:10.1088/0953-4075/25/20/016](https://doi.org/10.1088/0953-4075/25/20/016).
- [50] K. Molmer, “Atomic momentum diffusion in a σ^+ - σ^- laser configuration: influence of an internal sublevel structure”, *Journal of Physics B: Atomic, Molecular and Optical Physics* **23** (1990), no. 22, 4101–4110, [doi:10.1088/0953-4075/23/22/012](https://doi.org/10.1088/0953-4075/23/22/012).
- [51] S.-i. Ohshima, T. Kurosu, T. Ikegami et al., “Cesium Atomic Fountain with Two-Dimensional Moving Molasses”, *Japanese Journal of Applied Physics* **34** (Sep, 1995) L1170–L1173, [doi:10.1143/JJAP.34.L1170](https://doi.org/10.1143/JJAP.34.L1170).
- [52] P. van der Straten, S.-Q. Shang, B. Sheehy et al., “Laser cooling at low intensity in a strong magnetic field”, *Phys. Rev. A* **47** (1993), no. 5, 4160–4175, [doi:10.1103/PhysRevA.47.4160](https://doi.org/10.1103/PhysRevA.47.4160).
- [53] S. Chang, T. Y. Kwon, H. S. Lee et al., “Laser sub-Doppler cooling of atoms in an arbitrarily directed magnetic field”, *Physical Review A - Atomic, Molecular, and Optical Physics* **66** (2002), no. 4, 23, [doi:10.1103/PhysRevA.66.043404](https://doi.org/10.1103/PhysRevA.66.043404).

- [54] M. Walhout, J. Dalibard, S. L. Rolston et al., “ $\sigma^+ - \sigma^-$ Optical molasses in a longitudinal magnetic field”, *Journal of the Optical Society of America B* **9** (Nov, 1992) [doi:10.1364/JOSAB.9.001997](https://doi.org/10.1364/JOSAB.9.001997).
- [55] D. J. Berkeland and M. G. Boshier, “Destabilization of dark states and optical spectroscopy in Zeeman-degenerate atomic systems”, *Physical Review A* **65** (Feb, 2002) 033413, [doi:10.1103/PhysRevA.65.033413](https://doi.org/10.1103/PhysRevA.65.033413).
- [56] M. Kasevich, D. S. Weiss, E. Riis et al., “Atomic velocity selection using stimulated Raman transitions”, *Physical Review Letters* **66** (May, 1991) 2297–2300, [doi:10.1103/PhysRevLett.66.2297](https://doi.org/10.1103/PhysRevLett.66.2297).
- [57] T. H. Kim, S. H. Yim, K. M. Shim et al., “Spatial-contrast analysis in a cold-atom Sagnac interferometer with a single large Raman beam”, *Physical Review A* **95** (2017), no. 3, 1–6, [doi:10.1103/PhysRevA.95.033632](https://doi.org/10.1103/PhysRevA.95.033632).
- [58] J. A. Nelder and R. Mead, “A Simplex Method for Function Minimization”, *The Computer Journal* **7** (Jan, 1965) 308–313, [doi:10.1093/comjnl/7.4.308](https://doi.org/10.1093/comjnl/7.4.308).
- [59] R. Zhang and F. Shi, “A Novel Algorithm for Fiber-Optic Alignment Automation”, *IEEE Transactions on Advanced Packaging* **27** (Feb, 2004) 173–178, [doi:10.1109/TADVP.2004.825434](https://doi.org/10.1109/TADVP.2004.825434).
- [60] B. Barrett, L. Antoni-Micollier, L. Chichez et al., “Dual matter-wave inertial sensors in weightlessness”, *Nature Communications* **7** (2016) [doi:10.1038/ncomms13786](https://doi.org/10.1038/ncomms13786), [arXiv:1609.03598](https://arxiv.org/abs/1609.03598).
- [61] S. Foote and D. Grindeland, “Model QA3000 Q-Flex accelerometer high performance test results”, *IEEE Aerospace and Electronic Systems Magazine* **7** (Jun, 1992) 59–67, [doi:10.1109/62.145120](https://doi.org/10.1109/62.145120).
- [62] A. Lawrence, “The Pendulous Accelerometer”, pp. 57–71. 1998.
- [63] A. Lawrence, “Modern Inertial Technology”. Mechanical Engineering Series. Springer New York, New York, NY, 1998.
- [64] J. Lautier, M. Lours, and a. Landragin, “A compact micro-wave synthesizer for transportable cold-atom interferometers”, *Review of Scientific Instruments* **85** (2014), no. 6, [doi:10.1063/1.4884338](https://doi.org/10.1063/1.4884338), [arXiv:1406.2911](https://arxiv.org/abs/1406.2911).
- [65] A. M. Marino and C. R. Stroud, “Phase-locked laser system for use in atomic coherence experiments.”, *The Review of scientific instruments* **79** (Jan, 2008)

- 013104, [doi:10.1063/1.2823330](https://doi.org/10.1063/1.2823330).
- [66] R. W. P. Drever, J. L. Hall, F. V. Kowalski et al., "Laser phase and frequency stabilization using an optical resonator", *Applied Physics B Photophysics and Laser Chemistry* **31** (Jun, 1983) 97–105, [doi:10.1007/BF00702605](https://doi.org/10.1007/BF00702605).
- [67] J. J. . Bollinger, W. M. Itano, D. J. Wineland et al., "Optimal frequency measurements with maximally correlated states", *Physical Review A* **54** (Dec, 1996) R4649–R4652, [doi:10.1103/PhysRevA.54.R4649](https://doi.org/10.1103/PhysRevA.54.R4649).
- [68] A. Gauguet, T. E. Mehlstäubler, T. Lévèque et al., "Off-resonant Raman transition impact in an atom interferometer", *Physical Review A* **78** (Oct, 2008) 043615, [doi:10.1103/PhysRevA.78.043615](https://doi.org/10.1103/PhysRevA.78.043615), [arXiv:0809.0149](https://arxiv.org/abs/0809.0149).
- [69] K. Moler, D. Weiss, M. Kasevich et al., "Theoretical Analysis of Velocity-Selective Raman Transitions", *Physical Review A* **45** (1992), no. 1, 342–348.
- [70] E. Rocco, R. N. Palmer, T. Valenzuela et al., "Fluorescence detection at the atom shot noise limit for atom interferometry", *New Journal of Physics* **16** (sep, 2014) 093046, [doi:10.1088/1367-2630/16/9/093046](https://doi.org/10.1088/1367-2630/16/9/093046).
- [71] R. M. Howard, "Principles of Random Signal Analysis and Low Noise Design". 2002.
- [72] P. Welch, "The use of fast Fourier transform for the estimation of power spectra: A method based on time averaging over short, modified periodograms", *IEEE Transactions on Audio and Electroacoustics* **15** (Jun, 1967) 70–73, [doi:10.1109/TAU.1967.1161901](https://doi.org/10.1109/TAU.1967.1161901).
- [73] D. Allan, "Statistics of atomic frequency standards", *Proceedings of the IEEE* **54** (1966), no. 2, 221–230, [doi:10.1109/PROC.1966.4634](https://doi.org/10.1109/PROC.1966.4634).
- [74] N. El-Sheimy, H. Hou, and X. Niu, "Analysis and Modeling of Inertial Sensors Using Allan Variance", *IEEE Transactions on Instrumentation and Measurement* **57** (Jan, 2008) 140–149, [doi:10.1109/TIM.2007.908635](https://doi.org/10.1109/TIM.2007.908635).
- [75] G. Dick, "Local oscillator induced instabilities in trapped ion frequency standards",
- [76] P. Cheinet, B. Canuel, F. Pereira Dos Santos et al., "Measurement of the sensitivity function in a time-domain atomic interferometer", *IEEE Transactions*

- on Instrumentation and Measurement* **57** (Jun, 2008) 1141–1148,
[doi:10.1109/TIM.2007.915148](https://doi.org/10.1109/TIM.2007.915148), [arXiv:0510197](https://arxiv.org/abs/0510197).
- [77] B. Canuel, “Étude d’un gyromètre à atomes froids”. PhD thesis, Université Paris Sud - Paris XI, 2007. [doi:tel-00193288](https://doi.org/10.1109/TIM.2007.915148).
- [78] J. L. Gouët, T. Mehlstäubler, and J. Kim, “Limits to the sensitivity of a low noise compact atomic gravimeter”, *Applied Physics B* (2008) 1–30, [arXiv:arXiv:0801.1270v1](https://arxiv.org/abs/arXiv:0801.1270v1).
- [79] M. J. Vigué, A. Miffre, M. Büchner et al., “Phase noise due to vibrations in Mach-Zehnder atom interferometers”, *EPL (Europhysics Letters)* **75** (2006), no. 5, 688, [doi:10.1209/epl/i2006-10177-6](https://doi.org/10.1209/epl/i2006-10177-6), [arXiv:0604028](https://arxiv.org/abs/0604028).
- [80] M.-K. Zhou, Z.-K. Hu, X.-C. Duan et al., “Performance of a cold-atom gravimeter with an active vibration isolator”, *Physical Review A* **86** (Oct, 2012) 043630, [doi:10.1103/PhysRevA.86.043630](https://doi.org/10.1103/PhysRevA.86.043630).
- [81] K. Bongs, R. Launay, and M. Kasevich, “High-order inertial phase shifts for time-domain atom interferometers”, *Applied Physics B* **84** (Aug, 2006) 599–602, [doi:10.1007/s00340-006-2397-5](https://doi.org/10.1007/s00340-006-2397-5).
- [82] A. Peters, K. Y. Chung, and S. Chu, “High-precision gravity measurements using atom interferometry”, *Metrologia* **38** (Feb, 2001) 25–61, [doi:10.1088/0026-1394/38/1/4](https://doi.org/10.1088/0026-1394/38/1/4).
- [83] A. Sugarbaker and S. Dickerson, “Enhanced atom interferometer readout through the application of phase shear”, *Physical review ...* **94305** (2013) [arXiv:arXiv:1305.3298v1](https://arxiv.org/abs/arXiv:1305.3298v1).
- [84] J. R. Macdonald and W. J. Thompson, “Least-squares fitting when both variables contain errors: Pitfalls and possibilities”, *American Journal of Physics* **60** (Jan, 1992) 66–73, [doi:10.1119/1.17046](https://doi.org/10.1119/1.17046).
- [85] G. J. Dick, J. D. Prestage, C. A. Greenhall et al., “Local oscillator induced degradation of medium-term stability in passive atomic frequency standards”, in *The 22nd Annual Precise Time and Time Interval (PTTI) Applications and Planning Meeting*, pp. 487–508. 1990.
- [86] M. Meunier, I. Dutta, R. Geiger et al., “Stability enhancement by joint phase measurements in a single cold atomic fountain”,

- [doi:10.1103/PhysRevA.90.063633](https://doi.org/10.1103/PhysRevA.90.063633), [arXiv:1501.01943](https://arxiv.org/abs/1501.01943).
- [87] B. Fang, I. Dutta, P. Gillot et al., “Metrology with Atom Interferometry: Inertial Sensors from Laboratory to Field Applications”, *Journal of Physics: Conference Series* **723** (2016), no. 1, [doi:10.1088/1742-6596/723/1/012049](https://doi.org/10.1088/1742-6596/723/1/012049), [arXiv:1601.06082](https://arxiv.org/abs/1601.06082).
- [88] X. Cheng, “No Title”. PhD thesis, Imperial College London, 2018.
- [89] M. Schuler, “Die Störung von Pendel und Kreiselapparaten durch die Beschleunigung des Fahrzeuges”, *Physikalische Zeitschrift* **24** (1923), no. 16.
- [90] T. Farah, C. Guerlin, A. Landragin et al., “Underground operation at best sensitivity of the mobile LNE-SYRTE Cold Atom Gravimeter”, [doi:10.1134/S2075108714040051](https://doi.org/10.1134/S2075108714040051), [arXiv:1404.6722](https://arxiv.org/abs/1404.6722).
- [91] P. Gillot, O. Francis, A. Landragin et al., “Stability comparison of two absolute gravimeters: Optical versus atomic interferometers”, *Metrologia* **51** (2014), no. 5, L15–L17, [doi:10.1088/0026-1394/51/5/L15](https://doi.org/10.1088/0026-1394/51/5/L15), [arXiv:1406.5134](https://arxiv.org/abs/1406.5134).
- [92] P. Cheiney, L. Fouché, S. Templier et al., “Navigation-Compatible Hybrid Quantum Accelerometer Using a Kalman Filter”, *Physical Review Applied* **10** (Sep, 2018) 034030, [doi:10.1103/PhysRevApplied.10.034030](https://doi.org/10.1103/PhysRevApplied.10.034030).
- [93] U. Schunemann, H. Engler, R. Grimm et al., “Simple scheme for tunable frequency offset locking of two lasers”, *Review of Scientific Instruments* **70** (1999), no. 1, 242, [doi:10.1063/1.1149573](https://doi.org/10.1063/1.1149573).
- [94] S. Chu, L. Hollberg, J. Bjorkholm et al., “Three-Dimensional Viscous Confinement and Cooling of Atoms by Resonance Radiation Pressure”, *Physical Review Letters* **55** (1985), no. 1,.
- [95] A. Miffre, M. Jacquay, M. Büchner et al., “Atom interferometry”, [doi:10.1088/0031-8949/74/2/N01](https://doi.org/10.1088/0031-8949/74/2/N01), [arXiv:0605055](https://arxiv.org/abs/0605055).
- [96] M. Pappa, P. C. Condylis, G. O. Konstantinidis et al., “Ultra-sensitive atom imaging for matter-wave optics”, *New Journal of Physics* **13** (Nov, 2011) 115012, [doi:10.1088/1367-2630/13/11/115012](https://doi.org/10.1088/1367-2630/13/11/115012).
- [97] V. Schkolnik, B. Leykauf, M. Hauth et al., “The effect of wavefront aberrations in atom interferometry”, *Applied Physics B* **120** (Aug, 2015) 311–316, [doi:10.1007/s00340-015-6138-5](https://doi.org/10.1007/s00340-015-6138-5).

- [98] J. Hogan, "Towards precision tests of general relativity using an atom interferometer",.
- [99] M. Kasevich, "Atom Interferometry in an atomic fountain", 1992.
- [100] E. Masry, "Flicker noise and the estimation of the Allan variance", *IEEE Transactions on Information Theory* **37** (Jul, 1991) 1173–1177,
[doi:10.1109/18.86968](https://doi.org/10.1109/18.86968).
- [101] J. Schoser, A. Batär, R. Löw et al., "Intense source of cold Rb atoms from a pure two-dimensional magneto-optical trap", *Physical Review A* **66** (Aug, 2002) 023410, [doi:10.1103/PhysRevA.66.023410](https://doi.org/10.1103/PhysRevA.66.023410), [arXiv:0201034](https://arxiv.org/abs/0201034).
- [102] S. Y. Lan, P. C. Kuan, B. Estey et al., "Influence of the coriolis force in atom interferometry", *Physical Review Letters* **108** (2012), no. 9, 1–5,
[doi:10.1103/PhysRevLett.108.090402](https://doi.org/10.1103/PhysRevLett.108.090402), [arXiv:1110.6910](https://arxiv.org/abs/1110.6910).
- [103] G. Tackmann, P. Berg, C. Schubert et al., "Self-alignment of a compact large-area atomic Sagnac interferometer", *New Journal of Physics* **14** (Jan, 2012) 015002,
[doi:10.1088/1367-2630/14/1/015002](https://doi.org/10.1088/1367-2630/14/1/015002).
- [104] J. Hogan, D. Johnson, and M. Kasevich, "Light-pulse atom interferometry", *arXiv preprint arXiv:0806.3261* (2008) 1–38, [arXiv:arXiv:0806.3261v1](https://arxiv.org/abs/arXiv:0806.3261v1).

Acronyms

ADC Analogue-to-Digital Converter

AOM Acousto-optic Modulator

CCM Centre for Cold Matter

DAC Digital-to-Analogue Converter

DAQ Data Acquisition

DDS Direct Digital Synthesiser

ECDL External-Cavity Diode Laser

EDFA Erbium-Doped Fibre Amplifier

EOM Electro-optic Modulator

FPGA Field-Programmable Gate Array

GNSS Global Navigation Satellite System

HWP Half-wave Plate

MOT Magneto-optical Trap

NA Numerical Aperture

NEG Non-evaporative Getter

PBS Polarising beam-splitter

PLL Phase-Locked Loop

PM Polarisation-Maintaining

PPLN Periodically-Poled Lithium Niobate

QWP Quarter-wave Plate

SPI Serial Programming Interface

UHV Ultra-high Vacuum

VCA Voltage-Controlled Attenuator

VCO Voltage-Controlled Oscillator

⁸⁷Rb Rubidium-87

⁸⁵Rb Rubidium-85